Mechanisms and Machine Science 4

Liang Yan
I-Ming Chen
Chee Kian Lim
Guilin Yang
Kok-Meng Lee

Design, Modeling and Experiments of 3-DOF Electromagnetic Spherical Actuators

Springer

Design, Modeling and Experiments of 3-DOF Electromagnetic Spherical Actuators

MECHANISMS AND MACHINE SCIENCE

Volume 4

Series Editor

MARCO CECCARELLI

For other titles published in this series, go to
www.springer.com/series/8779

Liang Yan • I-Ming Chen • Chee Kian Lim •
Guilin Yang • Kok-Meng Lee

Design, Modeling and Experiments of 3-DOF Electromagnetic Spherical Actuators

Springer

Liang Yan
Beihang University
School of Automation Science
and Electrical Engineering
100191 Beijing
People's Republic of China
lyan1991@gmail.com

I-Ming Chen
Nanyang Technological University
School of Mechanical and Aerospace
Engineering
639798 Singapore
Singapore
michen@ntu.edu.sg

Chee Kian Lim
Singapore Polytechnic
School of Mechanical & Aeronautical
Engineering
500 Dover Road
139651 Singapore
Singapore
lim_chee_kian@sp.edu.sg

Guilin Yang
Singapore Institute
of Manufacturing Technology
Nanyang Drive 71
638075 Nanyang
Singapore
glyang@SIMTech.a-star.edu.sg

Kok-Meng Lee
Georgia Institute of Technology
30332-0405 Atlanta
USA
kokmeng.lee@me.gatech.edu

ISSN 2211-0984
ISBN 978-94-007-1645-2
DOI 10.1007/978-94-007-1646-9
Springer Dordrecht Heidelberg London New York

e-ISSN 2211-0992
e-ISBN 978-94-007-1646-9

Library of Congress Control Number: 2011930839

Cover design: VTeX UAB, Lithuania

Printed on acid-free paper

Springer is part of Springer Science+Business Media (www.springer.com)

The book is dedicated to authors' families.

Preface

学而不思则罔，思而不学则殆。
— 孔子（公元前551-479）

Learning without thought is labor lost; thought without learning is perilous.
– Confucius (551-479 BC)

Motors and actuators producing one degree-of-freedom (DOF) rotary or linear motion have been the main driving elements of modern machinery for a long time. With the advancement of technology, more and more new machines possessing complex structures and sophisticate motions to achieve tasks that have never been automated before have been developed, for example, humanoid robots, surgical robots, electric vehicles, just to name a few. In order to have a compact design of the machinery, actuators that can produce multiple degrees of freedom motion in one integrated package without the intermediate transmission mechanisms become crucial. However, there are quite a few technical challenges to realize a multiple DOF actuator at present. First, investigation of the actuating principle for multiple DOF motions with load bearing capability like or greater than the human is necessary. There are very few types of actuators that can achieve the load density comparable to that of the human. The design of the load bearing structure for multiple DOF motion is another important factor. One DOF rotary or linear motors can run smoothly and precisely with readily available precision rotary and linear bearings. It is not possible to find such component for multi-DOF actuators at present. If precise motion control is required for such multi-DOF actuators, sensors that can detect the multiple DOF rotor motion are necessity. Hence, multi-DOF sensing technology becomes part of the work for the realization of the actuator.

Spherical motion is a compact multi-DOF rigid body motion along a spherical surface with permanent center of rotation. By examining the machinery and systems surrounded us, spherical motion could possibly be the second most important motion type next to the compact rotary motion. Biological systems examples with spherical motions can be found in the eyeball movements, human wrist, shoulder,

and hip joint motions. Industrial examples can be found in the surveillance devices, automation tools, automobiles, and home appliances. Existing spherical motion generation devices are frequently designed by combining two to three rotary actuators with serially or parallel connected mechanisms. Such devices are inevitably bulky and difficult to be deployed as a critical component in complex machinery. Therefore, the need to develop a multiple DOF actuator capable of generating spherical motion arises.

The theme of this monograph is on the development of a compact electromagnetic spherical actuator that can produce two or three degrees of spherical motion. Through the study of this spherical actuator, the challenges of designing a multi-DOF actuator mentioned above are to be addressed. Spherical actuators based on a number of actuating principles such as electromagnetic force, piezoelectricity and mechanical means, have been explored by researchers. Electromagnetic actuation principle is chosen because of the load density, abundance of the material, and its compatibility with existing single DOF motors widely available at present. The underlying actuator design is a ball-joint structure with a rotor and a stator. The rotor is capable of moving in different orientations with finite angles or full 360 degrees about a fixed point within the actuator. It is our hope that the spherical actuator designed in this manner can be accepted and adopted by the industry based on its novelty as well as its compatibility and resemblance with existing motors in terms of the actuating principle and control.

This monograph presents a generic methodology on modeling, design and experimental investigation on 3-DOF permanent magnet (PM) spherical actuators. A parametric design approach is adopted from the coil and pole layout, spherical magnetic field strength to the motor torque-current function. This approach offers researchers and engineers to design the spherical actuator, such as the pole configurations and structure parameters, based on specific requirements from the applications. Furthermore, the actuator design can be fine-tuned and optimized, which is often required in complex system design. The topics in this book cover the introduction of different types of spherical actuators, formulation of three-dimensional (3D) spherical magnetic field, analytical motor torque modeling, prototype development, experimental investigation on magnetic field and motor torque, and 3D orientation sensing techniques.

While this book is primarily intended for researchers and developers working on spherical actuators, sensors and instruments, we also hope that it will interest researchers and students working in the area of electric machines since the methods proposed could also be useful for the understanding and analysis of others electromagnetic actuators; people in the area of magnetic field analysis since this book is also an illustrative example of the modeling and analysis of complex magnetic fields; people in the area of sensors since this book provides a solid starting point for the basic concept and working principle of various orientation measurement methods. It is also our hope that this book could provide a steppingstone for greater technology advancement in multi-DOF actuator design as future applications of these actuators are abundant.

This book is a complete exposition of the research work accomplished by the authors on the electromagnetic spherical actuators over the years through research collaboration among the Nanyang Technological University (Singapore), Singapore Institute of Manufacturing Technology, and Georgia Institute of Technology (USA). The authors sincerely appreciate the institutional support received from the three organizations. The major portions of the book were based on the PhD dissertations of two authors, Liang Yan and Chee Kian Lim while studying at Nanyang Technological University. Part of the work on orientation sensing for spherical actuators received graduate student manpower support from China Scholarship Council. This book would not have been possible without the help and the support from many people. In particular, we would like to thank Dr. Wei Lin for the financial support, Mr. Jialin Su for valuable technical comments, Prof. Weihai Chen, Prof. Yunhua Li, Dr. Zhongwei Guo and Dr. Yan Lang for the design and construction of the experimental apparatus and the actuator control system, and Thomas Moong for data collection, in carrying out the research project and subsequently completion of this book. Deep appreciations from the authors also go to several former members of the Robotics Research Center of Nanyang Technological University, especially Yan Jin and Xueyan Tang for a number of figures in this book. The authors are grateful to their families whose patience and comprehension have permitted them to spend time and effort on elaborating and completing this book. Finally, the authors would also like to acknowledge the support from the Agency for Science, Technology and Research (A*STAR) of Singapore, the National Nature Science Foundation of China, and the Fundamental Research Funds for the Central Universities, China.

December 2010 Singapore, Beijing, and Atlanta

Contents

List of Figures

List of Tables

Acronyms

1/2/3D	One/two/three-dimensional
AC	Alternating current
AWG	American wire gauge
BC	Boundary condition
CCD	Charge-coupled device
DAQ	Data acquisition
DC	Direct current
DOF	Degree-of-freedom
DLIM	Double-sided linear induction motor
FE	Finite element
FEA	Finite element analysis
SLIM	Single-sided linear induction motor
MST	Maxwell stress tensor
PC	Personal computer
PM	Permanent magnet
PZT	Piezoelectric
SPM	Spherical pointing motor
SWM	Spherical wheel motor
SRM	Switched reluctant motor
VRSM	Variable-reluctance spherical motor

Chapter 1
Introduction

Over the past decades, spherical actuator has been a more and more popular research topic worldwide. Due to its advantages of compact size, high motion precision, fast response, direct driven, non-singularity in workspace and high efficiency, it has wide potential applications in robotics, manufacturing, automobile, precision assembling and medical surgery. The fundamental concepts and working principles of various spherical actuators are presented in the monograph. Systematic study approaches on the modeling, design, experimental investigation and orientation sensing technologies of permanent magnet (PM) spherical actuators are the focus of this book. In this chapter, the background and motivation of the development of multi-degree-of-freedom (multi-DOF) spherical actuator is introduced. Following that, the state of the art of the studies on spherical actuators is reviewed. Subsequently, the research objective and scope of a 3-DOF PM spherical actuator are presented. Finally, the outline of the monograph is proposed.

1.1 Background and Motivation

An electric motor is a device that converts electricity into mechanical motions. Most electric motors work by electromagnetism, but motors based on other electromechanical phenomena, such as electrostatic forces and the piezoelectric effect, exist as well.

So far, motors with 1-DOF rotary or linear motion dominate the market. The rotary motor can be categorized as direct current (DC) motor and alternating current (AC) motor. As illustrated in Fig. 1.1(a), a classical DC motor has coils laying in the magnetic field of permanent magnets (PMs). A rotary switch called a commutator reverses the direction of the electric current flowing through the coils twice in every cycle so that a torque with constant direction can be generated between the coils and PMs resided on the fixture of the motor. The AC motor in Fig. 1.1(b) uses the phase differences between the three phases of the electrical current to create a rotating electromagnetic field in the motor. The rotor often consists of a number of copper

L. Yan et al., *Design, Modeling and Experiments of 3-DOF Electromagnetic Spherical Actuators*, Mechanisms and Machine Science 4,
DOI 10.1007/978-94-007-1646-9_1, © Springer Science+Business Media B.V. 2011

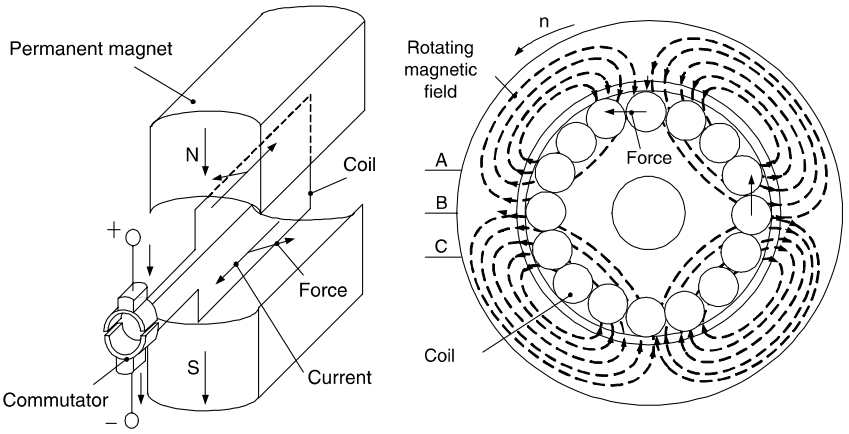

(a) DC motor (b) AC motor

Fig. 1.1: Conventional single-axis rotary motors

conductors embedded in the steel. Through electromagnetic induction, the rotating magnetic field induces current to flow in these conductors, which in turn generates a torque by interacting with the magnetic field and then move the rotor to turn in the direction that the field is rotating in. This type of motor is known as induction motor or asynchronous motor, as the rotor must always run slower than the frequency of the supplied power for operation. If the rotor coils are introduced with a separate current, one has a synchronous motor. The rotor will rotate in synchronism with the rotating magnetic field produced by the three-phase AC power.

Many industrial applications require multi-DOF rotational motions to achieve various targets. Since conventional motors can have only 1-DOF rotation, at least three motors connected in series or in parallel are needed to provide a multi-DOF spherical motion [1, 2, 3, 4, 5]. However, this type of combined multi-DOF actuator system has intrinsic disadvantages:

- the friction and backlash exist in motion transmission mechanism, which inevitably reduces the motion accuracy;
- large mass and inertia moment of the combined actuator introduce high energy consumption and low dynamic performance;
- kinematic singularities exist in the operation range of the actuator.

The desire to eliminate all these drawbacks motivated researchers to design a compact and high performance 3-DOF rotary actuator. One promising solution is the spherical actuator. The spherical actuator is a ball-joint-like device that is capable of performing 3-DOF rotational motion in a single joint. It has unique features and potential applications as follows.

(a) Laser alignment [6]

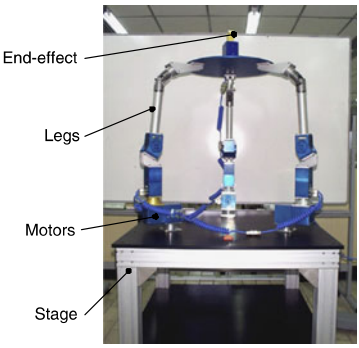

(b) Machining tool [7]

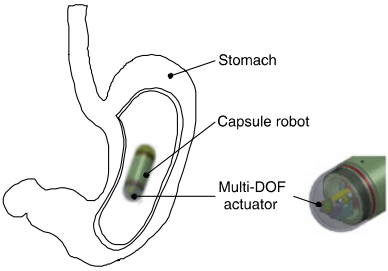

(c) Robot in stomach

(d) Micro robot [8, 9]

(e) Pick and place manipulator [10]

(f) Automobile wheel

Fig. 1.2: Potential applications of multi-DOF spherical actuators

- **High motion precision**

Conventional spherical motion mechanism consists of several single-axis motors and a large number of connecting mechanisms such as linkages, gears and worms that increase the system backlash more or less. As a result, the motion precision of the end-effector is reduced greatly. For spherical actuators, however, there is only one stator and one rotor, and no complex connecting parts. Therefore, its motion precision is much higher than that of conventional spherical motion mechanisms,

and could be used for high precision facilities like laser alignment equipment (Fig. 1.2(a)) and high precision machining tools (Fig. 1.2(b)).

- **Compact size**

The spherical actuator overcomes the disadvantage of bulky structure in conventional spherical motion mechanisms. It has compact size as well as high energy density. This feature helps designers to minimize the size of manipulators or robots, and thus to achieve dexterous motions in small workspace. Therefore, it could be utilized for the development of medical robots such as drug delivery robot and capsule endoscope that work in gastrointestinal tract to detect and treat the disease (Fig. 1.2(c)), and other micro-sized robots (Fig. 1.2(d)).

- **Low moment inertia and fast response**

In conventional spherical motion mechanisms, some connecting parts and single-axis motors are mounted on top of other motors. Thus, extra payload is added on the bottom joints/actuators, which increases the power consumption and decreases the system response speed and working efficiency significantly. Due to the compact structure of the spherical actuator, however, the inertia moment of the rotor is very low, and there is no additional inertia moment produced by other motors or linkages. Therefore, spherical actuator can achieve fast response and high working efficiency. It could be employed for mechatronic systems requiring high dynamic performance such as tracking radar and tank barbette.

- **Non-singularity in workspace**

It can be proved that there is no singularity points in the workspace of spherical actuators, i.e., for any rotor orientation in the workspace, we can always find at least one set of current inputs to move the rotor to neighborhood orientations. This feature maximizes the working range of manipulator (Fig. 1.2(e)), helps it to achieve smooth motion trajectory, and thus increases the system working efficiency.

- **Direct driven scheme**

It is worth pointing out that spherical actuators have very broad potential applications in automobile industry such as wheels (Fig. 1.2(f)). Nowadays, differential gear train is utilized in automobiles to transmit the engine's motion to the wheels. This makes the driving system very complex and large, and increases the energy loss during the transmission. The automobile wheels can generate multi-DOF rotational motions. The spinning motion drives the automobiles to move forward or backward, whereas the tilting motions steer the car's moving direction. Therefore, the wheel's motion is similar to that of spherical actuators. We may replace current automobile wheel and the differential gear train with spherical actuator in the new generation green cars. Apparently, it simplifies the driving system and increases the power efficiency. The spherical actuator works in the direct driven way, i.e., there is no intermediate motion transmission. This scheme can reduce the friction and vibration in the system, and thus increase the power efficiency.

In short, spherical actuator can be employed in a variety of industrial applications where orientation must be achieved rapidly, continuously and uniformly. It will greatly contribute to the development of robotics, manufacturing, automobile, precision assembling, medicine and especially, electrical vehicles.

1.2 The State of the Art

Currently, there are three different types of driving techniques proposed for the design of multi-DOF spherical actuators: the mechanical means, piezoelectricity and electromagnetic forces.

A spherical actuator driven by wires mechanically has been demonstrated by Nagasawa *et al* [11]. As illustrated in Fig. 1.3, the rotor (spherical cell) is put inside the concave shell and can move like a spherical sliding bearing. Four wires are connected between the rotor and four single-axis motors so that the orientation of the rotor can be moved to a desired position through tightening and/or loosening the wires. Essentially, this spherical actuator is similar to the conventional spherical

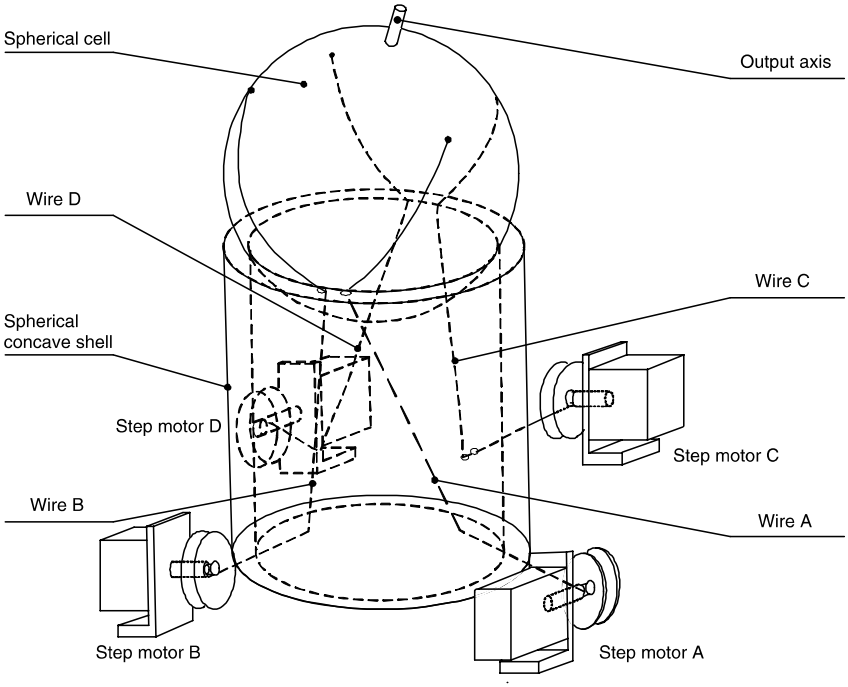

Fig. 1.3: A cable-driven spherical motor [11]

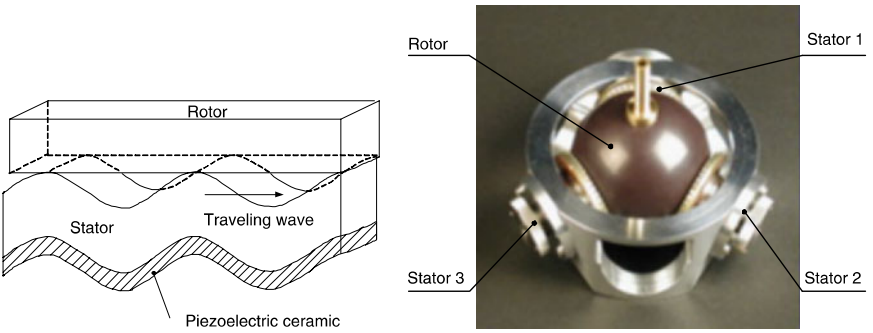

(a) Working principle [14] ©2001 IEEE (b) A prototype [15, 16] ©2003 IEEE

Fig. 1.4: Ultrasonic spherical motor with three stators

motion mechanism because four single-axis motors are utilized to drive the rotor in way of parallel mechanism.

Ultrasonic spherical actuators have been studies by several researchers. For instance, Amano *et al*. [12] have proposed a 3-DOF ultrasonic actuator design using bending and longitudinal vibrations of a single stator installed with three sets of piezoelectric (PZT) elements; Aoyagi *et al*. [13] have proposed a multi-DOF ultrasonic motor by using low-cost thick-film technology; Toyama *et al*. [14, 15, 17, 18, 19] have developed an ultrasonic motor as a fine-orienting stage. The working principle of ultrasonic motors is based on the reverse piezoelectric effect of ceramics, i.e. an applied electric voltage can cause a PZT material to change dimensions. A typical example [14] is illustrated in Fig. 1.4(a). A PZT element layer is bonded to the back of the stator. It can produce expansion or contraction

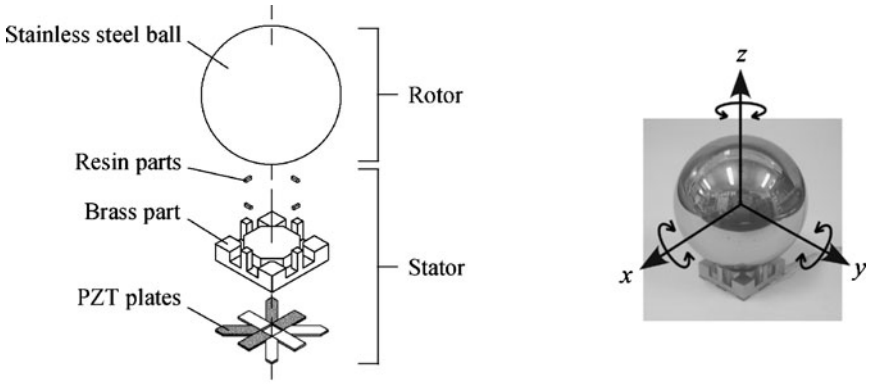

(a) Exploded view (b) A prototype

Fig. 1.5: Ultrasonic spherical motor with compact stator plate [20] ©2001 IEEE

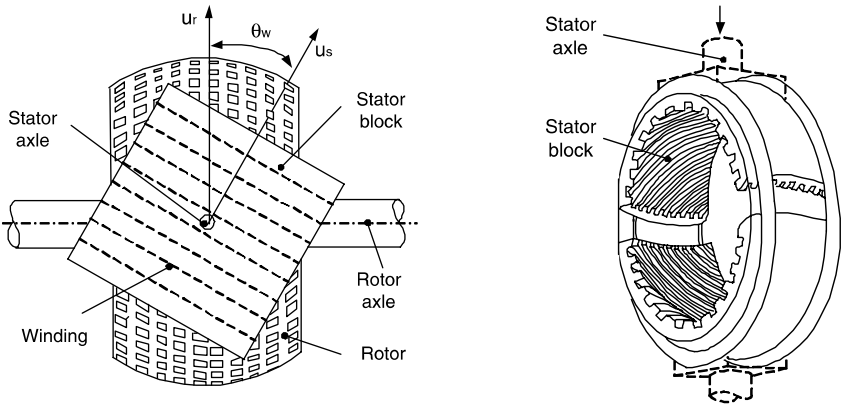

(a) Rotor and stator block (b) Structure of the stator

Fig. 1.6: A 2-DOF spherical induction motor by Williams *et al*. [22] ©1959 IEEE

motions after being energized positively or negatively. Thus, a traveling wave on the surface of the stator is generated. This traveling wave can drive the rotor on top of the stator. By using three stators of the same type, a 3-DOF spherical motion of the rotor can be achieved (Fig. 1.4(b)). To overcome the large volume of stator in previous ultrasonic spherical motors, Takemura *et al*. [20, 21] have developed a multi-DOF ultrasonic motor with a compact plate stator. As shown in Fig. 1.5, this multi-DOF ultrasonic motor consists of a spherical rotor made of stainless steel and a plate stator. The stator is composed of a brass part, resin parts, and PZT plates. The depressed sections in the brass part have functions to adjust natural frequencies and enlarge vibration amplitudes at contact points. The resin parts are located at the contact points with the rotor. This allows the contact points to have appropriate stiffness for friction to effectively drive the rotor. The ultrasonic actuator has the advantages of high motion resolution and low power consumption. However, it also possesses disadvantages such as low speed, complex fabrication and hysteresis. Furthermore, wear of frictional material for long term operation may cause instability of the spherical motion.

Most spherical actuators are based on the principle of electromagnetism. Williams and Laithwaite *et al*. [22] have designed the first spherical induction motor. As shown in Fig. 1.6(a), the rotor is made of ferromagnetic material with a spherical barrel shaped surface. A copper mesh is inlaid on the rotor surface to allow induction current to travel in longitudinal and latitudinal directions. The stator consists of two multiphase winding blocks (Fig. 1.6(b)) that can be twisted with an angle θ_w about an axis perpendicular to the rotor's axle, generating a rotational magnetic field at velocity u_s which induces the current on the surface of the rotor. The rotor approaches the synchronous speed $u_r = u_s/\cos\theta_w$, which can be changed by varying θ_w. Including the rotation of the rotor and the twist of the stator blocks, this motor has two DOFs, despite the fact that the twist of the stator blocks is not ac-

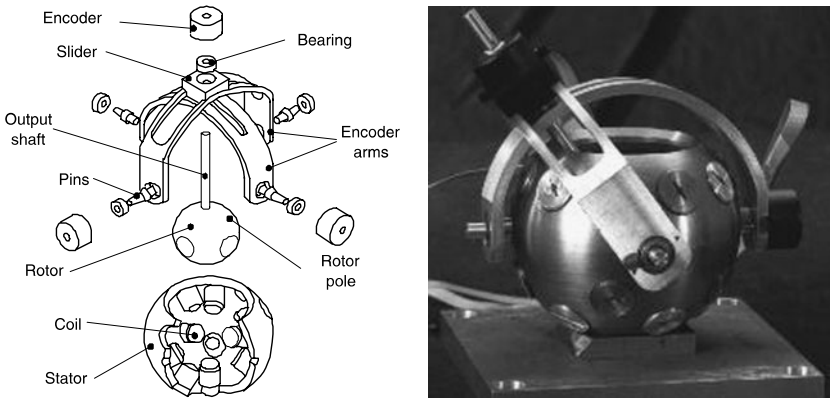

(a) Exploded view [34] (b) Prototype [33]

Fig. 1.7: Variable reluctance spherical motor by Lee *et al*.

complished by the winding currents. Davey *et al*. [23] have analyzed the magnetic field and torque of this type of spherical induction motor. A true 3-DOF spherical motor could not be developed by simple modification of this motor.

Vachtsevanos and Lee *et al*. [24, 25, 26, 27, 28, 29] have proposed two types of 3-DOF spherical motors for robotic applications. One of them is spherical induction motor. The rotor is a ball filled with infinite permeability material and encapsulated with conducting shell. Three sets of windings are mounted on the stator and excited to generate induced current on the rotor surface, and thus to drive the rotor to achieve 3-DOF rotations. However, no prototype has been constructed for this conceptualized spherical motor, because of the complexity in mechanical design, especially inlaying three transversal windings on the inner spherical surface is practically difficult. A second realization of the spherical motor is based upon the step motor principle. The hemispheric stator structure is designed to support coils, iron trimmings, bearings and the position measurement devices. A pair of PM poles are mounted on the rotor. The rotor is supported by six bearings on the stator. Energizing the stator coils sequentially, the rotor can be pulled to any desired orientation.

The variable reluctance spherical motor (VRSM) has been developed by Lee *et al* [30, 31, 32, 33, 35, 36, 37, 38, 39, 40, 41, 42] (Fig. 1.7). The stator is constructed of iron, which provides a magnetic flux path for linking stator poles. The stator poles consist of evenly spaced coils wound on ferromagnetic cores. These poles are arranged on the inside of the stator surface and at the vertices of a dodecahedron. The rotor consists of iron poles embedded in a round, smooth sphere following the pattern of octahedron. The torque of VRSM depends on the current inputs as well as the magnetic reluctance of the airgaps between the rotor and the stator poles. The reluctance of the airgap is a function of the relative position between the rotor and stator, and varies as the rotor moves, hence the name of VRSM. About two-thirds of the inertia moment of the entire system is contributed by the orientation mea-

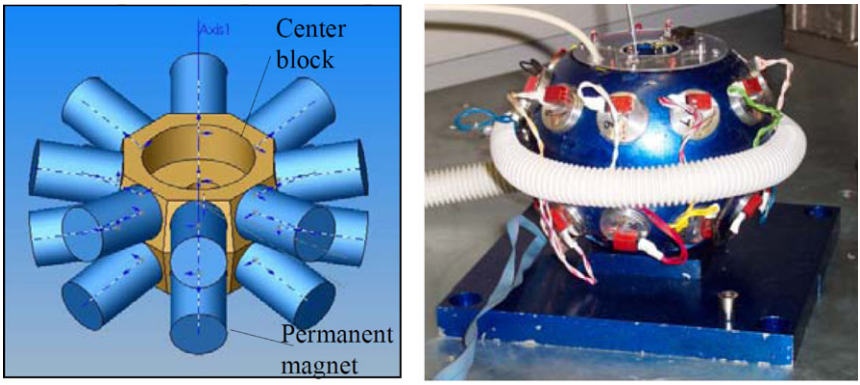

(a) Rotor assembly (b) Prototype

Fig. 1.8: 3-DOF spherical wheel motor by Lee *et al*. [43]

surement system consisting of three encoders, which cannot be ignored for system control [34].

Lee *et al*. [43, 44, 45] have also proposed the concept of spherical wheel motor (SWM). Unlike existing VRSM motors where design focuses have been on controlling 3-DOF angular displacements, the SWM offers a means to control the orientation of a continuously rotating shaft in an open-loop (OL) fashion. They provide a formula for deriving different switching sequences (full step and fractional step) for a specified current magnitude and pole configurations. The concept feasibility of an OL controlled SWM has been experimentally demonstrated on a prototype that has 8 rotor PM pole-pairs (two layers) and 10 stator electromagnet pole-pairs (two layers) as illustrated in Fig. 1.8.

Following the same concept of SWM, Cho *et al*. [46, 47] have developed a 3-DOF motor. As shown in Fig. 1.9, 4 PM poles are mounted on the rotor and 12 coils are mounted on the stator. The rotor is connected guide frame to bind on 3D as controlled by 12 channels of current source mounted inside of the stator. A current compensation function is proposed to increase stable operating range. The compensation function was estimated by using torque ripple computed from torque simulation.

Motivated by the inadequacy of industrial rotor manipulators and a proposed coarse-fine-manipulation solution, Hollis *et al.* [48, 49, 50, 51, 52, 53, 54] have developed a multi-DOF magnetically levitated fine-motion wrist. As shown in Fig. 1.10(a), every pole of this wrist consists of two U-shaped PMs and a flat-wound rectangular coil. The two U-shaped magnets are placed in opposite to form a loop with the small airgap. Between the two U-shaped magnets is the flat-wound rectangular coil. When the coil is excited with currents, it can move in the gap under the effect of magnets. Six flat-wound coils are attached on the six surfaces of a hexagonal cylinder in an interlaced longitudinal and latitudinal pattern (Fig. 1.10(b)). Six pairs of PMs are placed on both sides of coils so that the longitudinal position coil could

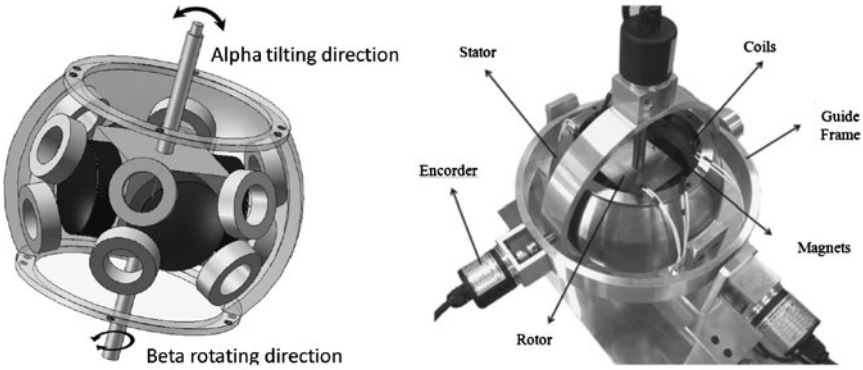

(a) Operating mode (b) Prototype

Fig. 1.9: 3-DOF spherical wheel motor by Cho *et al*. [46] ©2008 IEEE

move in latitudinal direction and the latitudinal position coil could move in longitudinal direction. Therefore, with respect to the magnets, the cylinder has 6-DOF motion. This wrist has relatively small workspace, allowing maximum translations and rotations of approximately $\pm$5mm and $\pm 4^{\circ}$.

Foggia *et al*. [55] have designed an electromagnetic actuator rotating around three independent axes. As illustrated in Fig. 1.11, the actuator consists of a moving armature and three fixed inductors. The moving armature is composed of a hollow sphere made of solid steel and can move around its center point. The outer surface of the armature may be used to attach additional components like antennas, cameras and light beam supports, etc. depending upon the application the user is looking after. On the inner surface of the sphere, there is a thin deposit of copper obtained

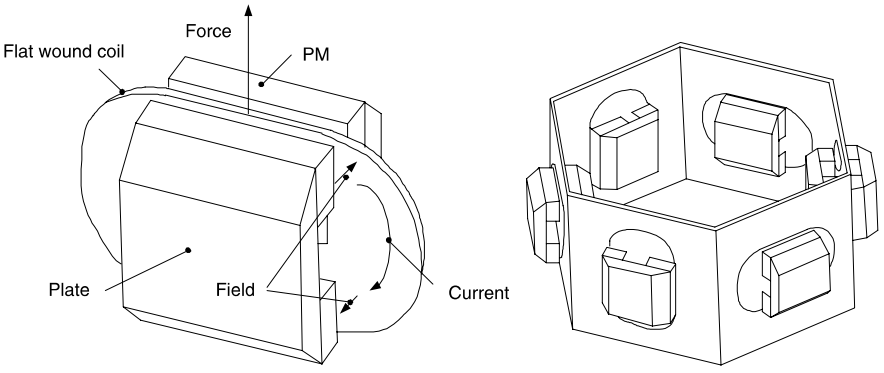

(a) Single pole (b) Actuator with six poles

Fig. 1.10: Multi-DOF motion wrist by Hollis *et al.* [51] ©1991 IEEE

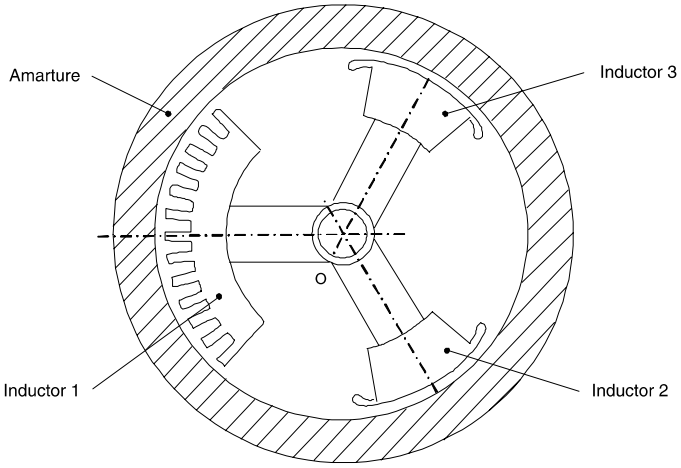

Fig. 1.11: 3-DOF induction motor by Foggia *et al*. [55] ©1989 IEEE

through electrolytic processing. When the three inductors are adequately supplied, a moving magnetic field can be created. This magnetic field can induce current on the thin copper deposit, which in turn generates torques on the armature by interacting with the magnetic field. This electromagnetic actuator can achieve a maximum deviation of $\pm 30^\circ$. Experimental results showed that the motor prototype exhibited significant noise and had a rather long response time of 5 seconds.

Kaneko *et al*. [56] have developed a spherical DC servo motor with 3-DOF motions. The motor is constructed of a rotor, a spherical stator and a pivot bearing. As shown in Fig. 1.12(a), the rotor is a disk comprised of a yoke with four PMs attached to its periphery. The stator has three spherical windings with electric currents I_x, I_y and I_z (Fig. 1.12(b)). Three encoders are used to measure the rotor orientation. This motor can achieve a maximum spinning torque 0.30Nm and $\pm 15^\circ$ tilting motion.

The spherical pointing motor (SPM) (Fig. 1.13) designed by Bederson *et al*. [57, 58, 59, 60, 61] is a 2-DOF computer-controlled device which incorporates both pan and tilt motions. This actuator consists of three orthogonal windings in a PM field. The coils can be either assembled inside of the actuator, free to rotate on a gimbal in a fixed magnetic field, or mounted outside whereas the magnets are attached to the gimbal inside the coils. A charge-coupled device (CCD) camera can be mounted on the rotor. The operating principle of the SPM comes from the fact that there is always a force on a current-carrying wire loop in a PM field in such a direction that the loop will move to make the normal to the plane of the loop align with the magnetic field. As designed for applications in active vision, this pan-tilt mechanism should be fast, small, inexpensive and have low power requirement. It is an absolute positioning device and runs in open-loop. The accuracy of the actuator is dependant on the friction of the bearings as well as rotor orientations. According to the literature [58], this actuator is capable of panning and tilting with a load of

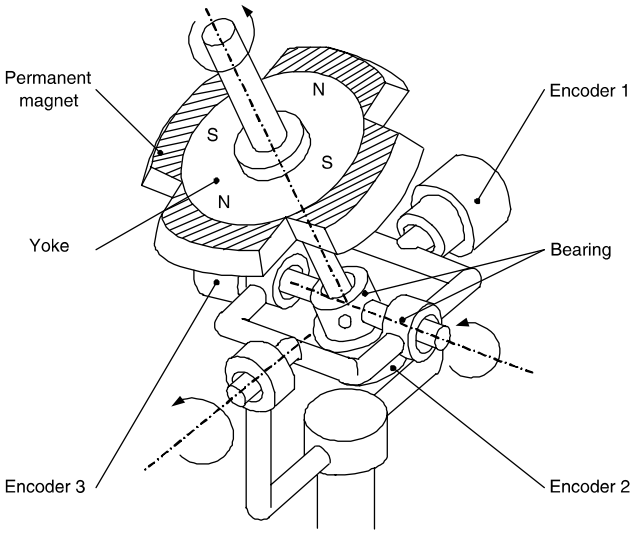

(a) Rotor

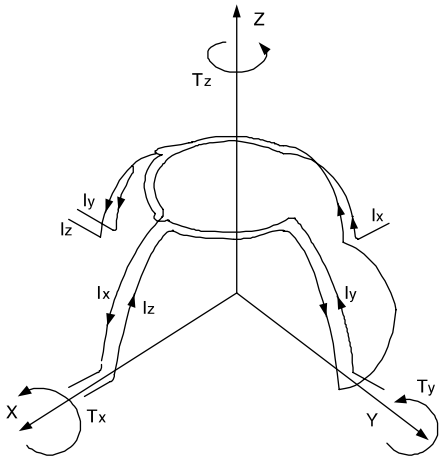

(b) Stator windings

Fig. 1.12: Spherical DC servo motor by Kaneko *et al*. [56]

15 grams at rotational velocity of several degrees per second with a repeatability of 0.15° at a fixed orientation.

Spherical actuators which can achieve either 2-DOF or 3-DOF motions have been developed by Wang *et al* [62, 63, 64, 65, 66, 67, 68, 69, 70, 71]. The spherical rotor is entirely made of magnetized rare-earth materials. It is housed within the spherical

Fig. 1.13: Miniature pan-tilt actuator by Bederson *et al*. [58] ©1994 IEEE

hollow stator on a low friction surface coating. Accommodated on the stator are several windings. On the application of current to the stator windings, the resulting torque can orientate the rotor to minimize the system potential energy. Thus, control of the rotor orientation can be achieved by varying the winding currents in the stator.

Oner *et al*. [72] have designed a spherical motor with similar structure. It consists of five parts: stator, rotor, bearings, coils and stator cover. The rotor is completely constitutive of four sector PM poles. Magnetization vector of PM poles is in the radius direction. The stator consists of eight independent coils. The coil is in the form of conical shape to occupy the space around the rotor as much as possible. The exterior shell of the motor is made of soft iron to reduce the magnetic energy loss. The coils are mounted on the stator around the rotor in the spherical motor. The 3D magnetic field has been simulated with FEM.

Weck *et al*. [73] have proposed a 3-DOF spherical motor with rotor diameter of 275mm. Coils are evenly mounted on the inner surface of the hemispherical stator and NdFeB magnets are plated on the entire rotor surface. The guiding of the rotor is realized by a hydrostatic bearing to achieve high stiffness and low friction. The oil can also reduce the temperature of the coils. The torque of this spherical motor has been calculated numerically.

Chirikjian *et al*. [74, 75, 76, 77] had designed a 3-DOF spherical step motor as shown in Fig. 1.14(c). Eighty cylindrical rare-earth PMs were placed along the inside surface of a hollow plastic sphere with a 12-inch diameter (Fig. 1.14(b)). Sixteen coils with iron cores are placed on the surface of a spherical cap and polarized to form the electromagnetic field within the stator (Fig. 1.14(a)). An adjustable magnet saddle holds the stator magnets so that the stator magnets can be repositioned and reoriented. Because the symmetry of the rotor-pole arrangement is different

(a) Stator [76, 78] ©1999 IEEE

(b) Rotor [76, 78] ©1999 IEEE

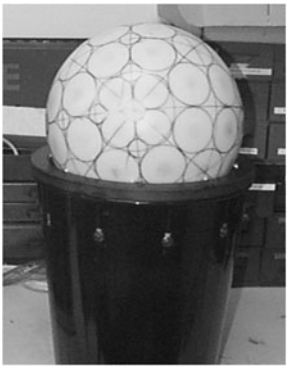

(c) Assembly [76, 78] ©1999 IEEE

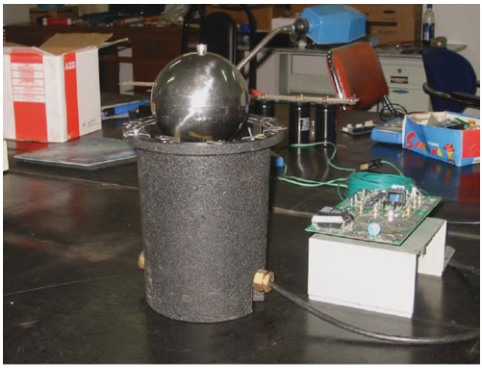

(d) Prototype by Li [79] ©2009 IEEE

Fig. 1.14: Spherical step motor by Chirikjian *et al*. and Li

from that of the stator poles, the magnetic field created by energizing two or more stator coils generates a torque that can change the rotor orientation. Li [79] (Fig. 1.14(d)) developed a spherical step motor with similar structure, and proposed a robust control based on neural networks to overcome uncertainties and disturbances such as environmental magnetic field, external load and friction that may generate speed ripple and decrease the system dynamic performance.

A similar electromagnetic spherical actuator has also been proposed by Ebihara *et al* [80]. Fig. 1.15 shows its basic structure. This actuator is based on same principle of PM type linear step motor. The spherical motor consists of the stator, the mover, and the mover supporting mechanism (bearing). The mover is composed of round-shaped PMs. The magnetic poles of the stator are round-shaped coils and distributed in triangular lattice. This design enables the spherical rotor to be driven by this magnetic poles distribution. To produce motions only in the 2D plane, the lattice distribution in which magnetic poles are distributed in parallel with x-axis

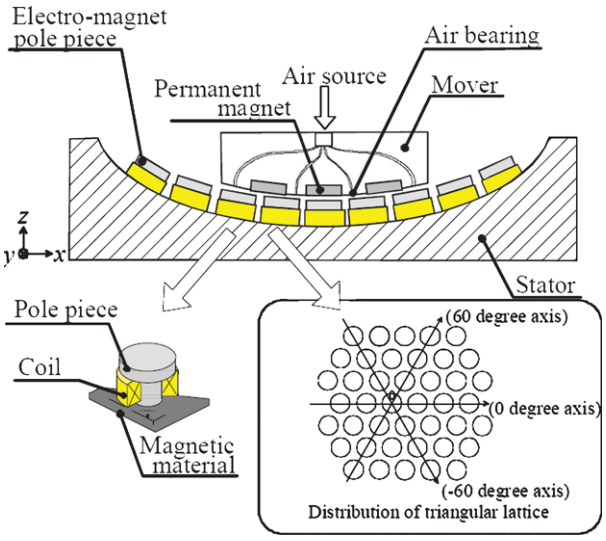

Fig. 1.15: Electromagnetic spherical motor by Ebihara *et al*. [80] ©2001 IEEE

and y-axis is sufficient. However, to produce motions in a spherical plane, the magnetic poles cannot distribute in this way. In the triangular lattice distribution that distributes the magnetic poles in the position used as a triangular vertex, if a surface of a sphere considers extension of polygon, this arrangement can uniformly distribute the magnet poles to a surface of a sphere. The mover has three basic axes of 0, $+60$, and -60 degree of angle as shown illustrated in Fig. 1.15.

Another spherical step motor with similar structure has been proposed by Ikeshita *et al* [81]. As illustrated in Fig. 1.16, the spherical motor is composed of a spherical

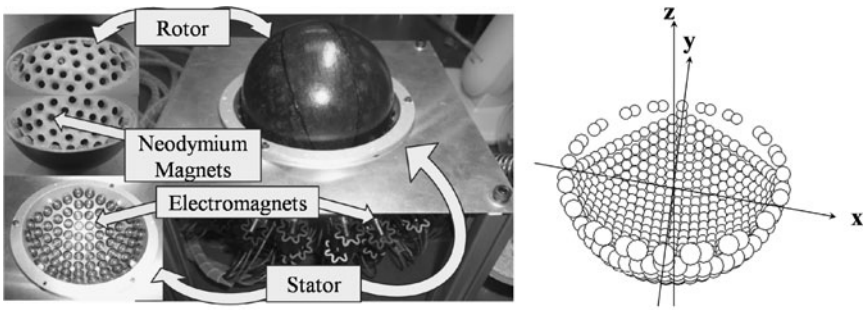

Fig. 1.16: 3-DOF spherical step motor by Ikeshita *et al*. [81]

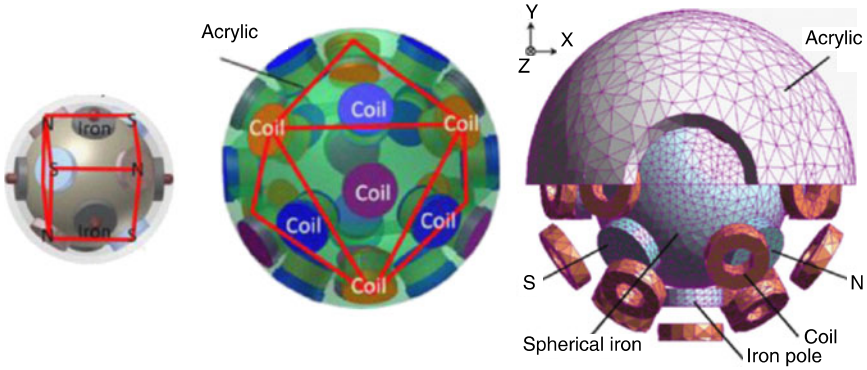

(a) Rotor (b) Stator (c) Meshed model

Fig. 1.17: Spherical step motor by Um *et al*. [82] ©2009 IEEE

rotor, a semi-spherical stator, a control PC, a control circuit, and a DC power supply. The rotor has 92 neodymium magnets, whereas 84 electromagnets are arranged on the stator. Each electromagnet can be excited to north or south magnetic pole to pull the rotor to change the orientation. The control PC calculates the posture of the rotor after a time interval and generates the pattern of excitation of electromagnets in order to move the rotor to the desired posture. The results of the performance of the developed spherical motor show that the maximum torque is 0.24 Nm, the maximum rotation speed is 2.5 rad/s, and the average error of rotation angle is up to several degrees that could be reduced by adding more magnets on the rotor.

Um *et al*. [82] have developed a spherical step motor based on a pair of a regular hexahedron and regular octahedron. The structure of the manufactured spherical step motor is illustrated in Fig. 1.17. Two type of poles are attached on the spherical surface of the rotor that is made of iron with 52mm of the inner diameter and 5mm of teeth. One type of poles is PM (NdFeB) with a pair of 4, and positioned on the imaginary fixed point of a regular hexahedron which is inscribed in the iron sphere. Another 6 iron-made poles are positioned on the each center surface of a regular hexahedron. In the stator, coils of three classes are inserted in the sphere of acrylic. First class (6 coils) is mounted on the imaginary fixed point of a regular octahedron that is inscribed in the acrylic sphere. Second class (16 coils) and third class (7 coils) are mounted on the imaginary edge and the imaginary center surface of a regular octahedron, respectively. This poles arrangement offers the advantage of high torque. Because the relationship between the PM poles on the rotor and the field winding on the stator is the same as the planer step motor of three phase circuit and bipolar, it is possible to use the control equipment of the planer step motor.

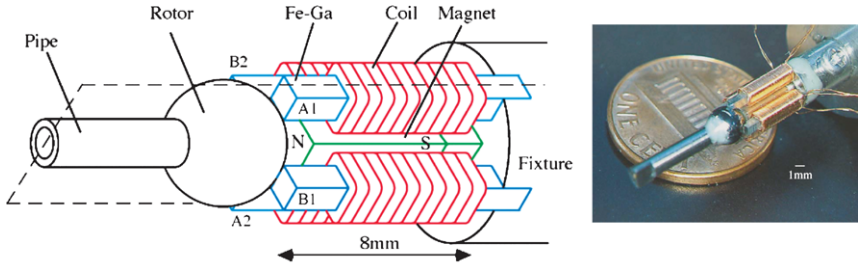

(a) Motor structure (b) Prototype

Fig. 1.18: Miniature spherical motor using iron gallium alloy by Ueno *et al*. [85]

Xia *et al*. [83, 84] have conceptualized a spherical actuator with Halbach array recently. In order to improve the torque output of spherical actuators, a layer of Halbach array PMs is arranged along the rotor equator, and multi-layers of air-core coils are mounted on the stator. The Halbach array magnetic structures have inherently sinusoidal air gap magnetic field distribution, high air gap flux density, and self-shielding effect. As a result, the torque value can be increased and the torque ripple can be suppressed effectively to achieve stable output performance.

A miniature spherical motor using iron gallium alloy (Galfenol) has been developed by Ueno *et al*. [85]. This motor consists of four rods of Galfenol with square cross-section, a wound coil, a PM, an iron yoke and a spherical rotor placed on the edge of the rods. The magnetomotive force of the magnet provides bias magnetostriction for the rods and an attractive force that maintains the rotor on the rods. When currents of 180° phase difference flow in pairs of opposing coils, a torque is exerted on the rotor by pushing (expansion) and pulling (contraction) of the rods. Rotation about a single axis is realized by a sawtooth current, such that the rotor rotates with slow expansion and slips at the rapid contraction. The motor can be fabricated at small sizes and driven with a low voltage, suitable for application as a micro actuator for rotating the camera and mirror in endoscopes.

1.3 Objective and Scope of the Study

As introduced, multi-DOF spherical actuators based on various operating principles have been developed by researchers. These actuators have particular features and advantages. However, so far there is no detailed report on systematic design methodologies on electromagnetic spherical actuators. The structures of previous spherical actuators are fixed uniquely, and it is not convenient to describe and analyze the relationship between actuator structure and torque output for design improvement generally. Therefore, the objective of this research is to investigate generic methodologies for modeling, design and experimental study of multi-DOF PM spherical

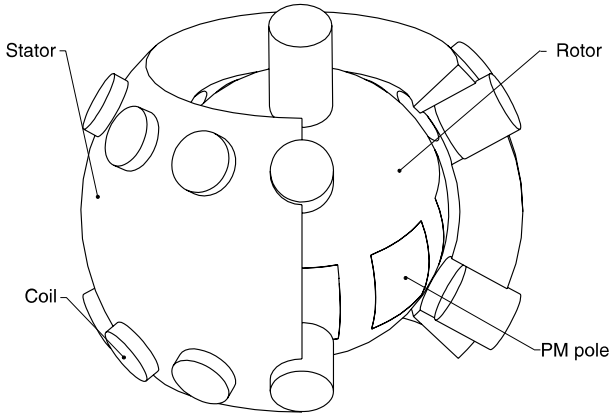

Fig. 1.19: Schematic drawing of PM spherical actuator

actuators for future commercial applications. Unlike previous spherical actuators, the structure of this proposed spherical actuator is more flexible, i.e. the structure of two major force/torque generating elements, PM and coil poles, are parameterized, which is useful for observing the relationship between structure parameters and magnetic field or torque output. This provides a way to increase the actuator torque output by selecting appropriate structure dimensions. Furthermore, in this spherical actuator, more PM and coil poles could be incorporated to increase the working range as well as the motion resolution of the actuator.

The proposed spherical actuator is driven by electromagnetic forces as electromagnetic actuators have advantages such as fast response, high torque and moderate voltage operation, etc. As an optional force/torque generating element of electromagnetic actuators, permanent magnet has a few virtues as follows [86].

- No electrical energy is absorbed by the field excitation system. Thus there are no excitation losses. This indicates that the efficiency of the PM actuator can be higher compared to actuators using only electromagnetic excitation.
- High torque or output power per volume can be achieved.
- Better dynamic performance can be achieved by using PM poles.
- The cost of rare-earth PMs has dropped significantly in recent years for wide adoption.

For these reasons, a 3-DOF electromagnetic spherical actuator with PM rotor poles is developed in this work. As illustrated in Fig. 1.19, this spherical actuator has two major parts: a ball-shaped rotor with a full circle of PM poles along the equator, and a spherical shell stator with multiple layers of circumferential air-core coils. The PMs made of rare-earth materials can produce high flux density. The use of air-core coils may simplify the control of the actuator based on linear torque model.

The basic working principle of the spherical actuator is illustrated in Fig. 1.20. By activating pairs of coils in two longitudinal directions, the rotor can tilt in two orthogonal directions as shown in Fig. 1.20(a) and (b). Energizing all rest coils, the

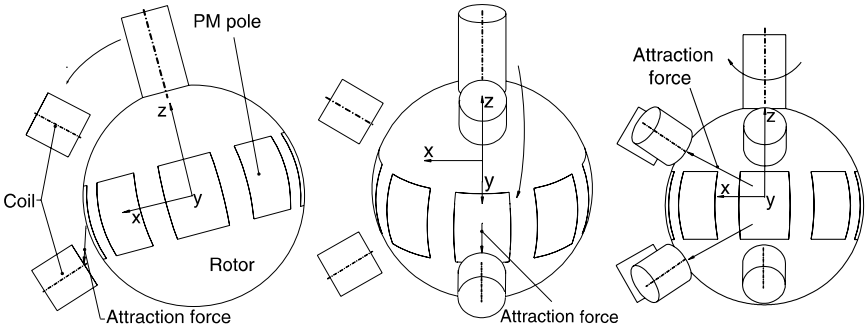

(a) First tilting motion (b) Second tilting motion (c) Spinning motion

Fig. 1.20: 3-DOF motion of spherical actuator

rotor shaft can spin about its own axis (Fig. 1.20(c)). Therefore, through varying the current inputs of the coils, any desirable 3-DOF spherical motion within the workspace can be achieved.

Figure 1.21 illustrates the major tasks that have been done in this study. Most tasks indicated in the figure are extended from torque modeling which is extremely important for motion control of the spherical actuator. Specifically, the magnetic field modeling is the prerequisite of the torque modeling; based on the torque model, design and development of a research prototype of the spherical actuator can be carried out; experimental investigation can be conducted on the magnetic field distribution and torque variation of this research prototype to verify the theoretical models; the orientation sensing technologies are discussed in this book too for future control implementation.

• **Magnetic field expression:** The purpose of magnetic field expression is to formulate the magnetic field of the PM-pole rotor analytically so that the torque modeling can be carried out. The PM rotor pole is defined based on several generic geometric parameters. The space of the rotor under study is divided into three regions according to their magnetic characteristics. Laplace's equation can be obtained for each of these three regions respectively, and thus the general solution of the magnetic scalar potential for each region can be obtained. By taking advantage of boundary conditions in between these regions, the unknowns in the general solution of magnetic scalar potential can be determined. Because the magnetic intensity is equal to the gradient of the magnetic scalar potential, the magnetic flux density of the PM-pole rotor can be obtained subsequently.

• **Torque modeling:** Following the magnetic field modeling, torque modeling of the PM spherical actuator is worked out. According to Lorentz force law, the force

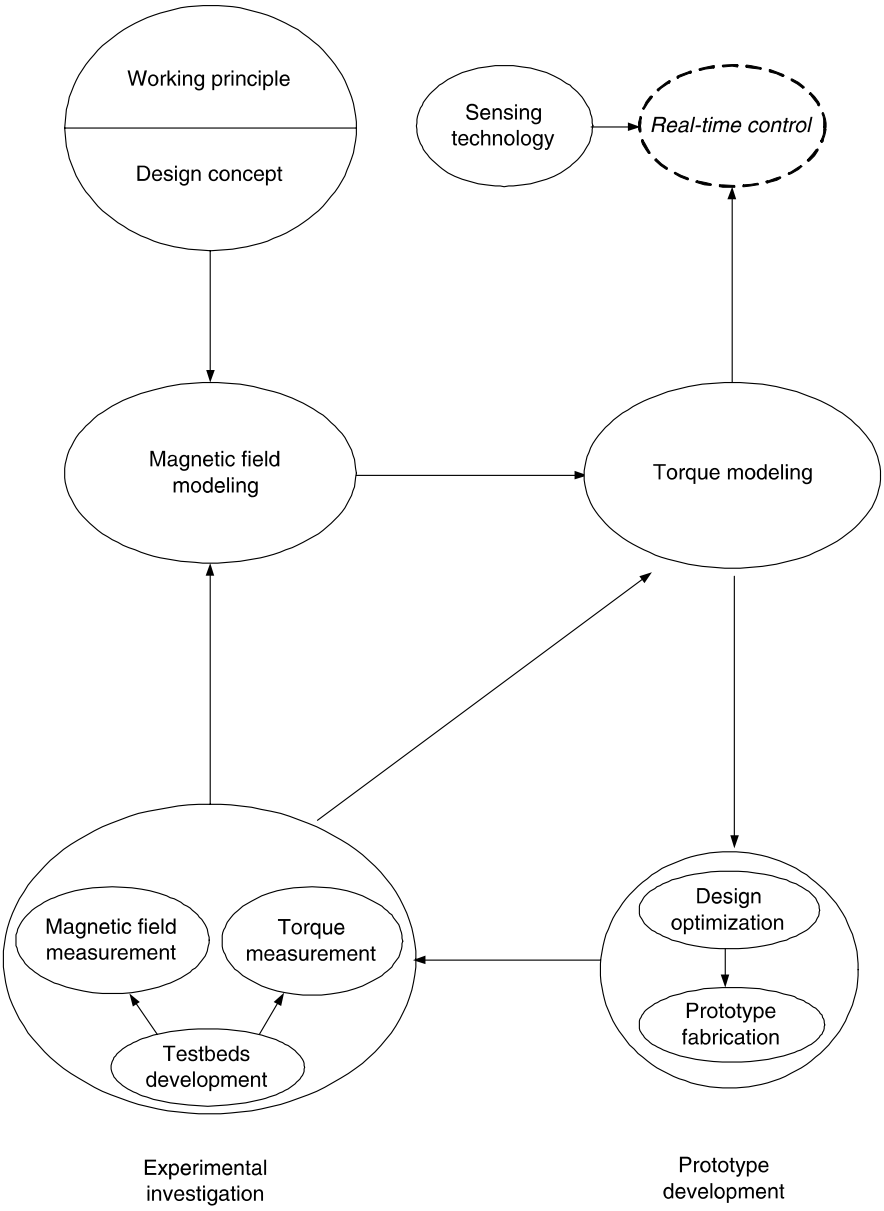

Fig. 1.21: Scope of the book

acted on a current-carrying conductor is equal to the multiplication of the current and the cross product of length segment vector and magnetic flux density. Therefore, the differential torque acted on a differential length segment of the winding with respect to the rotor center can be calculated by multiplying the moment arm with the differential force. Subsequently, integrating the differential torque within the entire volume of a single-coil results in the torque formula for a single coil. For each individual coil, similar formula can be obtained. Concatenating these formulas in a matrix form produces the torque model of the PM spherical actuator with full set of coils that relates current inputs and rotor orientation to the torque output.

• **Prototype development:** The parameters of PM and coil poles provide an effective way for actuator design. The design objective of the actuator is to achieve high torque output of the spherical actuator. According to the derived torque model, effects of poles parameters on the torque output can be described so that appropriate values of parameters can be chosen. Additionally, in order to increase the number of winding turns, several factors such as stacking patterns of windings, wire diameters, optional coil frames are discussed. Based on theoretical analysis, dimensions of PM pole and coil are determined, and thus a research prototype of the spherical actuator has been manufactured.

• **Experimental investigation:** The developed research prototype can be used for the experimental investigation on magnetic field and torque variation of the spherical actuator. The experimental results can be utilized to verify theoretical models. In order to measure the magnetic flux distribution of PM-pole rotor, an automated apparatus that is capable of locating any point surrounding the rotor needs to be developed. Through a three-axis hall probe, the three components of the flux density at particular points can be measured. Nondimensionalization and normalization of the acquired data for bench marking are carried out so that the experimental data can be referred by other similar designs without mentioning specific rotor dimensions. Furthermore, the measured data of the magnetic field can be visualized and compared with result from the theoretical model. In order to measure torque generated by stator coils, a force/torque measurement apparatus has been developed. This apparatus can obtain the 6D force/torque data for any rotor orientation within the workspace. The measured torque data is then compared with and to validate the theoretical torque model.

• **Orientation sensing technology:** To achieve high-precision motion control, orientation sensing is indispensable. There are various orientation sensing technologies proposed by researchers. Non-contact type sensing method is preferred as it does not bring additional inertia moment and friction on the rotor. Typical non-contact sensors are visual sensor based on barcode gridding pattern, optical sensor and Hall effect sensor. These measurement methods have their own features and advantages. However, generally, the measurement precision of these sensors is low, and is very sensitive to the environment. Therefore, an orientation measurement method based on laser detection is proposed in this study to achieve high precision and stable

measurement result. Several experimental apparatus are constructed to validate the concept of this orientation sensing method. In the future, we will implement this method into our spherical actuator by using simple laser diode in compact package for control purpose.

1.4 Book Organization

The remaining chapters of the monograph are arranged as follows. Chapter 2 introduces the working principle of the PM spherical actuator. According to the PM-pole arrangement, the magnetic field of the PM-pole rotor is formulated. Chapter 3 presents the torque modeling of the spherical actuator based on the magnetic field expression. By taking advantage of the magnetic field model and torque model, Chapter 4 describes the design of the spherical actuator and presents a research prototype. In Chapter 5, experimental apparatuses are developed to measure the flux density distribution of the PM-pole rotor and the torque variation of the spherical actuator. The data processing and presentation are discussed and the results are compared with theoretical models. Chapter 6 presents an orientation sensing technology based on laser detection. Finally, Chapter 7 summarizes this research work and makes recommendations for future research on the PM spherical actuator.

References

1. Kurtz R, Hayward V et al (1992) Multiple-Goal Kinematic Optimization of a Parallel Spherical Mechanism with Actuator Redundancy. IEEE Transactions on Robotics and Automation, vol. 8, no. 5:644–651, October 1992.
2. Gosselin C M, Perreault L, Vaillancourt C et al (1993) Simulation and Computer-Aided Design of Spherical Parallel Manipulators. Proceedings of Engineering in Harmony with Ocean, vol. 2:II301–II306, Victoria, BC, October 1993.
3. Wu T L, Chen J H, Chang S H et al (2008) A Six-DOF Prismatic-Spherical-Spherical Parallel Compliant Nanopositioner. IEEE Transactions on Ultrasonics, Ferroelectrics, and Frequency Control, vol. 55, no. 12:2544–2551, December 2008.
4. Paganelli D (2007) Avoiding Parallel Singularities of 3UPS and 3UPU Spherical Wrists. Proceedings of 2007 IEEE International Conference on Robotics and Automation, 1201–1206, Rome, Italy, 10–14 April 2007.
5. Chung B G, Yi B J, Suh I H, Kim W K, Chung W K et al (2001) Design and Analysis of a Spatial 3-DOF Micromanipulator for Tele-operation. Proceedings of 2001 IEEE/RSJ International Conference on Intelligent Robots and Systems, 1201–1206, Mani, Hawaii, USA, 29 October–03 November 2001.
6. RollCheck Green (2010) Picture of laser alignment. In: The website of Seiffert Industrial, Inc. Available online: http://www.seiffertindustrial.com/products/parallel-roll-alignment/rollcheck. Cited October 2010
7. Machining tool (2010) Picture of machining tool. In: The website of Nanyang Technological University. Available online: http://www.ntu.edu.sg/. Cited October 2010
8. I-SWARM (2010) Picture of micro robot. In: The website of I-SWARM group. Available online: http://www.i-swarm.org/MainPage/Robots/R_Images1.htm. Cited April 2010

9. Woem H, Szymanski M, Seyfried J et al (2006) The I-SWARM project. Proceedings of the 15th IEEE International Symposium on Robot and Human Interactive Communication (RO-MAN06), 492–496, Hatfield, UK, September 6-8, 2006.
10. Urban Junkie (2010) Picture of pick and place manipulator. In: The website of Carl's Electronics. Available online: http://www.urbanjunkie.co.uk/product.php/1200/0/robot-arm. Cited October 2010
11. Nagasawa H, Honda S et al (2000) Development of a spherical motor manipulated by four wires. Proceedings of American Society for Precision Engineering, vol. 22:219–221, Scottsdale, Arizon, 2000.
12. Amano T, Ishii T, Nakamura K, Ueha S et al (1998) An ultrasonic actuator with multi-degree of freedom using bending and longitudinal vibrations of a single stator. Proceedings of 1998 IEEE International Ultrasonic Symposium L-5, vol. 22:667–670, Sendai, Japan, October 1998.
13. Aoyagi M, Beeby S P, White N M et al (2002) A Novel Multi-Degree-of-Freedom Thick-Film Ultrasonic Motor. IIEEE Transactions, on Ultrasonics, Ferroelectrics and Frequency Control, vol. 49, no. 2:151–158, February 2002.
14. Purwanto E, Toyama S et al (2001) Development of an ultrasonic motor as a fine-orienting stage. IEEE Transactions on Robotics and Automation, vol. 17, no. 4:464–471, 2001.
15. Purwanto E, Toyama S et al (2003) Control method of a spherical ultrasonic motor. Proceedings of 2003 IEEE/ASME International Conference on Advanced Intelligent Mechatronics, vol. 2:464–471, Kobe, Japan, 20–24 July 2003.
16. Toyama Lab. (2005) Picture of ultrasonic spherical motor. In: The website of Tokyo University of Agriculture and Technology. Available online: http://www.tuat.ac.jp/toyama/. Cited May 2005
17. Toyama S, Shigeru S, Zhang G et al (1994) Multi-degree-of-freedom spherical ultrasonic motor. Proceedings of 1994 IEEE International Conference on Industrial Electronics, Control and Instrumentation, 900–905, Italy, September 1994.
18. Fukaya N, Toyama S, Asfour T, Dillmann R et al (2000) Design of the TUAT/Karlsruhe Humannoid Hand. Proceedings of 2000 IEEE/RSJ International Conference on Intelligent Robots and Systems, 1754–1759, Takamatsu, Japan, October 30–November 5, 2000.
19. Toyama S, Hatae S, Nonaka M et al (1991) Development of multi-degree-of-freedom spherical ultrasonic motor. Proceedings of 1991 IEEE International Conference on Advanced Robotics, Robots in Unstructured Environments, vol. 1:55–60, Pisa, Italy, 19–22 June 1991.
20. Takemura K, Ohno Y, Maeno T et al (2001) Design of a Plate Type Multi-DOF Ultrasonic Motor and Its Self-Oscillation Driving Circuit. IEEE Transactions on Mechatronics, vol. 9, no. 3:474–479, September 2004.
21. Takemura K, Ohno Y, Maeno T et al (2003) Design of a Plate Type Multi-DOF Ultrasonic Motor and its Driving Characteristics. Proceedings of 2003 IEEE/ASME International Conference on Advanced Intelligent Mechatronics (AIM 2003), 1309–1312, Kobe, Japan, 23–26 July 2003.
22. Williams F C, Laithwaite E R, Eastham J F et al (1959) Development and design of spherical induction motors. Proceedings of Inst. Electr. Eng., 106:471–847, Decemeber 1959.
23. Davey K, Vachtsevanos G, Powers R et al (1987) The analysis of fields and torques in spherical induction motors. IEEE Transactions on Magnetics, vol. 9, no. 1:273–282, January 1987.
24. Vachtevanos G J, DaveyDavey K et al (1988) Spherical Motor Particularly Adapted for Robotics. US Patent, 4739241, April 1988.
25. Vachtevanos G J, Davey K, Lee K M et al (1987) Development of a Novel Intelligent Robotic Manipulator. IEEE Control Systems Magazine, vol. 7, no. 3:9–15, June 1987.
26. Lee K M, Vachtsevanos G, Kwan C K et al (1988) Development of a spherical stepper wrist motor. Proceedings of the IEEE International Conference on Robotics and Automation, vol. 1:267–272, 24–29 April 1988.
27. Lee K M, Vachtsevanos G, Kwan C K et al (1988) Development of a spherical stepper wrist motor. Journal of Intelligent and Robotic Systems, vol. 1, no. 3:225–242, 24–29, 1988.

28. Lee K M, Kwan C K et al (1991) Design concept development of a spherical stepper for robotic applications. IEEE Transactions on Robotics and Automation, vol. 7, no. 1:175–181, February 1991.
29. Lee K M, Arjunan S et al (1988) Force/torque sensing and micro-motion manipulation of a spherical stepping wrist motor. Proceedings of the 1988 Joint American Control Conference (ACC), vol. 1:950–955, 15–17 June 1988.
30. Lee K M, Pei J et al (1991) Multi-degree-of-freedom spherical permanent magnet motors. Proceedings of 1991 Fifth International Conference on Robots in Unstructured Environments, vol. 1:72–77, Pisa, Italy, 19–22 June 1991.
31. Lee K M, Arjunan S et al (1991) A three-degrees-of-freedom micromotion in-parallel actuated manipulator. IEEE Transactions on Robotics and Automation, vol. 7, no. 15:634–641, October 1991.
32. Lee K M, Sosseh R A et al (2002) Effects of the Torque Model on the Control of a VR Spherical Motor. Proceedings of the 2nd IFAC Conference on Mechatronic Systems, Berkeley, California, USA, 9–11 December 2002.
33. Zhou Z, Lee K M et al (1994) Characterization of a Three Degrees-of-Freedom Variable-Reluctance Spherical Motor. Journal of Systems Engineering, (Special Issue on Motion Control), vol. 4:60–69, 1994.
34. Lee K M, Sosseh R A et al (2000) Effects of Fixture Dynamics on Back-stepping Control of a VR Spherical Motor. Proceedings of the 7th International Conference on Robotics, Automation and Computer Vision, vol. 1:384–389, Singapore, 2–5 December 2000.
35. Lee K M, Wei Z Y, Joni J et al (2004) Parametric Study on Pole Geometry and Thermal Effects of a VRSM. Proceedings of the 2004 IEEE Conference on Robotics, Automation and Mechatronics, 548–553, Singapore, 1–3 December 2004.
36. Lee K M, Wei Z Y, Joni J et al (2004) Design Method for Prototyping a Cost-effective VR Spherical Motor. Proceedings of the 2004 IEEE Conference on Robotics, Automation and Mechatronics, 542–547, Singapore, 1–3 December 2004.
37. Lee K M, Roth R B, Zhou Z et al (1996) Dynamic modeling and control of a ball-joint-like variable-reluctance spherical motor. ASME Journal of Dynamic Systems, Measurement, and Control, vol. 118:29–40, March 1996.
38. Pei J (1990) Methodology of Design and Analysis of Variable-Reluctance Spherical Motors. Thesis of Georgia Institute of Technology, GA, USA, 1994.
39. Roth R B (1992) An Experimental Investigation and Optimization of a Variable Reluctance Spherical Motor. Thesis of Georgia Institute of Technology, GA, USA, 1992.
40. Zhou Z (1995) Real-Time Control and Characterization of a Variable Reluctance Spherical Motor. Thesis of Georgia Institute of Technology, GA, USA, May 1995.
41. He T (2000) Effects of Rotor Configurations on the Characteristic Torque of a Variable-Reluctance Spherical Motor. Thesis of Georgia Institute of Technology, GA, USA, July 2000.
42. Sosseh R A (2001) Finite Element Torque Modeling and Backstepping Control of a Spherical Motor. Thesis of Georgia Institute of Technology, GA, USA, December 2001.
43. Lee K M, Son H, Joni J et al (2005) Concept Development and Design of a Spherical Wheel Motor (SWM). Proceedings of the 2005 IEEE International Conference on Robotics and Automation, 3652–3657, Barcelona, Spain, April 2005.
44. Lee K M, Son H et al (2005) Torque model for design and control of a spherical wheel motor. Proceedings of the 2005 IEEE/ASME International Conference on Advanced Intelligent Mechatronics, 335–340, Monterey, California, USA, 24–28 July 2005.
45. Lee K M, Bai K, Lim Zhou J et al (2009) Dipole Models for Forward/Inverse Torque Computation of a Spherical Motor. IEEE/ASME Transactions on Mechatronics, vol. 14, no. 1:46–54, February 2009.
46. Cho C, Kang D, Kim S, Won S, Lee J et al (2008) Using Mathematical Method of Torque Simulation for Reducing Calculation Time of Permanent Magnet Spherical Wheel Motor. Proceedings of the International Conference on Electrical Machines and Systems, 3112–3115, Wuhan, China, October 2008.

47. Kang D W, Kim W H, Go S C, Jin C S, Won S H, Koo D H, Lee J et al (2009) Method of Current Compensation for Reducing Error of Holding Torque of Permanent-Magnet Spherical Wheel Motor. IEEE Transactions on Magnetics, vol. 45, no. 6, 2819–2822, June 2009.
48. Hollis R L, Salcudean S, Allan A P et al (1987) A six degree-of-freedom magnetically levitated variable compliance fine motion wrist. Proceedings of the 4th International Symposium on Robotics Research (MIT Press), 65–73, Santa Cruz, California, USA, 9–14 August 1987.
49. Unger B J, Nicolaidis A, Berkelman P J, Thompson A, Lederman S, Klatzky R L, Hollis R L et al (2002) Virtual peg-in-hole performance using a 6-DOF magnetic levitation haptic device: comparison with real forces and with visual guidance alone. Proceedings of the 10th Symposium on Haptic Interfaces for Virtual Enviroment & Teleoperator System, 263–270, Orlando, Florida, USA, 24–25 March 2002.
50. Oh S R, Hollis R L, Salcudean S E et al (2002) Precision assembly with a magnetically levitated wrist. Proceedings of IEEE Robotics and Automation, vol. 1:127–134, Atlanta, Georgia, USA, 2–6 May 1993.
51. Salcudean S E, Hollis R L et al (1988) A magnetically levitated fine motion wrist: kinematics, dynamics and control. Proceedings of IEEE Robotics and Automation, vol. 1:261–266, Philadelphia, Pennsylvania, USA, 24–29 April 1988.
52. Hollis R L, Salcudean S E, Allan A P et al (1991) A six-degree-of-freedom magnetically levitated variable compliance fine motion wrist: Design, Modeling and Control. IEEE Transactions on Robotics and Automation, vol. 7, no. 3:320–332, 24–29 June 1991.
53. Berkelman P J, Hollis R L, Baraff D et al (1999) Interaction with a realtime dynamic environment simulation using a magnetic levitation haptic interface device. Proceedings of the 1999 IEEE International Conference on Robotics and Automation, 3261–3266, Detroit, Michigan, USA, 10–15 May 1999.
54. Hollis R L (1989) Six-DOF magnetically levitated fine motion robot wrist with programmable compliance. US Patent, 4874998, October 1989.
55. Foggia A, Oliver E, Chappuis F et al (1988) A new three degrees of freedom electromagnetic actuator. Industry Applications Society Annual Meeting, Conference Record of the 1988 IEEE, New York, USA, vol. 35:137–141, July 1988.
56. Kaneko K, Yamada I, Itao K et al (1988) A spherical DC servo motor with three degrees of freedom. ASME Dyn. Syst. Contr. Div. vol. 11:433–443, 1988.
57. Bederson B B, Wallace R S, Schwart E L et al (1993) Control and design of the spherical pointing motor. Proceedings of the 1993 IEEE International Conference on Robotics and Automation, Atlanta, USA, vol. 35:630–636, May 1993.
58. Bederson B B, Wallace R S, Schwart E L et al (1994) A miniature pan-tilt actuator: the spherical pointing motor. IEEE Transactions on Robotics and Automation, vol. 10, no. 3:298–308, June 1994.
59. Bederson B B (1992) A miniature space-variant active vision system: Cortex-I. Thesis of New York University, New York, USA, June 1992.
60. Bederson B B, Wallace R S, Schwart E L et al (1992) Two miniature pan-tilt devices. Proceedings of the 1992 IEEE International Conference on Robotics and Automation, Nice, France, vol. 35:658–663, May 1992.
61. Bederson B B, Wallace R S, Schwart E L et al (1992) A miniaturized active vision system. Proceedings of 11th IAPR International Conference D: on Architechtures for Vision and Pattern Recognition, Hague, Netherlands, vol. 35:58–61, 30 August–3 September 1992.
62. Wang J, Jewell G W, Howe D et al (1998) Analysis, design and control of a novel spherical permanent-magnet actuator. IEE Proceedings: Electric Power Applications, Hague, Netherlands, vol. 145, no. 1:61–71, January 1998.
63. Wang J, Jewell G W, Howe D et al (1997) Modelling of a novel spherical permanent magnet actuator. Proceedings of 1997 IEEE International Conference on Robotics and Automation, Hague, Netherlands, vol. 145, no. 1:1190–1195, Albuquerque, New Mexico, USA, April 1997.
64. Wang J, Mitchell K, Jewell G W, Howe D et al (2001) Multi-degree-of-freedom spherical permanent magnet motors. Proceedings of 2001 IEEE International Conference on Robotics

and Automation, Hague, Netherlands, vol. 145, no. 1:1798–1805, Seoul, Korea, 21–26 May 2001.
65. Wang J, Jewell G W, Howe D et al (1998) Spherical actuators with multiple degrees-of-freedom. IEE Colloquium on Limited motion electrical actuation systems, Hague, Netherlands, no. 1998/494:8/1–8/6, Seoul, Korea, 13-15 October 1998.
66. Wang J, Jewell G W, Howe D et al (1997) A novel spherical actuator: design and control. IEEE Transactions on Magnetics, vol. 33, no. 5:4209–4211, September 1997.
67. Wang W, Wang J, Jewell G W, Howe D et al (2003) Design and control of a novel spherical permanent magnet actuator with three degrees of freedom. IEEE/ASME Transactions on Mechatronics, vol. 8, no. 4:457–468, December 2003.
68. Wang J, Jewell G W, Howe D et al (2003) Analysis of a spherical permanent magnet actuator. Journal of Applied Physics, vol. 81, no. 8:4266–4268, April 1997.
69. Mitchell J K, Jewell G W, Wang J, Bingham C M, Howe D et al (2002) Influence of an aperture on the performance of a two-degree-of-freedom iron-cored spherical permanent-magnet actuator. IEEE Transactions on Magnetics, vol. 38, no. 6:3650–3653, November 2002.
70. Wang J, Wang W, Jewell G W, Howe D et al (1998) A novel spherical actuator with three degrees-of-freedom. IEEE Transactions on Magnetics, vol. 34, no. 4:2078–2080, July 1998.
71. Wang J, Jewell G W, Howe D et al (1997) Development of a novel spherical permanent magnet actuator. IEE Colloquium on New Topologies for Permanent Magnet Machines, no. 1997/090:8/1–8/10, 18 June 1997.
72. Oner Y, Cetin E, Yilanci A, Ozturk H K et al (2009) Design and Open Loop Control of a Spherical Motor. Applied Electronics, 191–194, 9–10 September 2009.
73. Weck M, Reinartz T, Henneberger G, De Doncker R W et al (2000) Design of a spherical motor with three degrees of freedom. 2000 International CIRP Design Seminar: Design with Manufacturing: Intelligent Design Concepts Methods and Algorithms, vol. 49, no. 1:289–294, 16–18 May 2000.
74. Stein D, Chirikjian G S et al (2000) Experiments in the commutation and motion planning of a spherical stepper motor. Proceedings of DETC'00 ASME 2000 Design Engineering Technical Conferences and Computers and Information in Engineering Conference, 1–7, Baltimore, MD, USA, September 2000.
75. Chirikjian G S, Stein D et al (1999) Kinematic design and commutation of a spherical stepper motor. IEEE/ASME Transactions on Mechatronics, vol. 4, no. 4:342–353, December 1999.
76. Stein D, Chirikjian G S, Scheinerman E R et al (1999) Mathematical models of binary spherical-motion encoders. IEEE/ASME Transactions on Mechatronics, vol. 8, no. 2:234–244, June 2003.
77. Stein D, Chirikjian G S, Scheinerman E R et al (1999) Theory, design, and implementation of a spherical encoder. Proceedings of 2001 IEEE International Conference on Robotics and Automation, vol. 2:1773–1779, Seoul, Korea, 21–26 May 2001.
78. Chirikjian G S (2005) John Hopkins University. In: The website of the Spherical motor project. Available online: http://caesar.me.jhu.edu/research/spherical_motor.html. Cited May 2005
79. Li Z (2009) Robust Control of PM Spherical Stepper Motor Based on Neural Networks. IEEE Transactions on Industrial Electronics, vol. 56, no. 8:2945–2954, August 2009.
80. Ebihara D, Katsuyama N, Kajioka M et al (2001) An Approach to Basic Design of the PM-type Spherical Motor. Proceedings of the 2001 IEEE International Conference on Robotics and Automation, Seoul, Korea, 21–26 May 2001.
81. Ikeshita S, Gofuku A, Kamegawa T, Nagai Ta et al (2009) Development of a spherical motor driven by electro-magnets. Journal of Mechanical Science and Technology, vol. 24:43–46, October 2009.
82. Um Y, Yano T et al (2009) Characteristic of Torque on Spherical Stepping Motor based on Hexahedron-Octahedron Structure. Proceedings of the IEEE International Conference on Mechatronics and Automation, Changchun, China, 9–12 August 2009.
83. Xia C, Li H, Shi T et al (2008) 3-D Magnetic Field and Torque Analysis of a Novel Halbach Array Permanent-Magnet Spherical Motor. IEEE Transactions on Magnetics, vol. 44, no. 8:2016–2020, August 2008.

84. Guo C, Xia C et al (2007) A Dynamic Decoupling Control Algorithm for Halbach Array Permanent Magnet Spherical Motor Based on Computed Torque Method. Proceedings of the 2007 IEEE International Conference on Robotics and Biomimetics, 2090–2094, Sanya, China, 15–18 December 2007.
85. Uenoa T, Saitob C, Imaizumib N, Higuchia T et al (2009) Miniature spherical motor using iron gallium alloy (Galfenol). Sensors and Actuators A: Physical, vol. 154:92–96, April 2009.
86. Gieras J F, Wing M et al (1998) Permanent Magnet Motor Technology. Marcel Dekker Inc., New York, 1998.

Chapter 2
Magnetic Field Modeling

2.1 Introduction

Magnetic field modeling of the spherical actuator refers to the formulation of magnetic flux density distribution of the PM-pole rotor. There are mainly two purposes for the magnetic field modeling of the spherical actuator. First, torque modeling is necessary for position and velocity control of the spherical actuator. According to Lorentz force law, one prerequisite of the torque modeling is to formulate the magnetic field distribution of the PM-pole rotor analytically. Second, the magnetic field model facilitates the simulation and comprehension of the flux density variation of the PM-pole rotor.

Various magnetic field modeling approaches have been investigated by other researchers. A method based on Maxwell equations has been proposed by Prieto *et al*. [1] to obtain the magnetic component model for planar structures successfully. This method is applicable to one-dimensional (1D) magnetic field, i.e. the magnetic field vector has a constant direction. As an improvement, by using quasi-Poissonian/Laplace's equations in polar coordinates, Zhu *et al*. [2, 3] have developed an analytical technique to predict the 2D magnetic field distribution of single-axis brushless PM machines. Similar approaches have been utilized by Cho *et al*. [4] to analyze the 2D magnetic field of a planar motor, and by Polinder *et al*. [5] to analyze the 2D magnetic field in the cylindrical airgap of a PM generator. For many practical cases, the magnetic field with 3D distribution requires different approaches for modeling. Xiong *et al*. [6] have proposed an analytical method of the magnetic field for a linear PM synchronous machine by using the concept of magnetic charge. A general analysis on the magnetic field of a spherical induction motor was introduced by Davey *et al*. [7] using magnetic vector potential. The analysis properly accounts for the diffusion of the magnetic field with changing frequency and motor speed. Wang *et al*. [8, 9] have proposed 2D/3D magnetic field modeling methods based on Laplace's equation in spherical coordinates for two spherical actuators. In these models, pole arrangements like two or four PM poles and three or four windings, are considered. The rotor is in principle regarded as a sphere entirely consisting

L. Yan et al., *Design, Modeling and Experiments of 3-DOF Electromagnetic Spherical Actuators*, Mechanisms and Machine Science 4,
DOI 10.1007/978-94-007-1646-9_2,

of magnetized rare-earth materials. This approach shows less flexibility in actuator design and system analysis to a certain extent. Prieto *et al*. [10] have presented a procedure to obtain the energy in 3D magnetic structures by applying the *Double 2D* methodology. An accurate model of the magnetic component can be obtained from the magnetic field energy. This approach is based on finite-element analysis (FEA), and thus is not suitable for system control.

The challenge of mathematic modeling of PM-pole rotor in spherical actuators lies in: 1. there are three components of flux density at every point of the 3D space; 2. each of these components varies with respect to the specific locations. In this chapter, an analytical modeling method based on Laplace's equation is proposed for the 3D magnetic field of PM-pole rotor. The PM poles are described by generic variables related to the formulation of the magnetic field. Laplace's equations are formulated for deriving the general solution of magnetic scalar potential. Then the analytical solution of magnetic flux density distribution of the PM-pole rotor is obtained with suitable boundary conditions (BCs). With analytical solution of the magnetic flux density, the influence of structure parameters of the rotor on the magnetic field distribution can be studied.

2.2 Configuration of Rotor Poles

When multiple poles are used in a rotor, the PM poles are arranged along the rotor equator in an alternative polarization pattern. Putting a coil between two PMs as shown in Fig. 2.1(b), one neighboring PM will generate an attraction force with it and the other will generate a repulsion force. The attraction and repulsion will move

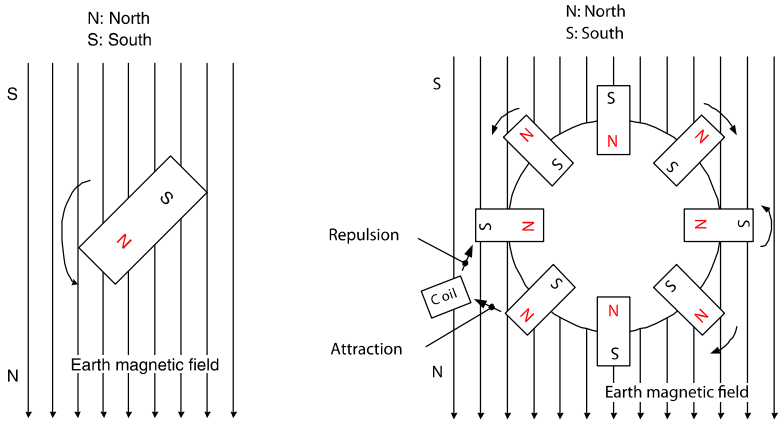

(a) Single PM pole (b) Eight PM poles

Fig. 2.1: Influence of earth magnetic field on rotor poles

the rotor in the same clockwise direction. Therefore, the alternative polarization pattern can achieve larger torque compared with the pattern with same polarization. In order to realize this alternative arrangement in a circle, even number of PM poles are required. Due to the intrinsically high magnetic flux produced by rare-earth magnet as indicated in Fig. 2.1(a), the rotor tends to align itself to the earth magnetic field. This phenomenon is analogous to the effect of earth magnetic field to the compass needle. Having even number of poles distributed uniformly around the equator of the rotor is a method to reduce the inherent self-inducing torque generated by the earth magnetic field at the center of the rotor (Fig. 2.1(b)).

Figure 2.2(a) illustrates the shape of a single rotor pole - an approximated dihedral cone enclosed by *ABCD* and *abcd*. The dihedral cone can be specified by four parameters: longitudinal angle α, latitudinal angle β, rotor radius R_r and rotor core radius R_b. Modeling a single pole as a dihedral cone has several benefits. First, due to the 3-DOF spherical motion of the rotor, the spherical surface of the dihedral-cone-shaped pole can avoid the interference between coils and PM poles, whilst making use of the working space of the rotor completely. Second, the volume of the rotor pole can be specified in spherical coordinates, which facilitates the formulation of the actuator torque. Third, by varying the parameters of the dihedral cone, R_b, R_r, α and β, the study of optimal magnet-pole pattern can be carried out. Figure 2.2(b) presents the PM poles in alternate magnetization directions placed around the equator of the rotor. There are air slots in between PM poles. The regions on top and bottom of the rotor can also be air or low-density materials such as aluminum. These air slots generalize the study of pole arrangement and decreases the inertia moment of the rotor.

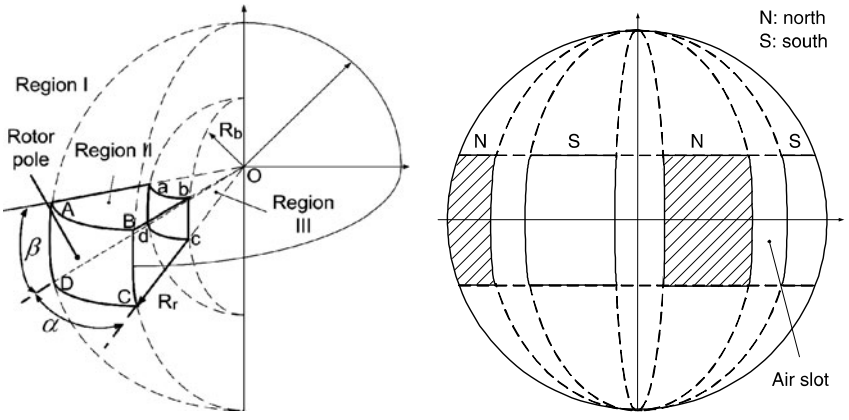

(a) Single rotor pole (b) Alternately arranged rotor pole

Fig. 2.2: Arrangement of rotor poles

2.3 Magnetic Scalar Potential

In the formulation of the magnetic field, the rotor space under study is divided into three regions based on their magnetic characteristics. The air space outside the rotor is denoted as Region *I*. The volume enclosed by *ABCD* and *abcd*, the PM pole (filled with rare-earth magnetic material), is denoted as Region *II*. The inner core enveloped by *abcdo* filled with ferromagnetic materials such as soft iron is denoted as Region *III*. The ferromagnetic core in Region *III* can "converge" the magnetic flux created by PM poles and reduce the magnetic energy loss. It is found that filling Region *III* with magnetized rare-earth material does not have significant improvement on the strength of the magnetic flux density. Rather, the inertia moment of the rotor increases and the dynamic performance of the rotor will be affected.

2.3.1 Relations Between H and B for Three Regions

Region *I* (air) and *III* (iron):

According to the material properties of Region *I* (air) and Region *III* (iron), it is readily to obtain equations relating magnetic field intensity **H** (A/m) to flux density **B** (T) for these two regions [11]:

$$\mathbf{B}_I = \mu_0 \mathbf{H}_I, \tag{2.1}$$

$$\mathbf{B}_{III} = \mu_0 \mu_r \mathbf{H}_{III}, \tag{2.2}$$

where μ_0 is permeability of the free space with a value of $4\pi \times 10^{-7}$H/m, dimensionless quantity μ_r is the relative permeability of soft iron having typical value larger than 4000.

Region *II* (PM):

PM can be characterized by a hysteresis loop which relates **H** to **B**. Figure 2.3(a) presents a typical full hysteresis loop or B-H curve for a rare-earth magnet. From the figure, it can be seen that the variation of **B** always lags behind that of **H**. This phenomenon is called hysteresis of PMs. The second quadrant of the B-H curve, commonly referred to as the demagnetization curve, describes the behavior of magnetic characteristics in actual use. According to Fig. 2.3(b), it can be found that rare-earth magnet exhibits high coercivity and nearly linear demagnetization property. The slope of this demagnetization curve is defined as the recoil permeability μ_{rec} (H/m), or $\mu_0 \mu_m$, where dimensionless quantity μ_m is called relative recoil permeability of magnet having typical value between 1.05 and 1.20. Therefore, for Region *II* (PM) of the rotor, the demagnetization curve can be represented by [11]

$$\mathbf{B}_{II} = \mu_0 \mu_m \mathbf{H}_{II} + \mu_0 \mathbf{M}_0, \tag{2.3}$$

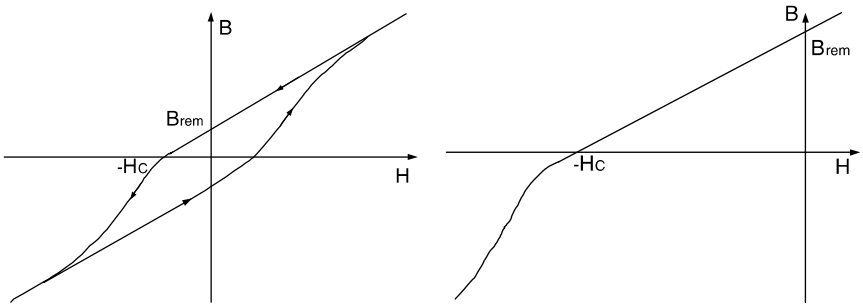

(a) Full hysteresis loop (b) Second quadrant

Fig. 2.3: Typical hysteresis loop of rare-earth magnet

where $\mathbf{M}_0 = \mathbf{B}_{rem}/\mu_0$ (A/m) is the residual magnetization vector and $\mathbf{B}_{rem}$ (T) is remanence of PM.

2.3.2 *Laplace's Equations for Three Regions*

By using the relations between $\mathbf{H}$ and $\mathbf{B}$ in Eqns. (2.1)-(2.3), Laplace's equations for three regions of the rotor space can be derived as follows.

Magnetic intensity $\mathbf{H}$ vs. scalar potential Φ:

It is known that for three regions of the rotor space, following equation can be obtained [12]

$$\nabla \times \mathbf{H}_i = 0, \tag{2.4}$$

where $i = I$, II and III. Eqn. (2.4) means that $\mathbf{H}_i$ is an irrotational field. According to Helmholtz's theorem [13], the magnetic intensity can be expressed as the gradient of a scalar potential Φ_i, i.e.,

$$\mathbf{H}_i = -\nabla \Phi_i. \tag{2.5}$$

Using the spherical coordinates (r, θ, ϕ), the magnetic field intensity $\mathbf{H}_i$ can be expressed as

$$\begin{aligned}\mathbf{H}_i &= H_{ir}\mathbf{e}_r + H_{i\theta}\mathbf{e}_\theta + H_{i\phi}\mathbf{e}_\phi \\ &= -\left(\frac{\partial \Phi_i}{\partial r}\mathbf{e}_r + \frac{1}{r}\frac{\partial \Phi_i}{\partial \theta}\mathbf{e}_\theta + \frac{1}{r\sin\theta}\frac{\partial \Phi_i}{\partial \phi}\mathbf{e}_\phi\right),\end{aligned}$$

where $\mathbf{e}_r$, $\mathbf{e}_\theta$ and $\mathbf{e}_\phi$ are unit vectors in r, θ and ϕ directions respectively. H_{ir}, $H_{i\theta}$ and $H_{i\phi}$ are three components of the magnetic field intensity $\mathbf{H}_i$, where

$$H_{ir} = -\frac{\partial \Phi_i}{\partial r}, \quad H_{i\theta} = -\frac{1}{r}\frac{\partial \Phi_i}{\partial \theta}, \quad H_{i\phi} = -\frac{1}{r\sin\theta}\frac{\partial \Phi_i}{\partial \phi} \quad . \tag{2.6}$$

According to Maxwell equations [14], a source-free or solenoidal magnetic field has the following property

$$\nabla \cdot \mathbf{B}_i = 0, \tag{2.7}$$

where $i = I$, II and III.

Laplace's equation for outside rotor (Region I):

Outside the rotor (Region I), substituting Eqn. (2.1) into Eqn. (2.5) and Eqn. (2.7), we have

$$\nabla \cdot \mathbf{B}_I = \nabla \cdot (\mu_0 \mathbf{H}_I) = \nabla \cdot [\mu_0(-\nabla \Phi_I)] = 0.$$

Thus,

$$\nabla^2 \Phi_I = 0, \tag{2.8}$$

where ∇^2 is Laplacian operator and Φ_I is the scalar potential in Region I (air).

Laplace's equation for PM (Region II):

Similarly, from Eqns. (2.3), (2.5) and (2.7), following equation can be obtained readily

$$\nabla \cdot \mathbf{B}_{II} = \nabla \cdot [-\mu_0 \mu_m (\nabla \Phi_{II})] + \nabla \cdot (\mu_0 \mathbf{M}_0) = 0,$$

which yields

$$-\mu_m \nabla^2 \Phi_{II} + \nabla \cdot \mathbf{M}_0 = 0,$$

that is

$$\nabla^2 \Phi_{II} = \nabla \cdot \mathbf{M}_0 / \mu_m. \tag{2.9}$$

Eqn. (2.9) is in the form of Poisson's equation. Due to symmetry of the rotor pole arrangement, the divergence of the residual magnetization vector is equal to zero, i.e., $\nabla \cdot \mathbf{M}_0 = 0$. The Poisson's equation can be reduced to Laplace's equation as

$$\nabla^2 \Phi_{II} = 0. \tag{2.10}$$

Laplace's equation for iron core (Region III):

Similar to Region I, scalar potential Φ_{III} of the soft iron core (Region III) can also be obtained as

$$\nabla^2 \Phi_{III} = 0. \tag{2.11}$$

2.3.3 General Solution of Laplace's Equation

In the spherical coordinates, the Laplace's equation can be expressed as

$$\frac{1}{r^2}\frac{\partial}{\partial r}(r^2\Phi_i) + \frac{1}{r^2\sin\theta}\frac{\partial}{\partial\theta}(\sin\theta\frac{\partial\Phi_i}{\partial\theta}) + \frac{1}{r^2\sin^2\theta}\frac{\partial\Phi_i}{\partial\phi} = 0, \tag{2.12}$$

where $i = I$, II and III, indicating the region of concern. Using separation of variables method, the scalar potential Φ_i can be represented as $\Phi_i(r,\theta,\phi) = R_i(r)\Theta_i(\theta)\Psi_i(\phi)$, where $R_i(r)$, $\Theta_i(\theta)$ and $\Psi_i(\phi)$ are functions of the spherical coordinates. Substituting $\Phi_i(r,\theta,\phi)$ into Eqn. (2.12), the general solution of the scalar potential Φ_i is expressed as [15]

$$\Phi_i = \sum_{n=0}^{\infty}\sum_{m=-n}^{n}[\kappa_{ni}^m r^n + \xi_{ni}^m r^{-(n+1)}][Y_n^m(\theta,\phi)], \tag{2.13}$$

where κ_{ni}^m and ξ_{ni}^m are constants to be determined by boundary conditions. $Y_n^m(\theta,\phi)$ is the spherical harmonic functions defined by

$$Y_n^m(\theta,\phi) = \sqrt{\frac{2n+1}{4\pi}\frac{(n-m)!}{(n+m)!}}[P_n^m(\cos\theta)]e^{im\phi},$$

where $P_n^m(\cos\theta)$ is associated Legendre functions, and n, m are integers with $-n \leq m \leq n$. Note that spherical harmonics are complex valued functions.

2.4 Spherical Harmonic Expansion of M_{0r}

Let M_0 be the magnitude of the residual magnetization vector $\mathbf{M}_0$. With reference to Fig. 2.4 that illustrates the poles placement on the equatorial plane of the rotor, the constituents M_{0r}, $M_{0\theta}$ and $M_{0\phi}$ of $\mathbf{M}_0$ in the directions $\mathbf{e}_r$, $\mathbf{e}_\theta$ and $\mathbf{e}_\phi$ can be computed as

$$M_{0r} = (-1)^{p-1}M_0\cos[\phi - \alpha_0 - \frac{2\pi}{P}(p-1)]\sin\theta, \tag{2.14}$$

$$M_{0\theta} = (-1)^{p-1}M_0\cos[\phi - \alpha_0 - \frac{2\pi}{P}(p-1)]\cos\theta, \tag{2.15}$$

$$M_{0\phi} = (-1)^{p}\ M_0\sin[\phi - \alpha_0 - \frac{2\pi}{P}(p-1)], \tag{2.16}$$

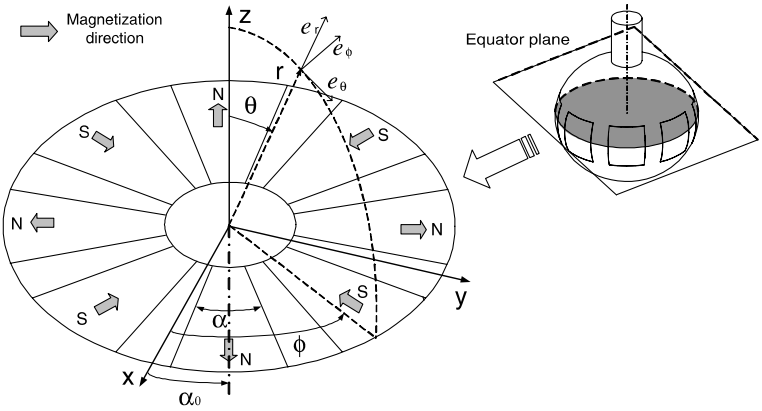

Fig. 2.4: Poles on the equatorial plane of the rotor in spherical coordinates

where $p = 1, 2, ..., P$. P is the total number of PM poles. In this study, $P = 8$, and α_0 is the PM pole angle at the center line in ϕ-direction. Note that these equations are only valid within the range of

$$\frac{\pi}{4}(p-1) + \alpha_0 - \frac{\alpha}{2} < \phi < \frac{\pi}{4}(p-1) + \alpha_0 + \frac{\alpha}{2}, \tag{2.17}$$

$$\frac{\pi}{2} - \frac{\beta}{2} < \theta < \frac{\pi}{2} + \frac{\beta}{2}, \tag{2.18}$$

in the PM pole (Region *II*). For the rest non-magnetized regions in the rotor, the residual magnetization is equal to zero.

When applying boundary conditions to solve the unknowns in the general solution of scalar potential, only the radial component of residual magnetization vector M_{0r} will be used to express the flux density continuity between regions. Components $M_{0\theta}$ and $M_{0\phi}$ do not exist in any boundary condition. The radial component can be expressed as an expansion of spherical harmonic functions $Y_n^m(\theta, \phi)$ as [9]:

$$M_{0r}^s(\theta, \phi) = \sum_{n=0}^{\infty} \sum_{m=-n}^{n} C_{nm} Y_n^m(\theta, \phi), \tag{2.19}$$

where C_{nm} are coefficients determined from the surface integral of the following form:

$$C_{nm} = \int_0^{\pi} \int_0^{2\pi} M_{0r}(\theta, \phi) Y_n^{m*}(\theta, \phi) \sin\theta d\theta d\phi, \tag{2.20}$$

and $Y_n^{m*}(\theta, \phi)$ denotes the complex conjugate of $Y_n^m(\theta, \phi)$. Substituting Eqn. (2.14) into Eqn. (2.20) gives the coefficients

$$C_{nm} = M_0 \int_0^{2\pi} f(\phi) e^{-im\phi} d\phi \int_0^{\pi} \sqrt{\frac{2n+1}{4\pi} \frac{(n-m)!}{(n+m)!}} [P_n^m(\cos\theta)] \sin^2\theta d\theta, \quad (2.21)$$

where

$$f(\phi) = (-1)^{p-1} \cos[\phi - \alpha_0 - \frac{\pi}{4}(p-1)], \; p = 1, 2, ..., 8. \quad (2.22)$$

It is found that $C_{nm} \neq 0$ if and only if $m = \pm 4, \pm 12, \pm 20, ...$ Thus, the fundamental terms of the spherical harmonic functions can be taken at $n = 4$ and $m = \pm 4$. For simplicity, only these terms are used for the derivation of the magnetic field. Denote

$$a \pm bi \equiv \int_0^{2\pi} f(\phi) e^{-im\phi} d\phi \quad (m = 4 \text{ and } m = -4), \quad (2.23)$$

$$c/\sqrt{\pi} \equiv \int_0^{\pi} \sqrt{\frac{2n+1}{4\pi} \frac{(n-m)!}{(n+m)!}} \sin^2\theta [P_n^m(\cos\theta)] d\theta, \quad (2.24)$$

where a, b and c are real numbers. As M_{0r} is available within the range defined by Eqns. (2.17) and (2.18), integrals in Eqns. (2.23) and (2.24) are also constrained by the same range. Out of this range, the integrals are equal to zero. It can be verified that the results of the second integral for $m = 4$ and $m = -4$ are the same. Consequently, the coefficients, $C_{4,4}$ and $C_{4,-4}$, can be obtained based on Eqn. (2.21) as

$$C_{4,4} = M_0 \frac{1}{\sqrt{\pi}} (a + bi) c, \qquad C_{4,-4} = M_0 \frac{1}{\sqrt{\pi}} (a - bi) c, \quad (2.25)$$

where $C_{4,-4}$ is the complex conjugate of $C_{4,4}$. Therefore, the radial component, M_{0r}, of the residual magnetization vector can be expressed in terms of spherical harmonics as

$$M_{0r}^s(\theta, \phi) = C_{4,-4} Y_4^{-4}(\theta, \phi) + C_{4,4} Y_4^4(\theta, \phi), \quad (2.26)$$

where $Y_4^{-4} = 3/16\sqrt{35/2\pi} \sin^4\theta e^{-4i\phi}$ and $Y_4^4 = 3/16\sqrt{35/2\pi} \sin^4\theta e^{4i\phi}$.

2.5 Boundary Conditions

Utilizing the boundary conditions in between different regions of the rotor space as well as the spherical harmonic expansion of M_{0r}, coefficients κ_{nI}^m, κ_{nII}^m, κ_{nIII}^m, ξ_{nI}^m, ξ_{nII}^m and ξ_{nIII}^m, in the general solution of magnetic scalar potential of Eqn. (2.13) can be obtained. Because only the flux density in Region *I* can produce actuator force/torque by interacting with the air-core coils, the coefficients κ_{nI}^m and ξ_{nI}^m are of significant importance.

2.5.1 Boundary Condition A or Far Field Boundary Condition ($B_{Ir}|_{r\to\infty}=0$, $B_{I\theta}|_{r\to\infty}=0$ and $B_{I\phi}|_{r\to\infty}=0$)

The magnetic flux density decreases when the radial distance r increases. Three components of the flux density, B_{Ir}, $B_{I\theta}$ and $B_{I\phi}$ tend to zero when $r\to\infty$. According to Eqns. (2.6) and (2.13), the boundary condition $B_{Ir}|_{r\to\infty}=0$ can be written as

$$\begin{aligned} B_{Ir}|_{r\to\infty} &= -\mu_0\frac{\partial\Phi_I}{\partial r}|_{r\to\infty} \\ &= -\mu_0\sum_{n=0}^{\infty}\sum_{m=-n}^{n}[n\kappa_{nI}^m r^{n-1}-(n+1)\xi_{nI}^m r^{-(n+2)}][Y_n^m(\theta,\phi)]|_{r\to\infty}=0. \end{aligned}$$

Through inspection of the exponential terms, it can be concluded that $\kappa_{nI}^m = 0$. With the aid of Eqns. (2.6) and (2.13), the boundary conditions $B_{I\theta}|_{r\to\infty}=0$ and $B_{I\phi}|_{r\to\infty}=0$ can be expressed as follows.

$$\begin{aligned} B_{I\theta}|_{r\to\infty} &= -\mu_0\frac{1}{r}\frac{\partial\Phi_I}{\partial\theta}|_{r\to\infty} \\ &= -\mu_0\sum_{n=0}^{\infty}\sum_{m=-n}^{n}[\kappa_{nI}^m r^{n-1}+\xi_{nI}^m r^{-(n+2)}]\sqrt{\frac{2n+1}{4\pi}\frac{(n-m)!}{(n+m)!}}\frac{\partial[P_n^m(\cos\theta)]}{\partial\theta}e^{im\phi}|_{r\to\infty} \\ &= 0, \\ B_{I\phi}|_{r\to\infty} &= -\mu_0\frac{1}{r\sin\theta}\frac{\partial\Phi_I}{\partial\phi}|_{r\to\infty} \\ &= -\mu_0\sum_{n=0}^{\infty}\sum_{m=-n}^{n}[\kappa_{nI}^m r^{n-1}+\xi_{nI}^m r^{-(n+2)}]\sqrt{\frac{2n+1}{4\pi}\frac{(n-m)!}{(n+m)!}}\frac{P_n^m(\cos\theta)}{\sin\theta}e^{im\phi}(im)|_{r\to\infty} \\ &= 0. \end{aligned}$$

These two conditions lead to the same result $\kappa_{nI}^m = 0$, as that of $B_{Ir}|_{r\to\infty}=0$.

2.5.2 Boundary Condition B ($B_{Ir}|_{r=R_r}=B_{\text{II}r}|_{r=R_r}$)

On the interface of Region *I* (air) and Region *II* (PM) as shown in Fig. 2.5 (a), the components of the flux density B_{Ir} and $B_{\text{II}r}$ are normal to the interfacial surface of the two neighboring medium. Applying the law of conservation of the magnetic flux [17] to the cylindrical volume in Fig. 2.5 (a) and allowing $\Delta h\to 0$, the result of $B_{Ir}\Delta S = B_{\text{II}r}\Delta S$ can be obtained, hence $B_{Ir}|_{r=R_r}=B_{\text{II}r}|_{r=R_r}$, where R_r is the radius of the rotor that defines the spherical boundary between these two regions.

Projecting all terms of Eqn. (2.3) into the r-direction gives

$$B_{\text{II}r} = \mu_0\mu_m H_{\text{II}r}+\mu_0 M_{0r}. \tag{2.27}$$

Substituting Eqn. (2.19) into Eqn. (2.27), the radial component $B_{\mathrm{II}r}$ of magnetic flux density can be expressed as

$$B_{\mathrm{II}r} = \mu_0\mu_m H_{\mathrm{II}r} + \mu_0 \sum_{n=0}^{\infty}\sum_{m=-n}^{n} C_{nm}[Y_n^m(\theta,\phi)]. \tag{2.28}$$

By taking advantage of Eqns. (2.6) and (2.13), Eqn. (2.28) is rewritten as

$$\begin{aligned} B_{\mathrm{II}r} = &-\mu_0\mu_m \sum_{n=0}^{\infty}\sum_{m=-n}^{n} [n\kappa_{n\mathrm{II}}^m r^{n-1} - (n+1)\xi_{n\mathrm{II}}^m r^{-(n+2)}][Y_n^m(\theta,\phi)]|_{r=R_r} \\ &+\mu_0 \sum_{n=0}^{\infty}\sum_{m=-n}^{n} C_{nm}[Y_n^m(\theta,\phi)]. \end{aligned} \tag{2.29}$$

Therefore, the boundary condition $B_{Ir}|_{r=R_r} = B_{\mathrm{II}r}|_{r=R_r}$ is expanded to

$$\begin{aligned} &-\mu_0 \sum_{n=0}^{\infty}\sum_{m=-n}^{n} [-(n+1)\xi_{nI}^m r^{-(n+2)}][Y_n^m(\theta,\phi)]|_{r=R_r} \\ = &-\mu_0\mu_m \sum_{n=0}^{\infty}\sum_{m=-n}^{n} [n\kappa_{n\mathrm{II}}^m r^{n-1} - (n+1)\xi_{n\mathrm{II}}^m r^{-(n+2)}][Y_n^m(\theta,\phi)]|_{r=R_r} \\ &+\mu_0 \sum_{n=0}^{\infty}\sum_{m=-n}^{n} C_{nm}[Y_n^m(\theta,\phi)]. \end{aligned} \tag{2.30}$$

As the spherical harmonics $Y_n^m(\theta,\phi)$ are orthonormal functions [16], Eqn. (2.30) holds for each pair of n and m. The following relation can be subsequently obtained

$$(n+1)\xi_{nI}^m = -\mu_m[n\kappa_{n\mathrm{II}}^m R_r^{2n+1} - (n+1)\xi_{n\mathrm{II}}^m] + C_{nm}R_r^{n+2}. \tag{2.31}$$

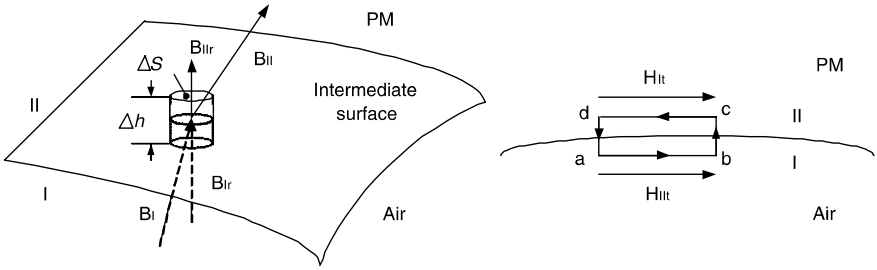

(a) $B_{Ir} = B_{\mathrm{II}r}$ (b) $H_{It} = H_{\mathrm{II}t}$

Fig. 2.5: Continuity boundary conditions

2.5.3 Boundary Condition C ($H_{I\phi}|_{r=R_r} = H_{II\phi}|_{r=R_r}$ and $H_{I\theta}|_{r=R_r} = H_{II\theta}|_{r=R_r}$)

According to Ampere's circuital law [17], the line integral of the magnetic intensity along any closed contour is always equal to the total real current crossing a surface limited by the contour. As shown in Fig. 2.5 (b), a narrow rectangular contour at the boundary surface is indicated by *abcd*. The lengthes of l_{da} and l_{bc} tend to be close to zero. If there is no real surface current on the interface, the result of $H_{IIt}l_{cd} - H_{It}l_{ab} = 0$ can be obtained, i.e., $H_{It} = H_{IIt}$ with $l_{cd} = l_{ab}$, where H_{It} and H_{IIt} are tangent to the surface. For the spherical actuator, there are two components H_θ and H_ϕ of the magnetic field intensity which are tangent to the rotor surface between Region *I* (air) and Region *II* (PM). Therefore, $H_{It} = H_{IIt}$ is rewritten as $H_{I\phi}|_{r=R_r} = H_{II\phi}|_{r=R_r}$ and $H_{I\theta}|_{r=R_r} = H_{II\theta}|_{r=R_r}$, where $r = R_r$ defines the boundary surface between Region *I* (air) and *II* (PM). From Eqns. (2.6) and (2.13), it can be obtained that

$$H_{I\phi} = -\frac{1}{r\sin\theta}\sum_{n=0}^{\infty}\sum_{m=-n}^{n}\xi_{nI}^{m}r^{-(n+1)}\sqrt{\frac{2n+1}{4\pi}\frac{(n-m)!}{(n+m)!}}[P_n^m(\cos\theta)]e^{im\phi}(im),$$

$$H_{II\phi} = -\frac{1}{r\sin\theta}\sum_{n=0}^{\infty}\sum_{m=-n}^{n}[\kappa_{nII}^{m}r^{n} + \xi_{nII}^{m}r^{-(n+1)}]\sqrt{\frac{2n+1}{4\pi}\frac{(n-m)!}{(n+m)!}}[P_n^m(\cos\theta)]e^{im\phi}(im).$$

Substituting these two equations into the boundary condition of $H_{I\phi}|_{r=R_r} = H_{II\phi}|_{r=R_r}$ yields

$$\xi_{nI}^{m}R_r^{-(n+1)} = \kappa_{nII}^{m}R_r^{n} + \xi_{nII}^{m}R_r^{-(n+1)},$$

that is,

$$\xi_{nI}^{m} = \kappa_{nII}^{m}R_r^{2n+1} + \xi_{nII}^{m}. \tag{2.32}$$

Similarly, the following equations can be obtained for the θ-direction

$$H_{I\theta} = -\sum_{n=0}^{\infty}\sum_{m=-n}^{n}\xi_{nI}^{m}r^{-(n+2)}\sqrt{\frac{2n+1}{4\pi}\frac{(n-m)!}{(n+m)!}}\frac{\partial[P_n^m(\cos\theta)]}{\partial\theta}e^{im\phi},$$

$$H_{II\theta} = -\frac{1}{r}\sum_{n=0}^{\infty}\sum_{m=-n}^{n}[\kappa_{nII}^{m}r^{n} + \xi_{nII}^{m}r^{-(n+1)}]\sqrt{\frac{2n+1}{4\pi}\frac{(n-m)!}{(n+m)!}}\frac{\partial[P_n^m(\cos\theta)]}{\partial\theta}e^{im\phi}.$$

From these two equations, it can be verified that the boundary condition of $H_{I\theta}|_{r=R_r} = H_{II\theta}|_{r=R_r}$ yields the same result as Eqn. (2.32).

2.5.4 Finite Boundary Condition D at $r = 0$ ($B_{\text{III}r}|_{r=0} \neq \infty$, $B_{\text{III}\theta}|_{r=0} \neq \infty$ and $B_{\text{III}\phi}|_{r=0} \neq \infty$)

This boundary condition comes from the fact that it is impossible to achieve an infinite value of flux density. According to Eqns. (2.6) and (2.13), the boundary condition, $B_{\text{III}r}|_{r=0} \neq \infty$, can be written as

$$B_{\text{III}r}|_{r=0} = -\mu_0\mu_r \sum_{n=0}^{\infty}\sum_{m=-n}^{n} [n\kappa_{n\text{III}}^m r^{n-1} - (n+1)\xi_{n\text{III}}^m r^{-(n+2)}][Y_n^m(\theta,\phi)]|_{r=0} \neq \infty.$$

This equation indicates that $\xi_{n\text{III}}^m = 0$. It can be verified that $B_{\text{III}\theta}|_{r=0} \neq \infty$ and $B_{\text{III}\phi}|_{r=0} \neq \infty$ yield the same result.

2.5.5 Boundary Condition E ($B_{\text{II}r}|_{r=R_b} = B_{\text{III}r}|_{r=R_b}$)

This boundary condition is similar to BC-B. Following the same development, BC-E results in

$$\begin{aligned} & -\mu_0\mu_r \sum_{n=0}^{\infty}\sum_{m=-n}^{n} [n\kappa_{n\text{III}}^m r^{n-1}][Y_n^m(\theta,\phi)]|_{r=R_b} \\ = \; & -\mu_0\mu_m \sum_{n=0}^{\infty}\sum_{m=-n}^{n} [n\kappa_{n\text{II}}^m r^{n-1} - (n+1)\xi_{n\text{II}}^m r^{-(n+2)}][Y_n^m(\theta,\phi)]|_{r=R_b} \\ & +\mu_0 \sum_{n=0}^{\infty}\sum_{m=-n}^{n} C_{nm}[Y_n^m(\theta,\phi)], \end{aligned} \tag{2.33}$$

that is,

$$\mu_r n\kappa_{n\text{III}}^m R_b^{2n+1} = \mu_m[n\kappa_{n\text{II}}^m R_b^{2n+1} - (n+1)\xi_{n\text{II}}^m] - C_{nm}R_b^{n+2} \tag{2.34}$$

2.5.6 Boundary Condition F ($H_{\text{II}\phi}|_{r=R_b} = H_{\text{III}\phi}|_{r=R_b}$ and $H_{\text{II}\theta}|_{r=R_b} = H_{\text{III}\theta}|_{r=R_b}$)

Following the same procedure of BC-C, $H_{\text{II}\phi}|_{r=R_b} = H_{\text{III}\phi}|_{r=R_b}$ can lead to

$$\begin{aligned} & -\frac{1}{r\sin\theta}\sum_{n=0}^{\infty}\sum_{m=-n}^{n} (\kappa_{n\text{III}}^m r^n)\sqrt{\frac{2n+1}{4\pi}\frac{(n-m)!}{(n+m)!}}[P_n^m(\cos\theta)]e^{im\phi}(im)|_{r=R_b} \\ = & -\frac{1}{r\sin\theta}\sum_{n=0}^{\infty}\sum_{m=-n}^{n} [\kappa_{n\text{II}}^m r^n + \xi_{n\text{II}}^m r^{-(n+1)}]\sqrt{\frac{2n+1}{4\pi}\frac{(n-m)!}{(n+m)!}}[P_n^m(\cos\theta)]e^{im\phi}(im)|_{r=R_b}, \end{aligned}$$

that is

$$\kappa_{n\mathit{III}}^m R_b^{2n+1} = \kappa_{n\mathit{II}}^m R_b^{2n+1} + \xi_{n\mathit{II}}^m. \tag{2.35}$$

$H_{\mathit{II}\theta}|_{r=R_b} = H_{\mathit{III}\theta}|_{r=R_b}$ also yields the same result.

2.5.7 Solution of Coefficients ξ_{nI}^m and κ_{nI}^m

So far, the values or relationships of coefficients ξ_{nI}^m, $\xi_{n\mathit{II}}^m$, $\xi_{n\mathit{III}}^m$, κ_{nI}^m, $\kappa_{n\mathit{II}}^m$ and $\kappa_{n\mathit{III}}^m$ have been derived from boundary conditions. Specifically, BC-A and BC-D produce $\kappa_{nI}^m = 0$ and $\xi_{n\mathit{III}}^m = 0$ respectively; BC-B, BC-C, BC-E and BC-F lead to Eqn. (2.31), (2.32), (2.34) and (2.35) respectively. According to Lorentz force law, only the magnetic field in Region *I* (air) generates actuator torque. Therefore, solutions of ξ_{nI}^m and κ_{nI}^m are important ($\kappa_{nI}^m = 0$). By using Eqns. (2.31), (2.32), (2.34) and (2.35), coefficient ξ_{nI}^m can be calculated as follows.

First, multiplying Eqn. (2.35) by $\mu_r n$ and adding into Eqn. (2.34) yield

$$(\mu_r - \mu_m) n \kappa_{n\mathit{II}}^m R_b^{2n+1} + [\mu_r n + \mu_m(n+1)]\xi_{n\mathit{II}}^m + C_{nm} R_b^{n+2} = 0. \tag{2.36}$$

Substituting $\xi_{n\mathit{II}}^m$ in Eqn. (2.32) into Eqn. (2.36) gives

$$\kappa_{n\mathit{II}}^m = -\frac{[\mu_r n + \mu_m(n+1)]\xi_{nI}^m + C_{nm} R_b^{n+2}}{(\mu_r - \mu_m) n R_b^{2n+1} - [\mu_r n + \mu_m(n+1)] R_r^{2n+1}}. \tag{2.37}$$

From Eqns. (2.32) and (2.37), the following result is obtained

$$\xi_{n\mathit{II}}^m = \xi_{nI}^m + \frac{R_r^{2n+1}\{[\mu_r n + \mu_m(n+1)]\xi_{nI}^m + C_{nm} R_b^{n+2}\}}{(\mu_r - \mu_m) n R_b^{2n+1} - [\mu_r n + \mu_m(n+1)] R_r^{2n+1}}. \tag{2.38}$$

Substituting Eqns. (2.37) and (2.38) into Eqn. (2.31) yields

$$\xi_{nI}^m = C_{nm} d_n, \tag{2.39}$$

where

$$d_n = -d_n^{\top}/d_n^{\perp}, \tag{2.40}$$

and

$$\begin{aligned} d_n^{\top} &= R_r^{n+2} + \frac{\mu_m(2n+1) R_b^{n+2} R_r^{2n+1}}{(\mu_r - \mu_m) n R_b^{2n+1} - [\mu_r n + \mu_m(n+1)] R_r^{2n+1}}, \\ d_n^{\perp} &= (\mu_m - 1)(n+1) \\ &\quad + \frac{\mu_m(2n+1)[\mu_r n + \mu_m(n+1)] R_r^{2n+1}}{(\mu_r - \mu_m) n R_b^{2n+1} - [\mu_r n + \mu_m(n+1)] R_r^{2n+1}}. \end{aligned}$$

Particularly, for $n=4$ and $m=\pm 4$, the coefficients of ξ_{4I}^{4} and ξ_{4I}^{-4} can be expressed with $C_{4,4}$ and $C_{4,-4}$ in Eqn. (2.25) as

$$\begin{aligned}\xi_{4I}^{4} &= C_{4,4}d_4 = M_0\frac{d_4}{\sqrt{\pi}}(a+bi)c,\\ \xi_{4I}^{-4} &= C_{4,-4}d_4 = M_0\frac{d_4}{\sqrt{\pi}}(a-bi)c,\end{aligned} \tag{2.41}$$

where

$$d_4 = -d_4^{\top}/d_4^{\perp}, \tag{2.42}$$

and

$$\begin{aligned}d_4^{\top} &= R_r^6 + \frac{9\mu_m R_b^6 R_r^9}{4(\mu_r-\mu_m)R_b^9 - (4\mu_r+5\mu_m)R_r^9},\\ d_4^{\perp} &= 5(\mu_m-1) + \frac{9\mu_m(4\mu_r+5\mu_m)R_r^9}{4(\mu_r-\mu_m)R_b^9 - (4\mu_r+5\mu_m)R_r^9},\end{aligned}$$

2.6 Solutions of Scalar Potential and Flux Density

The derivation of the flux density is performed in the space outside of the rotor (Region I), because only the magnetic field in this region is used to compute the motor torque according to Lorentz force law. Substituting the coefficients of ξ_{4I}^{4} and ξ_{4I}^{-4} in Eqn. (2.41) into Eqn. (2.13) and discarding the higher order harmonic terms result in

$$\begin{aligned}\Phi_I &= \xi_{4I}^{-4}r^{-5}[Y_4^{-4}(\theta,\phi)] + \xi_{4I}^{4}r^{-5}[Y_4^{4}(\theta,\phi)]\\ &= M_0\frac{d_4}{\sqrt{\pi}}(a-bi)cr^{-5}\left(\frac{3}{16}\sqrt{\frac{35}{2\pi}}\sin^4\theta e^{-4i\phi}\right) + M_0\frac{d_4}{\sqrt{\pi}}(a+bi)cr^{-5}\\ &\quad\left(\frac{3}{16}\sqrt{\frac{35}{2\pi}}\sin^4\theta e^{4i\phi}\right)\\ &= M_0\frac{3cd_4}{8\pi}\sqrt{\frac{35}{2}}r^{-5}\sin^4\theta(a\cos 4\phi - b\sin 4\phi).\end{aligned} \tag{2.43}$$

Using Eqns. (2.1) and (2.6), the flux density in Region I (air) can be obtained

$$B_{Ir} = -\mu_0 \frac{\partial \Phi_I}{\partial r} = \frac{15\mu_0 M_0 c d_4}{8\pi} \sqrt{\frac{35}{2}} r^{-6} \sin^4\theta (a\cos 4\phi - b\sin 4\phi), \tag{2.44}$$

$$B_{I\theta} = -\mu_0 \frac{1}{r} \frac{\partial \Phi}{\partial \theta} = \frac{12\mu_0 M_0 c d_4}{8\pi} \sqrt{\frac{35}{2}} r^{-6} \sin^3\theta \cos\theta (b\sin 4\phi - a\cos 4\phi), \tag{2.45}$$

$$B_{I\phi} = -\mu_0 \frac{1}{r\sin\theta} \frac{\partial \Phi}{\partial \phi} = \frac{12\mu_0 M_0 c d_4}{8\pi} \sqrt{\frac{35}{2}} r^{-6} \sin^3\theta (a\sin 4\phi + b\cos 4\phi). \tag{2.46}$$

2.7 Simplification of Magnetic Field Model

It is worth mentioning that in the derivation of the magnetic field model, a generic Cartesian coordinates system is set up as indicated in Fig. 2.4 (or Fig. 2.6(a)), with angle α_0 specifying the position of PM poles. By letting $\alpha_0 = 0$ as shown in Fig. 2.6(b), the magnetic field model can be simplified. In this case, the x- and y-axes pass through the center of PM poles. Correspondingly, Eqns. (2.14) - (2.16) could be simplified as

$$M_{0r} = (-1)^{p-1} M_0 \cos[\phi - \frac{\pi}{4}(p-1)] \sin\theta, \tag{2.47}$$

$$M_{0\theta} = (-1)^{p-1} M_0 \cos[\phi - \frac{\pi}{4}(p-1)] \cos\theta, \tag{2.48}$$

$$M_{0\phi} = (-1)^{p} \ M_0 \sin[\phi - \frac{\pi}{4}(p-1)], \tag{2.49}$$

which are only valid within the range of

$$\frac{\pi}{4}(p-1) - \frac{\alpha}{2} < \phi < \frac{\pi}{4}(p-1) + \frac{\alpha}{2}, \tag{2.50}$$

$$\frac{\pi}{2} - \frac{\beta}{2} < \theta < \frac{\pi}{2} + \frac{\beta}{2}, \tag{2.51}$$

in the PM pole (Region II). Applying these equations into Eqn. (2.20), it can be verified that the constant b is always equal to zero. Hence, all terms related to b in Eqns. (2.44) - (2.46) vanish. Eqns. (2.44) - (2.46) become

$$B_{Ir} = \frac{15\mu_0 M_0 a c d_4}{8\pi} \sqrt{\frac{35}{2}} r^{-6} \sin^4\theta \cos 4\phi, \tag{2.52}$$

$$B_{I\theta} = -\frac{12\mu_0 M_0 a c d_4}{8\pi} \sqrt{\frac{35}{2}} r^{-6} \sin^3\theta \cos\theta \cos 4\phi, \tag{2.53}$$

$$B_{I\phi} = \frac{12\mu_0 M_0 a c d_4}{8\pi} \sqrt{\frac{35}{2}} r^{-6} \sin^3\theta \sin 4\phi. \tag{2.54}$$

This simplification can facilitate the torque formulation greatly.

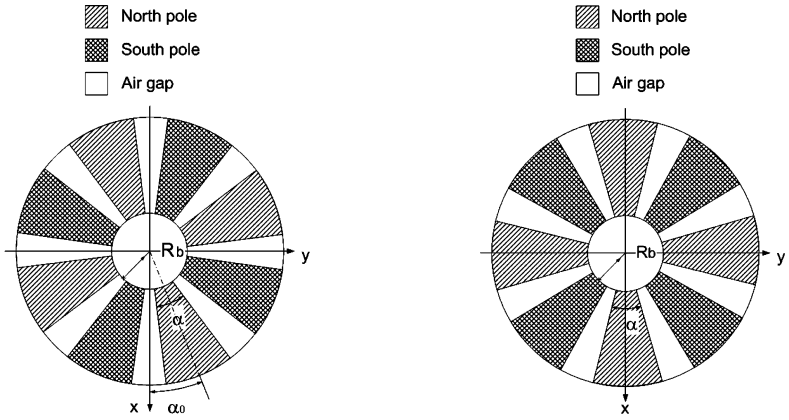

(a) General coordinates (PM pole center specified by α_0)

(b) x-axis through the center of PM pole ($\alpha_0 = 0$)

Fig. 2.6: Coordinates definition in rotor frame

2.8 Summary

This chapter has presented the magnetic field modeling of the PM-pole rotor. According to the magnetic characteristics of the three regions of the rotor space, Laplace's equations of magnetic scalar potential are derived. By using the boundary conditions in between neighboring regions as well as the spherical harmonic expansion of radial component of the residual magnetization vector, coefficients in the general solution of magnetic scalar potential are determined. The magnetic field flux density of the PM rotor is formulated analytically by taking the gradient of the scalar potential. This analytical magnetic field model is described based on the dimensional parameters of the PM poles. Hence, it can be used in the design of the spherical actuator to maximize the torque output.

References

1. Prieto R, Stuchly J A, Cobos J A, Uceda J et al (1999) 1D magnetic component model for planar structures. Proceedings of IEEE International Conference on Power Electronics, vol. 1, no. 27:574–579, Atlanta, USA, June 1999.
2. Zhu Z Q, Howe D, Chan C C et al (2002) Improved analytical model for predicting the magnetic field distribution in brushless permanent-magnet machines. IEEE Transactions on Magnetics, vol. 38, no. 1:229–238, January 2002.
3. Zhu Z Q, Howe D, Bolte E, Ackermann B et al (1993) Instantaneous magnetic field distribution in brushless permanent magnet DC motors, Part I: open-circuit field. IEEE Transactions on Magnetics, vol. 29, no. 1:124–135, January 1993.
4. Cho H S, Im C H, Jung H K et al (2001) Magnetic field analysis of 2-D permanent magnet array for planar motor. IEEE Transactions on Magnetics, vol. 37, no. 5:3762–3766, September 2001.

5. Polinder H, Hoeijmakers M J et al (1997) Analytic calculation of the magnetic field in PM machines. Proceedings of IEEE Industry Applications Society's Annual Meeting, 35–41, New Orleans, Louisiana, USA, 5–9 June 1997.
6. Xiong G, Nasar S A et al (2001) Analysis of fields and forces in a permanent magnet linear synchronous machine based on the concept of magnetic charge. IEEE Transactions on Magnetics, vol. 25, no. 3:2713–2719, May 1989.
7. Davey K, Vachtsevanos G, Powers R et al (1987) The analysis of fields and torques in spherical induction motors. IEEE Transactions on Magnetics, vol. 9, no. 1:273–282, January 1987.
8. Wang J, Jewell G W, Howe D et al (1997) A novel spherical actuator: design and control. IEEE Transactions on Magnetics, vol. 33, no. 5:4209–4211, September 1997.
9. Wang J, Wang W, Jewell G W, Howe D et al (1998) A novel spherical actuator with three degrees-of-freedom. IEEE Transactions on Magnetics, vol. 34, no. 4:2078–2080, July 1998.
10. Prieto R, Cobos J A, Garcia O, Alou P, Uceda J et al (2003) Study of 3-D magnetic components by means of double 2-D methodology. IEEE Transactions on Industrial Electronics, vol. 50, no. 1:183–192, February 2003.
11. Gieras J F, Wing M et al (1998) Permanent Magnet Motor Technology. Marcel Dekker, Inc., New York, 1998.
12. Miner G F (1996) Lines and Electromagnetic Fields for Engineers. Oxford University Press, USA, 1996.
13. Demarest K R (1998) Engineering Electromagnetics. Prentice Hall, Inc., USA, 1998.
14. Solymar L (1976) Electromagnetic Theory. Oxford University Press, UK, 1976.
15. Walter H (1971) Introduction to the Principles of Electromagnetism. Addison-Wesley Publishing Company, Inc., USA, 1971.
16. Virchenko N, Fedotova I et al (2001) Generalized Associated Legendre Functions and Their Applications. World Scientific Publication, USA, 2001.
17. Sadiku N O M (2001) Elements of Electromagnetics. Oxford University Press, UK, 2001.

Chapter 3
Torque Modeling

3.1 Introduction

As an important topic in electromagnetic actuators, the torque modeling of the actuator is to establish the relation between current input and torque output mathematically. One typical usage of the torque model is for computer simulation of actuator motions as shown in Fig. 3.1(a). Given a set of current inputs, torque output of an actuator can be calculated according to the torque model. Based on forward dynamics of an actuator, one is able to simulate how an actuator would move under the action of the torque. Another significant use of the torque model is for position and velocity servo control of actuators. According to inverse dynamics of an actuator as shown in Fig. 3.1(b), the desired actuator torque can be computed from the desired angular displacement (θ_d), angular velocity ($\dot{\theta}_d$) and angular acceleration ($\ddot{\theta}_d$) of the actuator. Then by utilizing the toque model, required currents can be calculated from the desired actuator torque. These currents are supplied to the actuator so that it can follow the desired motion. An analytical solution of the torque model in a

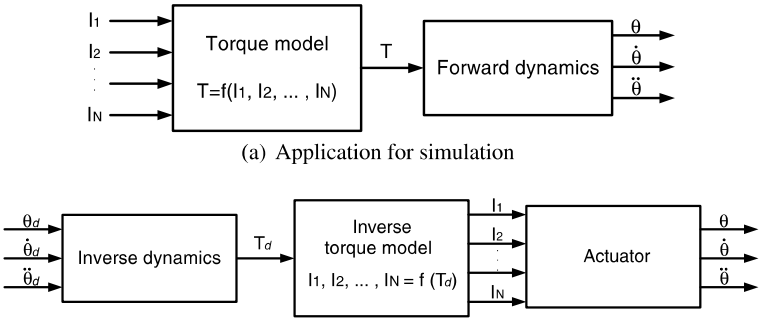

Fig. 3.1: Functions of the actuator torque model

L. Yan et al., *Design, Modeling and Experiments of 3-DOF Electromagnetic Spherical Actuators*, Mechanisms and Machine Science 4,
DOI 10.1007/978-94-007-1646-9_3, © Springer Science+Business Media B.V. 2011

linear fashion is preferred because it can facilitate the real-time motion control of the complex mechatronic systems.

Generally speaking, there are three types of methods that can be employed for the calculation of force and torque of electromagnetic products, i.e., Maxwell stress tensor (MST), coenergy method[1] and Lorentz force law. The MST approach computes local stress at all points of a boundary surface of a body, then sums the local stresses to obtain the global magnetic force/torque [1]. This classic method is usually used in finite element (FE) solution of force/torque computation. For example, Hamler *et al*. [2] took advantage of MST and an interpolation-based triangular mesh to compute the torque of a one-phase brushless motor. Im *et al*. [3] computed the force of a single-sided linear induction motor(SLIM)[2] by applying MST. Yamasawa [4] described the calculation of the magnetic thrust of an automotive magnetic actuator by expanding the MST to cover the nonlinear magnetic region. Davey *et al*. [5] proposed a general torque computation approach of spherical induction motors by using MST. The disadvantage of MST is that the result is very sensitive to discretization density and integration contour position. In addition, the definition of the boundary surface becomes difficult in 3D problems.

The coenergy method [6] can be employed to obtain the torque model of electromagnetic products analytically. Its basic principle is illustrated in Fig. 3.2. Many electromagnetic products possess coils and ferromagnetic materials such as soft iron disrupted by narrow airgaps. By energizing the coils, flux lines are generated and flow through the soft iron and airgaps, forming a closed magnetic flux loop. The relative permeability of soft iron (more than 4000) is much greater than that of the airgap (approximately 1). In other words, the reluctance of airgap is much larger than that of soft iron. Therefore, the magnetic energy is mostly stored in the narrow

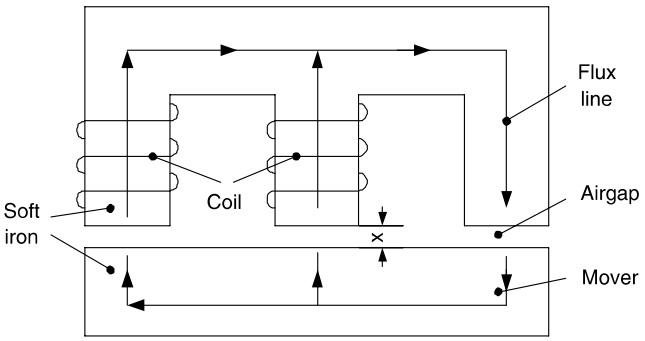

Fig. 3.2: Closed magnetic flux loop

[1] Coenergy method is also named virtual work method.

[2] A linear induction motor is conceptually a rotary induction motor whose stator core has been cut and unrolled. The circular stator becomes a linear stator, defining a single-sided linear induction motor (SLIM). Likewise, if the circular stator is cut into two sections and flattened, the motor becomes a double-sided linear induction motor (DLIM).

airgaps[3]. In this case, the magnetic energy can be formulated easily. Coenergy is equal to the difference of electrical power input and the magnetic energy stored. By differentiating the coenergy with respect to the displacement element x, the force acted on the mover can be calculated. If the displacement is from an angular element, then a torque model can be obtained. This approach was utilized by Lee *et al*. [7, 8, 9] to derive the torque model of VRSM successfully. Sahoo [10] and Materu [11] *et al*. have also obtained an analytical torque model of switched reluctant motors (SRM) in terms of the stator phase current and rotor position by using coenergy principle. One prerequisite of the implementation of coenergy method for torque modeling is that the magnetic energy stored in the airgap of actuators can be formulated readily.

However, due to the existence of large airgap or air-core coils in some cases, the magnetic energy cannot be formulated analytically and the coenergy method becomes ineffective. Alternatively, Lorentz force law can be adopted because energy formation is no longer required. Lorentz force law is especially useful when the force/torque is generated by a current-carrying conductor laying in the magnetic field of PM. As illustrated in Fig. 3.3, Lorentz force law [12] states that the force $d\mathbf{F}$ exerted on differential length segment $d\mathbf{l}$ of current-carrying conductor by external magnetic field $\mathbf{B}$ is equal to the multiplication of the current I_w and the cross product of $d\mathbf{l}$ and $\mathbf{B}$, i.e. $d\mathbf{F} = I_w d\mathbf{l} \times \mathbf{B}$. By using Lorentz force law, Sathuvalli *et al*. [13] calculated the force on an electrically conducting sphere placed in an arbitrary sinusoidally varying 1D magnetic field analytically. Another implementation of this method was found in the torque formulation of spherical actuators developed by Wang *et al* [14, 15].

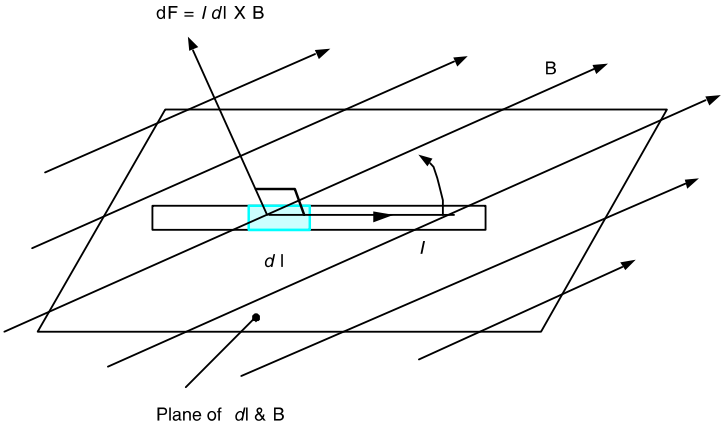

Fig. 3.3: Force on a current-carrying element

[3] A magnetic circuit is very similar to an electric circuit. The equivalent to resistance is reluctance; the equivalent to current is flux; the equivalent to voltage is mmf or magnetomotive force.

Due to the existence of the air-core coils and the large airgap between the rotor and the stator in our PM spherical actuator, the magnetic energy of the PM spherical actuator is difficult to formulate analytically. Based on previous research on the three torque modeling methods, Lorentz force law is adopted for the torque formulation of this PM spherical actuator. By utilizing the magnetic field model derived in Chapter 2, an analytical solution of the torque model is able to be obtained.

3.2 Formulation of Actuator Torque

3.2.1 Torque Generating Component of Flux Density

The direction of the force generated by each component of the flux density, B_{Ir}, $B_{I\theta}$ and $B_{I\phi}$ can be determined as shown in Fig. 3.4. The differential length segment $d\mathbf{l}$ of the wire is tangential to the spherical surface at point O. Note that only B_{Ir} produces a torque to change the rotor orientation. $B_{I\theta}$ and $B_{I\phi}$ do not produce torque on the rotor because the action lines of magnetic forces generated by $B_{I\phi}$ and $B_{I\theta}$ pass through the rotor center. As a consequence, following discussion will focus on the radial component of the flux density B_{Ir}.

3.2.2 Torque Model for a Single Coil

The torque produced by a single coil due to the existence of the PM rotor magnetic field will be first studied. An ideal air-core coil used in the spherical actuator is illustrated in Fig. 3.5. The coil assumes a conical-shaped object embedded in the stator shell to facilitate the formulation of the actuator torque. Without loss of generality, the dimensions of the coil (shaded region) can be specified by four quantities:

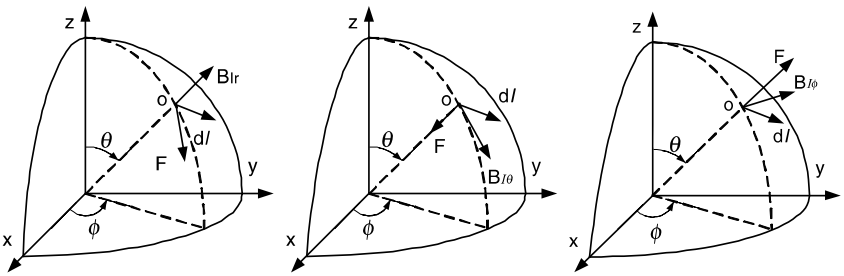

(a) r-direction (b) θ-direction (c) ϕ-direction

Fig. 3.4: Force activated by three components of the flux density

R_0-the center distance of the inner surface of the coil; R_1-the center distance of the outer surface of the coil; ζ_0-the angular diameter of the air-core and ζ_1-the angular diameter of the coil.

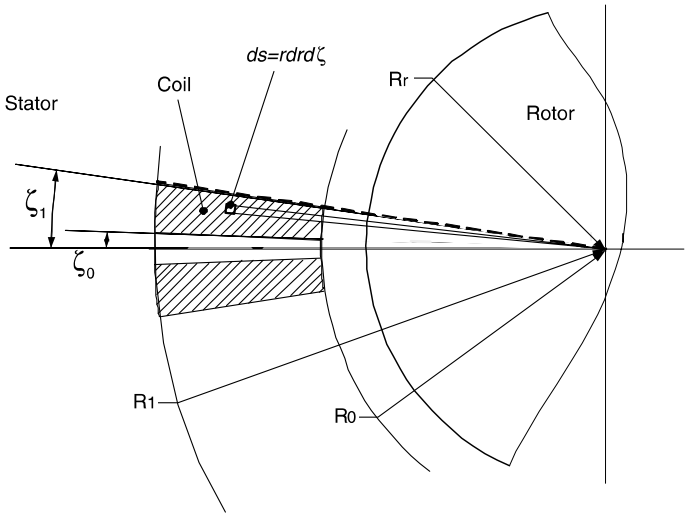

Fig. 3.5: Section view of the conical air-core coil

3.2.2.1 Force on Differential Line Segment of Winding

Consider a differential line segment $d\mathbf{l}$ of the winding. As shown in Fig. 3.5, the differential sectional area of $d\mathbf{l}$ can be computed by

$$ds = rdrd\zeta. \tag{3.1}$$

The current passing through this section area is $Jrdrd\zeta$, where J is the current density in the section area of the coil. According to Lorentz force law, the differential force on the rotor caused by the interaction between the magnetic field of the PM-pole rotor and current-carrying conductor $d\mathbf{l}$ is

$$d\mathbf{F} = -Id\mathbf{l} \times B_{Ir}(r,\theta,\phi)\mathbf{e}_r = -Jrdrd\zeta d\mathbf{l} \times B_{Ir}(r,\theta,\phi)\mathbf{e}_r, \tag{3.2}$$

where $\mathbf{e}_r$ is the unit vector in the r-direction of spherical coordinates. The negative sign indicates that the force imposed on the rotor by $d\mathbf{l}$ is the reaction force exerted by the magnetic field on $d\mathbf{l}$.

3.2.2.2 Torque on Differential Line Segment of Winding

It can be seen that the differential torque generated by $d\mathbf{l}$ is the cross product of the moment arm $r\mathbf{e}_r$ (the vector from rotor center to the differential winding segment) and force $d\mathbf{F}$, i.e.,

$$d\mathbf{T}_i = r\mathbf{e}_r \times [-Jrdrd\zeta d\mathbf{l} \times B_{Ir}(r,\theta,\phi)\mathbf{e}_r]. \tag{3.3}$$

3.2.2.3 Integration on Entire Coil Volume

Integrating the differential torque in Eqn. (3.3) within the entire volume of the coil gives the torque of a single coil under the magnetic field of PM rotor as

$$\begin{aligned}\mathbf{T}_c &= \int\int\int_V r\mathbf{e}_r \times [-Jrdrd\zeta d\mathbf{l} \times B_{Ir}(r,\theta,\phi)\mathbf{e}_r] \\ &= J\int_{R_0}^{R_1}\int_{\zeta_0}^{\zeta_1}\left\{\int_C r\mathbf{e}_r \times [B_{Ir}(r,\theta,\phi)\mathbf{e}_r \times d\mathbf{l}]\right\} rdrd\zeta.\end{aligned} \tag{3.4}$$

The symbol $\int_C$ denotes the line integral of the differential torque along a circular loop of the winding that has a "wire" section area of ds. The total volume of the coil can be completely described by the four parameters R_0, R_1, ζ_0 and ζ_1. Integration of the torque value is carried out within this volume. Because the differential length $d\mathbf{l}$ is tangential to the spherical surface, $d\mathbf{l}$ is perpendicular to $\mathbf{e}_r$. Therefore, the relationship of $\mathbf{e}_r \times (\mathbf{e}_r \times d\mathbf{l}) = -d\mathbf{l}$ can be obtained readily. As a result, Eqn. (3.4) is reduced to

$$\mathbf{T}_c = -J\int_{R_0}^{R_1}\int_{\zeta_0}^{\zeta_1}\left\{\int_C rB_{Ir}(r,\theta,\phi)d\mathbf{l}\right\} rdrd\zeta. \tag{3.5}$$

3.2.2.4 Solution to Torque Integral

With analytical expression of B_{Ir} and Eqn. (3.5), the actuator torque generated by the i^{th} coil, denoted as $\mathbf{T}_i$, can be expressed explicitly using the i^{th} coil-axis position θ_i and ϕ_i with respect to the rotor frame, as well as the current input J_i passing through this coil. For any specific rotor orientation, the torque output can then be determined by the current input uniquely.

Assume that only one coil is mounted on the stator. The spherical coordinates (θ_i, ϕ_i) is used to represent the position of the coil in the rotor frame. One loop of winding in the i^{th} coil on the sphere is indicated in Fig. 3.6; $\mathbf{e}_{\theta i}$ and $\mathbf{e}_{\phi i}$ are unit vectors of the spherical coordinates. The magnitude and the unit vector of the differential length segment $d\mathbf{l}$ can be calculated respectively as

$$\|d\mathbf{l}\| = r\sin\zeta\, d\psi, \tag{3.6}$$

$$\mathbf{e}_{d\mathbf{l}} = \sin\psi\mathbf{e}_{\theta i} - \cos\psi\mathbf{e}_{\phi i}. \tag{3.7}$$

Combining Eqns. (3.6) and (3.7) together, we have

$$d\mathbf{l} = r\sin\zeta\, d\psi(\sin\psi\mathbf{e}_{\theta i} - \cos\psi\mathbf{e}_{\phi i}). \tag{3.8}$$

Substituting magnetic field component B_{Ir} of Eqn. (2.52) and $d\mathbf{l}$ of Eqn. (3.8) into torque integral formula of Eqn. (3.5) results in

$$\mathbf{T}_i = \sqrt{\frac{35}{2}}\frac{15\mu_0 M_0 acd_4}{8\pi} J_i \int_{R_0}^{R_1}\int_{\zeta_0}^{\zeta_1}\int_0^{2\pi} r^{-3}\sin^4\theta\cos 4\phi\sin\zeta$$
$$(\cos\psi\mathbf{e}_{\phi i} - \sin\psi\mathbf{e}_{\theta i})d\psi dr d\zeta. \tag{3.9}$$

For a particular coil, the ranges of integration are known: ζ varies from ζ_0 to ζ_1; r from R_0 to R_1; ψ from 0 to 2π. To integrate Eqn. (3.9), it is necessary to relate the terms $\sin\theta$ and $\cos 4\phi$ to ζ, ψ and r. For convenience, denote the angular portion of Eqn. (3.9) as

$$\mathbf{D}(\theta,\phi) \equiv \sin^4\theta\cos 4\phi\sin\zeta(\cos\psi\mathbf{e}_{\phi i} - \sin\psi\mathbf{e}_{\theta i}). \tag{3.10}$$

Eqn. (3.9) can thus be compactly expressed as

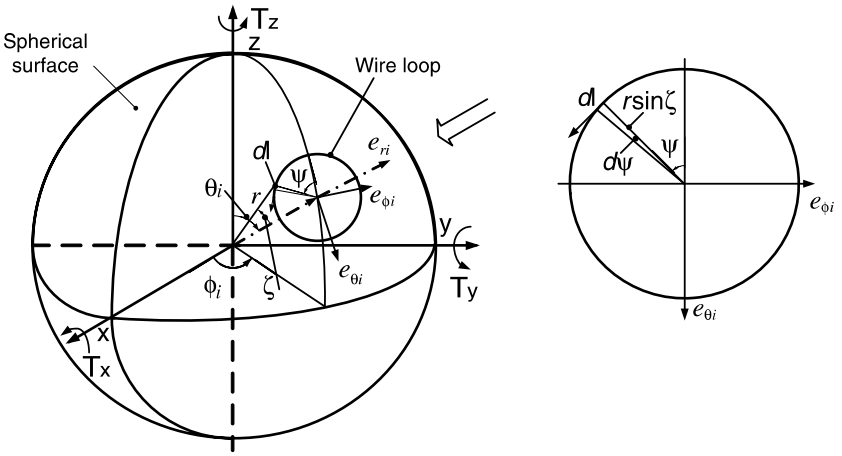

Fig. 3.6: One loop of wire in the i^{th} coil on the sphere

$$\mathbf{T}_i = \sqrt{\frac{35}{2}}\frac{15\mu_0 M_0 acd_4}{8\pi} J_i \int_{R_0}^{R_1}\int_{\zeta_0}^{\zeta_1}\int_0^{2\pi} r^{-3}[\mathbf{D}(\theta,\phi)]d\psi dr d\zeta$$
$$= \sqrt{\frac{35}{2}}\frac{15\mu_0 M_0 acd_4 R_c}{16\pi} J_i \int_{\zeta_0}^{\zeta_1}\int_0^{2\pi} [\mathbf{D}(\theta,\phi)]d\psi d\zeta, \tag{3.11}$$

where

$$R_c = R_0^{-2} - R_1^{-2}. \tag{3.12}$$

The integration of $\int_{\zeta_0}^{\zeta_1}\int_0^{2\pi}[\mathbf{D}(\theta,\phi)]d\psi d\zeta$ will be discussed below. First, rewrite $\mathbf{D}(\theta,\phi)$ as

$$\mathbf{D}(\theta,\phi) = \sin^4\theta(\cos^4\phi - 6\sin^2\phi\cos^2\phi + \sin^4\phi)\sin\zeta(\cos\psi\mathbf{e}_{\phi i} - \sin\psi\mathbf{e}_{\theta i}). \tag{3.13}$$

Recall the relationship of the Cartesian coordinates, x, y, z, to spherical coordinates θ and ϕ,

$$\cos\phi = \frac{x}{r\sin\theta}, \quad \sin\phi = \frac{y}{r\sin\theta}. \tag{3.14}$$

Substituting Eqn. (3.14) into Eqn. (3.13) gives

$$\mathbf{D}(\theta,\phi) = \frac{1}{r^4}(x^4 - 6x^2y^2 + y^4)\sin\zeta(\cos\psi\mathbf{e}_{\phi i} - \sin\psi\mathbf{e}_{\theta i}). \tag{3.15}$$

With reference to Fig. 3.6, it can be verified that the Cartesian coordinates of the differential element on the coil, x, y and z can be represented in terms of ζ, ψ, θ_i and ϕ_i as following

$$\begin{aligned} x &= r\cos\zeta\sin\theta_i\cos\phi_i - r\sin\zeta\cos\psi\cos\theta_i\cos\phi_i + r\sin\zeta\sin\psi\sin\phi_i, \\ y &= r\cos\zeta\sin\theta_i\sin\phi_i - r\sin\zeta\cos\psi\cos\theta_i\sin\phi_i - r\sin\zeta\sin\psi\cos\phi_i, \\ z &= r\cos\zeta\cos\theta_i + r\sin\zeta\cos\psi\sin\theta_i. \end{aligned} \tag{3.16}$$

The unit vectors $\mathbf{e}_{\phi i}$ and $\mathbf{e}_{\theta i}$ in spherical coordinates can be represented in terms of Cartesian coordinates as

$$\mathbf{e}_{\phi i} = -\sin\phi_i\mathbf{e}_x + \cos\phi_i\mathbf{e}_y = \begin{bmatrix} -\sin\phi_i \\ \cos\phi_i \\ 0 \end{bmatrix}, \tag{3.17}$$

$$\mathbf{e}_{\theta i} = \cos\theta_i\cos\phi_i\mathbf{e}_x + \cos\theta_i\sin\phi_i\mathbf{e}_y - \sin\theta_i\mathbf{e}_z = \begin{bmatrix} \cos\theta_i\cos\phi_i \\ \cos\theta_i\sin\phi_i \\ -\sin\theta_i \end{bmatrix}. \tag{3.18}$$

By substituting Eqns. (3.16), (3.17) and (3.18) into Eqn. (3.15), $\mathbf{D}(\theta,\phi)$ can be expressed as a function of ζ and ψ. Because the integration range of ψ is from 0 to

2π, many terms in $\int_{\zeta_0}^{\zeta_1}\int_0^{2\pi}[\mathbf{D}(\theta,\phi)]d\psi d\zeta$ vanish. Let

$$\mathbf{D}^e(\theta_i,\phi_i) \equiv \int_{\zeta_0}^{\zeta_1}\int_0^{2\pi}[\mathbf{D}(\theta,\phi)]d\psi d\zeta, \tag{3.19}$$

we have

$$\begin{aligned}\mathbf{D}^e(\theta_i,\phi_i)=\pi\Big\{\mathbf{e}_{\phi i}\ [\ G'_\zeta\ (\ &-3\sin\theta_i\cos^4\phi_i\cos^3\theta_i-18\sin\theta_i\cos^2\phi_i\cos\theta_i\sin^2\phi_i\\ &-3\sin\theta_i\sin^4\phi_i\cos^3\theta_i+18\sin\theta_i\cos^2\phi_i\cos^3\theta_i\sin^2\phi_i+3\sin\theta_i\cos^4\phi_i\\ &\cos\theta_i+3\sin^4\phi_i\sin\theta_i\cos\theta_i)+G''_\zeta(-4\sin^3\theta_i\cos^4\phi_i\cos\theta_i-4\sin^3\theta_i\\ &\sin^4\phi_i\cos\theta_i+24\sin^3\theta_i\cos^2\phi_i\sin^2\phi_i\cos\theta_i)]-\mathbf{e}_{\theta i}[G'_\zeta(12\sin\theta_i\cos^3\phi_i\\ &\cos^2\theta_i\sin\phi_i+12\sin\theta_i\cos\phi_i\sin^3\phi_i-12\sin\theta_i\sin^3\phi_i\cos^2\theta_i\cos\phi_i-12\sin\theta_i\\ &\sin\phi_i\cos^3\phi_i)+G''_\zeta(16\sin^3\theta_i\cos^3\phi_i\sin\phi_i-16\sin^3\theta_i\sin^3\phi_i\cos\phi_i)]\Big\},\end{aligned} \tag{3.20}$$

Eqn. (3.20) is simplified as following

$$\begin{aligned}\mathbf{D}^e(\theta_i,\phi_i)=(G''_\zeta-\frac{3G'_\zeta}{4})\ \pi\ \Big\{&\mathbf{e}_{\phi i}(-4\sin^3\theta_i\cos^4\phi_i\cos\theta_i-4\sin^3\theta_i\sin^4\phi_i\cos\theta_i\\ &+24\sin^3\theta_i\cos^2\phi_i\sin^2\phi_i\cos\theta_i)-\mathbf{e}_{\theta i}(16\sin^3\theta_i\cos^3\phi_i\sin\phi_i-16\sin^3\theta_i\\ &\sin^3\phi_i\cos\phi_i)\Big\},\end{aligned} \tag{3.21}$$

where

$$G'_\zeta = 1/5\sin^5\zeta_1-1/5\sin^5\zeta_0, \tag{3.22}$$

$$\begin{aligned}G''_\zeta = {}&1/5\cos^4\zeta_0\sin\zeta_0-1/15\cos^2\zeta_0\sin\zeta_0-2/15\sin\zeta_0-1/5\cos^4\zeta_1\sin\zeta_1\\ &+1/15\cos^2\zeta_1\sin\zeta_1+2/15\sin\zeta_1.\end{aligned} \tag{3.23}$$

Eqn. (3.21) can be rewritten in a compact form as

$$\mathbf{D}^e(\theta_i,\phi_i) = \pi G_\zeta[\mathbf{D}^e_c(\theta_i,\phi_i)], \tag{3.24}$$

where

$$G_\zeta = G''_\zeta-\frac{3G'_\zeta}{4}, \tag{3.25}$$

which is completely determined by the geometry of coils, and

$$\begin{aligned}\mathbf{D}^e_c(\theta_i,\phi_i)=&\mathbf{e}_{\phi i}(-4\sin^3\theta_i\cos^4\phi_i\cos\theta_i-4\sin^3\theta_i\sin^4\phi_i\cos\theta_i+24\sin^3\theta_i\cos^2\phi_i\\ &\sin^2\phi_i\cos\theta_i)-\mathbf{e}_{\theta i}(16\sin^3\theta_i\cos^3\phi_i\sin\phi_i-16\sin^3\theta_i\sin^3\phi_i\cos\phi_i),\end{aligned} \tag{3.26}$$

which is specified by the coil arrangement patterns. Consequently, the integration of Eqn. (3.11) can be obtained as

$$\mathbf{T}_i = \frac{15}{16}\sqrt{\frac{35}{2}}\mu_0 M_0 acd_4 R_c G_\zeta [\mathbf{D}_c^e(\theta_i, \phi_i)] J_i. \tag{3.27}$$

Note that $\mathbf{D}_c^e(\theta_i, \phi_i)$ is a 3×1 Cartesian vector. Parameters θ_i and ϕ_i represent the position of the i^{th} coil's axis relative to the rotor frame. Without loss of generality, let

$$\mathbf{G}(\theta_i, \phi_i) = [g_x(\theta_i, \phi_i)\ g_y(\theta_i, \phi_i)\ g_z(\theta_i, \phi_i)]^T \equiv \mathbf{D}_c^e(\theta_i, \phi_i). \tag{3.28}$$

Eqn. (3.27) can be written in the matrix form

$$\mathbf{T}_i = T_c \mathbf{G}(\theta_i, \phi_i) J_i \tag{3.29}$$

$$\text{or} \quad \begin{bmatrix} T_{xi} \\ T_{yi} \\ T_{zi} \end{bmatrix} = T_c \begin{bmatrix} g_x(\theta_i, \phi_i) \\ g_y(\theta_i, \phi_i) \\ g_z(\theta_i, \phi_i) \end{bmatrix} J_i, \tag{3.30}$$

where

$$T_c = \frac{15}{16}\sqrt{\frac{35}{2}}\mu_0 M_0 acd_4 R_c G_\zeta. \tag{3.31}$$

3.2.3 Torque Model for Complete Set of Coils

For the i^{th} coil, the torque model of the actuator can be expressed as Eqn. (3.29). Hence, there will be N torque equations like Eqn. (3.30) with N coils mounted on the stator. The actuator torque is thus a vector sum of all the individual torque equations. Concatenating all N torque equations, we can obtain the torque model of the actuator in the rotor frame as

$$\mathbf{T} = T_c \begin{bmatrix} g_x(\theta_1, \phi_1)\ g_x(\theta_2, \phi_2)\ \cdots\ g_x(\theta_N, \phi_N) \\ g_y(\theta_1, \phi_1)\ g_y(\theta_2, \phi_2)\ \cdots\ g_y(\theta_N, \phi_N) \\ g_z(\theta_1, \phi_1)\ g_z(\theta_2, \phi_2)\ \cdots\ g_z(\theta_N, \phi_N) \end{bmatrix} \begin{bmatrix} J_1 \\ J_2 \\ \vdots \\ J_N \end{bmatrix}. \tag{3.32}$$

or

$$\mathbf{T} = T_c \boldsymbol{Q} \mathbf{J}, \tag{3.33}$$

where

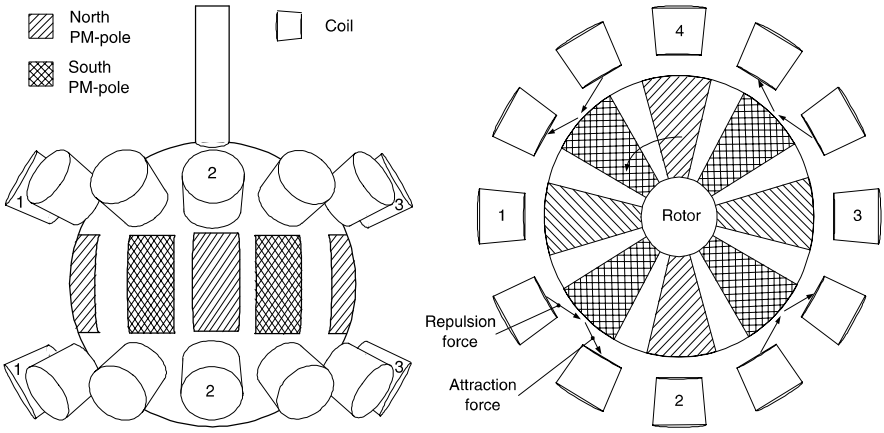

(a) Two layers of coils (front view) (b) Twelve coils for one layer (top view)

Fig. 3.7: Two layers of twelve coils distributed around the PM-pole rotor

$$\boldsymbol{Q} = \begin{bmatrix} g_x(\theta_1,\phi_1)\ g_x(\theta_2,\phi_2)\ \cdots\ g_x(\theta_N,\phi_N) \\ g_y(\theta_1,\phi_1)\ g_y(\theta_2,\phi_2)\ \cdots\ g_y(\theta_N,\phi_N) \\ g_z(\theta_1,\phi_1)\ g_z(\theta_2,\phi_2)\ \cdots\ g_z(\theta_N,\phi_N) \end{bmatrix} \text{ is the torque matrix; } \theta_i \text{ and } \phi_i \text{ present the position of the } i^{th} \text{ coil in the rotor frame;} \tag{3.34}$$

$$\mathbf{J} = \begin{bmatrix} J_1 \\ J_2 \\ \vdots \\ J_N \end{bmatrix} \text{ is the current density vector of electric currents passing through Coil 1, Coil 2, } \cdots \text{, and Coil } N. \tag{3.35}$$

The torque model of Eqn. (3.33) can be generically applicable to the study of spherical actuators with any number of coils. In this research, two layers of twelve coils are employed on the actuator as illustrated in Fig. 3.7. Pairs of coils at positions 1, 2, 3 and 4 are for tilting motion of the rotor in two different directions. Through the attraction and repulsion force generated by rest of the coils (Fig. 3.7(b)), a spinning motion about the rotor axis can be achieved. The following discussion is based on this coil layout.

3.2.4 Orientation Dependance of Torque Model

Further inspection of Eqn. (3.32) shows that the positions of the coils (θ_i, ϕ_i) are defined based on the rotor frame. Because coils are fixed on the stator, when the

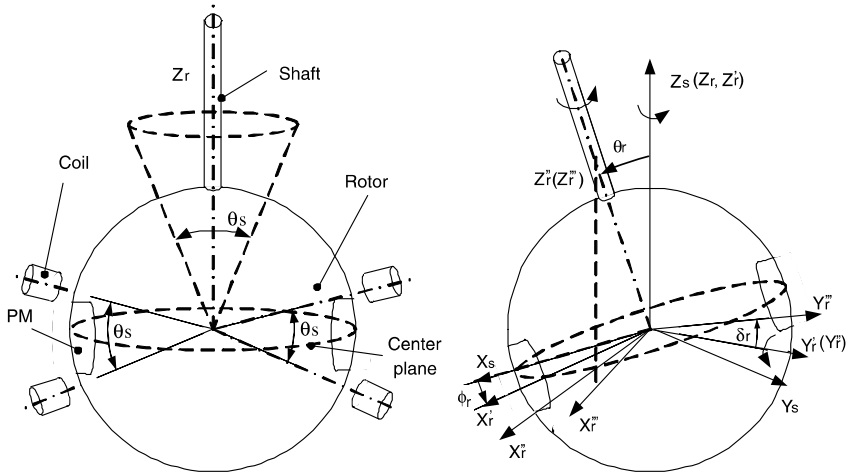

(a) Working range of the rotor axis (b) Rotation of the rotor frame

Fig. 3.8: Representation of the rotor orientation

rotor moves and change its orientation, (θ_i, ϕ_i) will change its value and thus the matrix $\boldsymbol{Q}$ and the torque value. This section shows how to obtain the torque matrix from the rotor orientation.

3.2.4.1 Representation of the Rotor Orientation

The workspace of the PM spherical actuator is shown in Fig. 3.8(a). A series of PM poles are mounted along the equator of the rotor, whereas the air-core coils are symmetrically mounted on the stator with respect to the stator equatorial plane, with two layers separated by an angular distance of θ_s. It can spin about its own z-axis, Z_r, in 360° without constraint. The rotor can also incline about its equatorial plane to an extreme position that the axes of a PM pole and the coil are aligned. Thus the z-axis of the rotor can move within a conical workspace with a conical angle of θ_s as shown in Fig. 3.8(a).

The orientation of the rotor frame with respect to the stator frame can be expressed by using Euler angles as follows. Let the rotor frame be (X_r, Y_r, Z_r) and the stator frame be (X_s, Y_s, Z_s). In order to arrive at an arbitrary final orientation within the workspace, three rotations of the rotor have to take place in sequence (Fig. 3.8(b)). Suppose that the stator frame is coincident with the rotor frame initially, the Euler ZYZ angle expression of the rotor orientation can be written as the matrix multiplication of the three body rotation matrices $\boldsymbol{R}_z(\phi_r)$, $\boldsymbol{R}_y(\theta_r)$ and $\boldsymbol{R}_z(\delta_r)$ as [16]

$$\begin{bmatrix} X_s \\ Y_s \\ Z_s \end{bmatrix} = \boldsymbol{R} \begin{bmatrix} X_r \\ Y_r \\ Z_r \end{bmatrix}, \tag{3.36}$$

where

$$\boldsymbol{R} = \boldsymbol{R}_z(\phi_r)\boldsymbol{R}_y(\theta_r)\boldsymbol{R}_z(\delta_r), \tag{3.37}$$

$$\boldsymbol{R}_z(\phi_r) = \begin{bmatrix} \cos\phi_r & -\sin\phi_r & 0 \\ \sin\phi_r & \cos\phi_r & 0 \\ 0 & 0 & 1 \end{bmatrix}, \tag{3.38}$$

$$\boldsymbol{R}_y(\theta_r) = \begin{bmatrix} \cos\theta_r & 0 & \sin\theta_r \\ 0 & 1 & 0 \\ -\sin\theta_r & 0 & \cos\theta_r \end{bmatrix}, \tag{3.39}$$

$$\boldsymbol{R}_z(\delta_r) = \begin{bmatrix} \cos\delta_r & -\sin\delta_r & 0 \\ \sin\delta_r & \cos\delta_r & 0 \\ 0 & 0 & 1 \end{bmatrix}. \tag{3.40}$$

3.2.4.2 Computation of Torque Matrix Q from Rotor Orientation

By utilizing Euler angle representation of the rotor orientation, the computing process of torque matrix $\boldsymbol{Q}$ from the rotor orientation is carried out as follows (Fig. 3.9).

Step one: *Computation of initial values of θ_i and ϕ_i*

Because the positions of all coil axes with respect to the rotor frame at the initial rotor orientation are known, it is easy to obtain the initial values of (θ_i, ϕ_i) of the i^{th} coil, i.e.,

$$\theta_{i,0} = \pi/2 - \theta_s/2, \qquad \phi_{i,0} = \pi(i-1)/6, \tag{3.41}$$

for coils ($i = 1, 2, ..., 12$) at the upper layer, and

$$\theta_{i,0} = \pi/2 + \theta_s/2, \qquad \phi_{i,0} = \pi(i-13)/6, \tag{3.42}$$

for coils ($i = 13, 14, ..., 24$) at the lower layer. The subscript "0" represents the initial values of θ_i, ϕ_i.

Step two: *Calculate the initial position of a unit vector on the coil axis*

Take a unit vector starting from the rotor center along the axis of the i^{th} coil. The Cartesian coordinates of the end point of this vector in the rotor frame can be calculated as

$$\mathbf{p}_{i,0} = \begin{bmatrix} \sin\theta_{i,0}\cos\phi_{i,0} \\ \sin\theta_{i,0}\sin\phi_{i,0} \\ \cos\theta_{i,0} \end{bmatrix}. \tag{3.43}$$

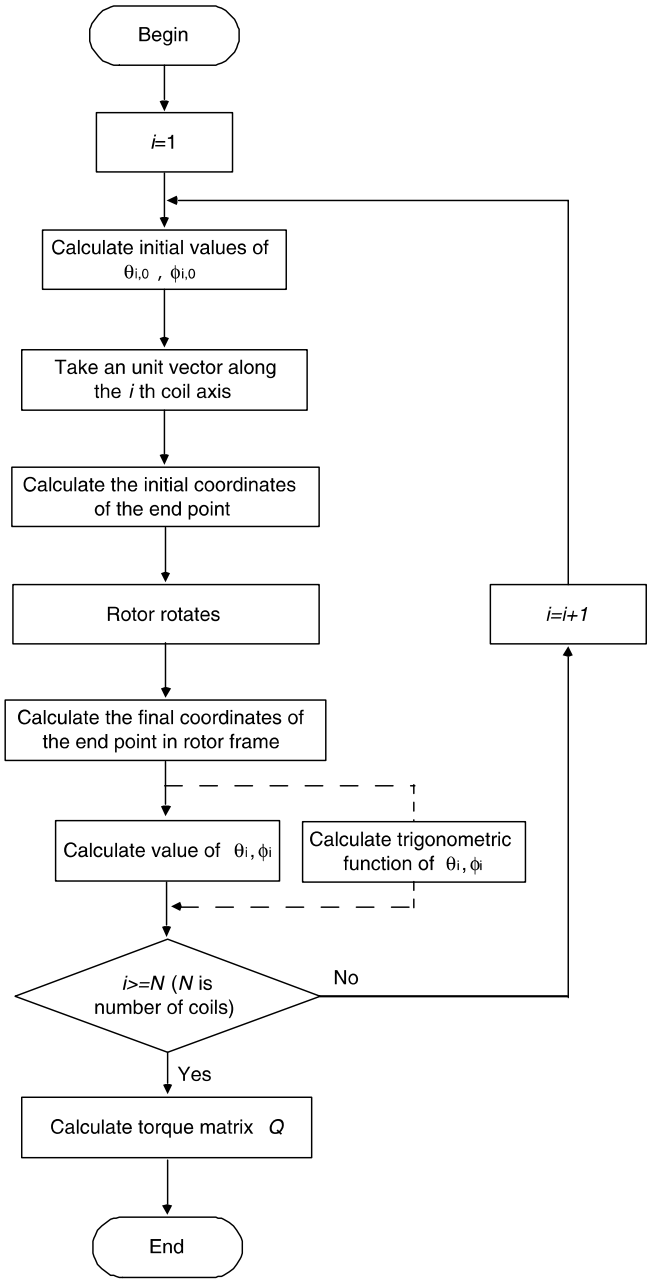

Fig. 3.9: Calculation of torque matrix from rotor orientation

Step three: *Compute the final position of the end point of the unit vector after rotor rotations*

The final coordinates $\mathbf{p}_i$ of the point $\mathbf{p}_{i,0}$ in the rotor frame can be obtained via

$$\mathbf{p}_i = \begin{bmatrix} p_{ix} \\ p_{iy} \\ p_{iz} \end{bmatrix} = [\boldsymbol{R}_z(\phi_r)\boldsymbol{R}_y(\theta_r)\boldsymbol{R}_z(\delta_r)]^T \mathbf{p}_{i,0},$$

where p_{ix}, p_{iy} and p_{iz} are components of $\mathbf{p}_i$.

Step four: *Computation of (θ_i, ϕ_i) or their trigonometric functions*

In order to obtain the torque matrix $\boldsymbol{Q}$, values of θ_i, ϕ_i or their trigonometric functions can be calculated from the final coordinates of $\mathbf{p}_i$.

(i) A simple way to obtain $\boldsymbol{Q}$ is to calculate θ_i and ϕ_i then substitute them into the torque matrix formula. This approach is easy to understand and can be employed to analyze or observe the torque variation corresponding to θ_i and ϕ_i. From the final position of the unit vector $\mathbf{p}_i$ in the rotor frame, the values of θ_i and ϕ_i can be obtained in terms of p_{ix}, p_{iy} and p_{iz} as follows.

$$\theta_i = \cos^{-1}\left(\frac{p_{iz}}{\sqrt{p_{ix}^2 + p_{iy}^2 + p_{iz}^2}}\right) = \cos^{-1}(p_{iz}), \tag{3.44}$$

$$\phi_i = \begin{cases} \cos^{-1}\left(\dfrac{p_{ix}}{\sqrt{p_{ix}^2 + p_{iy}^2}}\right), & p_{iy} \geq 0, \\ -\cos^{-1}\left(\dfrac{p_{ix}}{\sqrt{p_{ix}^2 + p_{iy}^2}}\right), & p_{iy} < 0. \end{cases} \tag{3.45}$$

Note that θ_i takes values within $(0, \pi)$. Due to the different signs of cosine function in $(0, \pi/2]$ and in $[\pi/2, \pi)$, the value of θ_i can be uniquely determined through Eqn. (3.44). In contrast, for the implementation of Eqn. (3.45), two situations for $p_{iy} \geq 0$ and $p_{iy} < 0$ are considered. It can be found that when $p_{ix}^2 + p_{iy}^2 = 0$, Eqn. (3.45) is no longer available. This condition implies that the axis of this coil is co-linear with the shaft of the rotor. However, in practice, this situation will never happen due to the constraints of the mechanical design in the actual spherical actuator.

(ii) The previous method facilitate the analysis and observation of actuator torque variation with respect to θ_i and ϕ_i. But it takes long computation time due to the trigonometric functions in the torque matrix, which may not be feasible for real-time motion control. Therefore, an alternative approach is used to calculate the torque matrix $\boldsymbol{Q}$ by computing trigonometric functions of θ_i and ϕ_i from $\mathbf{p}_i$.

Inspection of Eqn. (3.26) shows that $\mathbf{D}_c^e(\theta_i, \phi_i)$ or torque matrix $\boldsymbol{Q}$ is composed of $\sin\theta_i$, $\cos\theta_i$, $\sin\phi_i$ and $\cos\phi_i$. Solving functions of $\sin\theta_i$, $\cos\theta_i$, $\sin\phi_i$ and $\cos\phi_i$ from the final position $\mathbf{p}_i$ of the axis point directly instead of from θ_i and ϕ_i could improve the computing efficiency considerably because computation of trigono-

metric functions takes much time. Specifically, trigonometric functions of θ_i and ϕ_i are calculated as

$$\begin{aligned}
\cos\phi_i &= \frac{p_{ix}}{\sqrt{p_{ix}^2+p_{iy}^2}},\\
\sin\phi_i &= \frac{p_{iy}}{\sqrt{p_{ix}^2+p_{iy}^2}},\\
\cos\theta_i &= \frac{p_{iz}}{\sqrt{p_{ix}^2+p_{iy}^2+p_{iz}^2}} = p_{iz},\\
\sin\theta_i &= \sqrt{p_{ix}^2+p_{iy}^2}.
\end{aligned} \tag{3.46}$$

Step five: *Complete solution of torque matrix*

Repeat the above computation for the all coils. A complete set of θ_i and ϕ_i or their trigonometric functions can be calculated. Substituting all these values into Eqn. (3.32), the torque matrix $\boldsymbol{Q}$ can be obtained finally.

3.3 Solution of Inverse Electromagnetics

With matrix $\boldsymbol{Q}$, the inverse electromagnetics solution of the actuator can be solved. The purpose of the inverse electromagnetics solution is to determine the required current input from the desired torque output based on torque model. The discussion of inverse electromagnetics includes two parts. One is on the existence of inverse electromagnetics solution within the workspace, i.e., $\boldsymbol{Q}$ is a full rank matrix, the other is to obtain the minimum right-inverse solution of electromagnetics because $\boldsymbol{Q}$ is not a square matrix.

3.3.1 Nonsingularity of the Workspace

Singularities here are defined as orientations of the rotor where no torque can be generated with respect to the rotor center even though large currents are supplied. These singularities have to be strictly avoided in the design because they may cause severe malfunctions. In mathematical sense, the non-singular orientation of the spherical actuator are the orientations that there exists at least one set of coil currents $[J_1, J_2, ..., J_N]^T$ to produce the desired actuator torque $\mathbf{T}$. This implies that the matrix $\boldsymbol{Q}$ must be a full rank matrix for any rotor orientation within the workspace. A simple way to verify the nonsingularity of the spherical actuator is to compute the rank of torque matrix $\boldsymbol{Q}$ for every attainable rotor orientation within the workspace. If the

rank is equal to 3, i.e., full rank, the spherical actuator is singularity-free. Otherwise, singularities exist within the workspace. However, this method does not reveal how close the system is to singularity points. Therefore, a method based on the condition number of $\boldsymbol{Q}$ is proposed to satisfy this requirement.

The condition number for square matrices is computed from the characteristic roots or eigenvalues[4] of the matrix. It is defined as the ratio of largest eigenvalue and the smallest eigenvalue (in magnitude), i.e.,

$$cond(\boldsymbol{Q}) = \left| \frac{\text{largest eigenvalue}}{\text{smallest eigenvalue}} \right|.$$

It can be generalized to non-square matrices with singular values[5]

$$cond(\boldsymbol{Q}) = \left| \frac{\text{largest singular value}}{\text{smallest singular value}} \right|.$$

Ideally, when $cond(\boldsymbol{Q}) = 1$, the system being evaluated is in good condition. However, when $cond(\boldsymbol{Q}) \gg 1$, the system is ill-conditioned or nearly singular.

3.3.1.1 Computation of Condition Number

The computation of the condition numbers of torque matrix $\boldsymbol{Q}$ is illustrated in Fig. 3.10. Torque matrix $\boldsymbol{Q}$ can be calculated corresponding to a rotor orientation within the workspace, and thus the condition number. If the condition number of $\boldsymbol{Q}$ is much great than 1, then it is assumed a singular matrix, i.e., the corresponding rotor orientation is a singular point. Repeat this computation by varying the angles ϕ_r, θ_r and δ_r within their ranges. Based on all condition numbers obtained, the singularity property of the PM spherical actuator workspace can be evaluated.

3.3.1.2 Visualization of Computational Result of Condition Numbers

The variation of the condition numbers can be visualized. By fixing ϕ_r at certain values such as $0^\circ, 15^\circ, 30^\circ$, etc, the condition numbers corresponding to different values of θ_r and δ_r can be obtained. Thus, a 3D plot of the condition number, denoted as n_c, with respect to the variation of θ_r and δ_r can be presented visually as a 2D surface. By choosing different ϕ_r, a set of 2D surfaces can be obtained, some of which are shown in Fig. 3.11. Due to the symmetric arrangement of the PM poles about the shaft, only the ranges of $\phi_r = 0^\circ \sim 45^\circ$ and $\delta_r = 0^\circ \sim 45^\circ$ are considered. Referring to Fig. 3.11, we can find that the condition numbers n_c do not vary too

[4] Let $\boldsymbol{Q}$ be a square matrix. Then λ is called an eigenvalue of $\boldsymbol{Q}$ if there exists a nonzero vector $\mathbf{v}$ such that $\boldsymbol{Q}\mathbf{v} = \lambda\mathbf{v}$ [17].

[5] For any matrix $\boldsymbol{Q}$, the square roots of the nonzero eigenvalues of $\boldsymbol{Q}^*\boldsymbol{Q}$ are called singular values of $\boldsymbol{Q}$, where $\boldsymbol{Q}^*$ denotes the adjoint or conjugate transpose of $\boldsymbol{Q}$ [18].

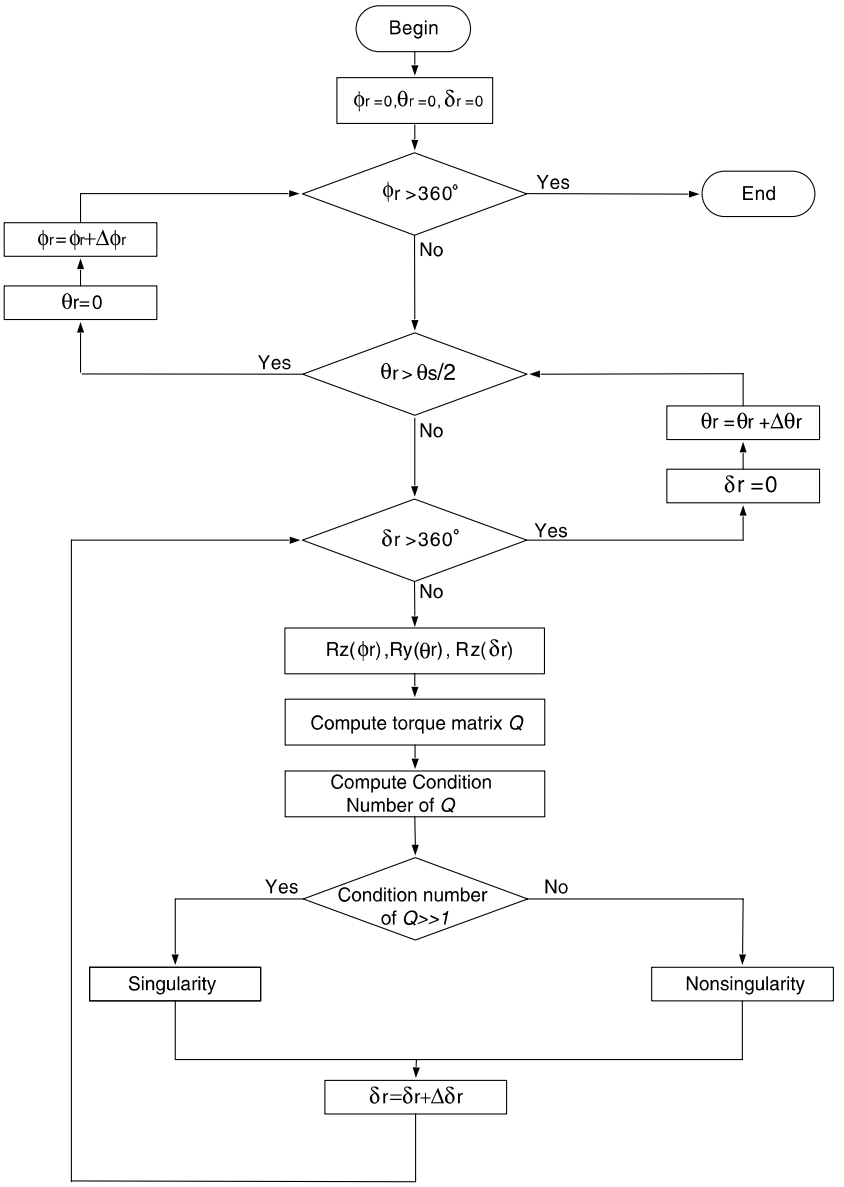

Fig. 3.10: Computation of condition number of torque matrix $\boldsymbol{Q}$ within the workspace of the spherical actuator

much with respect to δ_r and ϕ_r because of the evenly distributed PM poles along the rotor equator.

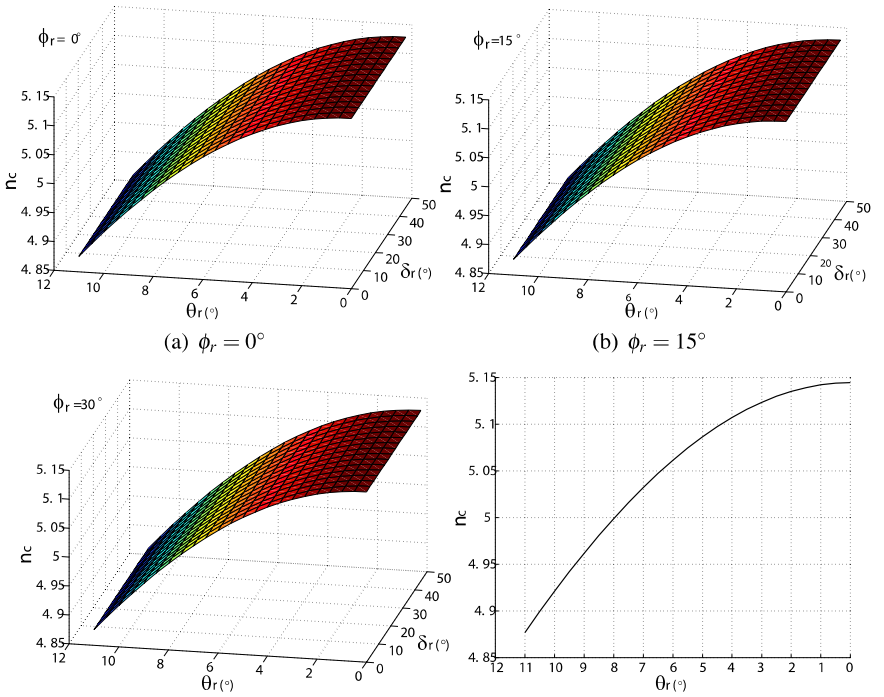

(a) $\phi_r = 0°$ (b) $\phi_r = 15°$

(c) $\phi_r = 30°$ (d) Section view for $\phi_r = 30°$ and $\delta_r = 0$

Fig. 3.11: Condition number of torque matrix $\boldsymbol{Q}$

Through computing the condition number of $\boldsymbol{Q}$ within the workspace of the spherical actuator, it can be found that the minimum value of the condition number is 4.877, whereas the maximum value is 5.145, which is in the same order magnitude of 1. Therefore the workspace of this PM spherical actuator is completely singularity-free.

3.3.2 Minimum Right-inverse Solution of Electromagnetics

As there is no singularity within the workspace of the rotor, there are infinite solutions to Eqn. (3.32). This fact offers an opportunity to optimize the solution of inverse electromagnetics. In order to improve the actuator efficiency, the optimization of the inverse electromagnetics solution in this study aims at minimizing the electric power consumption under current input. This can be formulated as follows.

$$\textbf{Minimize} \qquad \frac{1}{2}\mathbf{J}^T \boldsymbol{W}\mathbf{J}, \tag{3.47}$$

$$\textbf{Subject to} \qquad \mathbf{T} = T_c \boldsymbol{Q}\mathbf{J}, \tag{3.48}$$

where $\mathbf{J}$ is current input vector, $\boldsymbol{W}$ is a positive definite matrix in the form of

$$\boldsymbol{W} = \begin{bmatrix} w_1 & 0 & \cdots & 0 \\ 0 & w_2 & & \vdots \\ \vdots & & \ddots & 0 \\ 0 & \cdots & 0 & w_N \end{bmatrix},$$

$w_1, w_2, ..., w_N$ are positive weightings determined by coils' resistance. As an effective technique to solve this problem, the *minimum right-inverse solution* [19] is employed to obtain the solution of current input

$$\mathbf{J} = \begin{bmatrix} J_1 \\ J_2 \\ \vdots \\ J_N \end{bmatrix} = \boldsymbol{Q}^{RM}\mathbf{T}/T_c,$$

where $\boldsymbol{Q}^{RM}$ is the minimum right inverse of $\boldsymbol{Q}$ computed by

$$\boldsymbol{Q}^{RM} = \boldsymbol{W}^{-1}\boldsymbol{Q}^T(\boldsymbol{Q}\boldsymbol{W}^{-1}\boldsymbol{Q}^T)^{-1},$$

and $\boldsymbol{Q}^T$ is the transpose of $\boldsymbol{Q}$, $\boldsymbol{W}^{-1}$ is the inverse of $\boldsymbol{W}$. The similar minimum right-inverse solution approach was applied to VRSM by Zhou [20] to obtain the control vector of currents.

3.4 Summary

By utilizing the magnetic field model derived in Chapter 2, this chapter has presented the formulation of the actuator torque caused by the interaction between current carrying coils and the magnetic field of the PM-pole rotor according to Lorentz force law. This torque model relates the torque output of the spherical actuator to the current inputs of coils as well as the rotor orientation, which indicates that the torque output of the PM spherical actuator is orientation dependant. Nonsingularity is one of the important advantages of this PM spherical actuator. Based on the torque model, existence of inverse electromagnetics solution or nonsingularity workspace of the PM spherical actuator is verified through the condition number of the torque matrix. In addition, the minimum right-inverse electromagnetics solution is proposed to calculate the required current inputs for desired torque output. This solution can minimize the electric power consumption of the spherical actuator.

In VRSM developed by Lee *et al*. [20], a non-linear torque model has been derived, i.e., the torque output is a quadratic function current inputs. The non-linearity makes the real-time motion control of VRSM very complex. In the study of the proposed PM spherical actuator, the torque output is directly proportional to the current input, which facilitates the position and velocity control of the actuator. This analytical torque model can be used as a tool for the spherical actuator design to maximize the actuator torque output.

References

1. Gieras J F, Wing M et al (1998) Permanent Magnet Motor Technology. Marcel Dekker, Inc., New York, USA, 1998.
2. Hamler A, Hribernik B, Likar M, Guid N et al (1995) Torque Calculation by Bernstein Bezier's Surfaces. IEEE Transactions on Magnetics, vol. 31, no. 3:1885–1887, May 1995.
3. Im D H, Kim C E et al (1994) Finite Element Force Calculation of a Linear Induction Motor Taking Account of the Movement. IEEE Transactions on Magnetics, vol. 30, no. 5:3495–3498, September 1994.
4. Yamasawa K, Suzuki S, Biringer P P et al (1990) A Proposal for a Finite-Element Force Approximation an Automotive Magnetic Actuator. IEEE Transactions on Magnetics, vol. 26, no. 4:1270–1273, July 1990.
5. Davey K, Vachtsevanos G, Powers R et al (1987) The analysis of fields and torques in spherical induction motors. IEEE Transactions on Magnetics, vol. 9, no. 1:273–282, January 1987.
6. Krause P C, Wasynczuk O et al (1989) Electromechanical Motion Devices. McGraw-Hill, Inc., USA, 1989.
7. Lee K M, Roth R B, Zhou Z et al (1996) Dynamic modeling and control of a ball-joint-like variable-reluctance spherical motor. ASME Journal of Dynamic Systems, Measurement, and Control, vol. 118:29–40, March 1996.
8. Lee K M, Sosseh R A et al (2002) Effects of the Torque Model on the Control of a VR Spherical Motor. Proceedings of the 2nd IFAC Conference on Mechatronic Systems, Berkeley, California, USA, 9–11 December 2002.
9. Roth R B (1992) An Experimental Investigation and Optimization of a Variable Reluctance Spherical Motor. Thesis of Georgia Institute of Technology, GA, USA, 1992.
10. Sahoo S K, Zheng Q, Panda S K, Xu J X et al (2003) Model-based torque estimator for switched reluctance motors. Proceedings of The Fifth International Conference on Power Electronics and Drive Systems, PEDS, vol. 2:959–963, Singapore, 17–20 November 2003.
11. Materu P, Krishnan R et al (1990) Analytical prediction of SRM inductance profile and steady-state average torque. Conference Record of the 1990 IEEE Industry Applications Society Annual Meeting, vol. 1:214–223, Seattle, WA, USA, 7–12 October 1990.
12. Sadiku N O M (2001) Elements of Electromagnetics. Oxford University Press, UK, 2001.
13. Sathuvalli U B, Bayazitoglu Y et al (1996) The lorentz forces on an electrically conducing sphere in an alternating magnetic field. IEEE Transactions on Magnetics, vol. 32, no. 2:386–399, March 1996.
14. Wang J, Jewell G W, Howe D et al (2003) Analysis of a spherical permanent magnet actuator. Journal of Applied Physics, vol. 81, no. 8:4266–4268, April 1997.
15. Wang J, Wang W, Jewell G W, Howe D et al (1998) A novel spherical actuator with three degrees-of-freedom. IEEE Transactions on Magnetics, vol. 34, no. 4:2078–2080, July 1998.
16. Craig J J (1989) Introduction to Robotics: Mechanics and Control. Addison-Wesley Publishing Company, USA, 1989.
17. Wilde C (1988) Linear Algebra. Addison-Wesley Publishing Company, USA, 1988.
18. Griffel D H (1989) Linear Algebra and Its Applications. Ellis Horwood Limited, UK, 1989.

19. Nakamura Y (1991) Advanced Robotics: Redundancy and Optimization. Addision-Wesley Publishing Company, USA, 1991.
20. Zhou Z (1995) Real-Time Control and Characterization of a Variable Reluctance Spherical Motor. Thesis of Georgia Institute of Technology, GA, USA, May 1995.

Chapter 4
Prototype Development

Prototype development is an essential step to ensure the functionalities of the proposed 3-DOF PM spherical actuator. The research prototype can be used for conducting experimental works on magnetic field distribution as well as actuator torque output to verify the derived analytical models. This chapter discusses the prototype development of the PM spherical actuator with detail considerations in the design of the rotor poles and stator poles. In nature, both rotor and stator poles are crucial components for generating the actuator torque. The prototype design here is aimed at an actuator with the following features.

- A 3-DOF rotational motion can be achieved for the rotor.
- The actuator torque output is maximized by choosing appropriate values of structural parameters of rotor and stator poles.
- The frictional torque exerted on the rotor is reduced as it may affect the working efficiency of the actuator and make the actuator motion control complex.
- This actuator prototype facilitates the experimental measurement on magnetic field and torque output.
- The eddy current on the stator created by the rotor is avoided because it may retard the rotor motion.

4.1 Introduction

Here, an overview of the developed prototype of the PM spherical actuator is presented and the equations that will be used for actuator design are listed. The component design will be described in detail subsequently.

L. Yan et al., *Design, Modeling and Experiments of 3-DOF Electromagnetic Spherical Actuators*, Mechanisms and Machine Science 4,
DOI 10.1007/978-94-007-1646-9_4,

4.1.1 Prototype of PM Spherical Actuator

A research prototype of the 3-DOF PM spherical actuator has been developed. As shown in Fig. 4.1 (exploded view) and Fig. 4.2 (assembly view), this prototype consists of a ball-like rotor housed in a shell-like stator. The rotor is connected to the stator through a spherical bearing. Eight PM poles are evenly arranged along the rotor equator. The stator has twenty-four coils which are evenly grouped into two layers and symmetrically placed with respect to its equator. The specification of the prototype is listed in Table 4.1. The maximum tilting range can be increased up to about 45° by incorporating more layers of coils. This research prototype can be employed for the experimental investigation on magnetic field and torque variation to verify the theoretical models of magnetic field and torque output.

Table 4.1: Specifications of 3-DOF PM spherical actuator prototype

Inner / outer stator radius	95/112.5 (mm)
Rotor radius	46.5 (mm)
Rotor core radius	23 (mm)
PM pole material	NdFeB 37N25EH
PM pole angular parameters	α=40°, $\beta = 70°$
Number of rotor poles (PM)	8
Number of stator poles (coil)	24/2 layers
Number of coil turns	900
Coil Wire type	AWG24
Maximum tilting angle	$\pm 11°$
Maximum torque	4 (Nm)

4.1.2 Equations for Actuator Design

In Chapter 3, an analytical torque model of the spherical actuator has been formulated in terms of the critical parameters of the PM poles and air-core coils. Based on the torque model, appropriate values of structural parameters can be selected so that high actuator torque can be achieved. To facilitate the discussion, the equations which will be used for actuator design are listed in Table 4.2. From the torque model of Eqn. (3.33), it can be seen that the torque matrix $\boldsymbol{Q}$ is completely determined by positions of coil axis (θ_i, ϕ_i) which in turn is determined by rotor orientations with respect to the stator frame. The constant T_c is defined by structural parameters of PM poles (longitudinal angle α, latitudinal angle β, rotor core radius R_b and rotor radius R_r in Fig. 2.2) and those of coils (the center distance of the inner surface of the coil

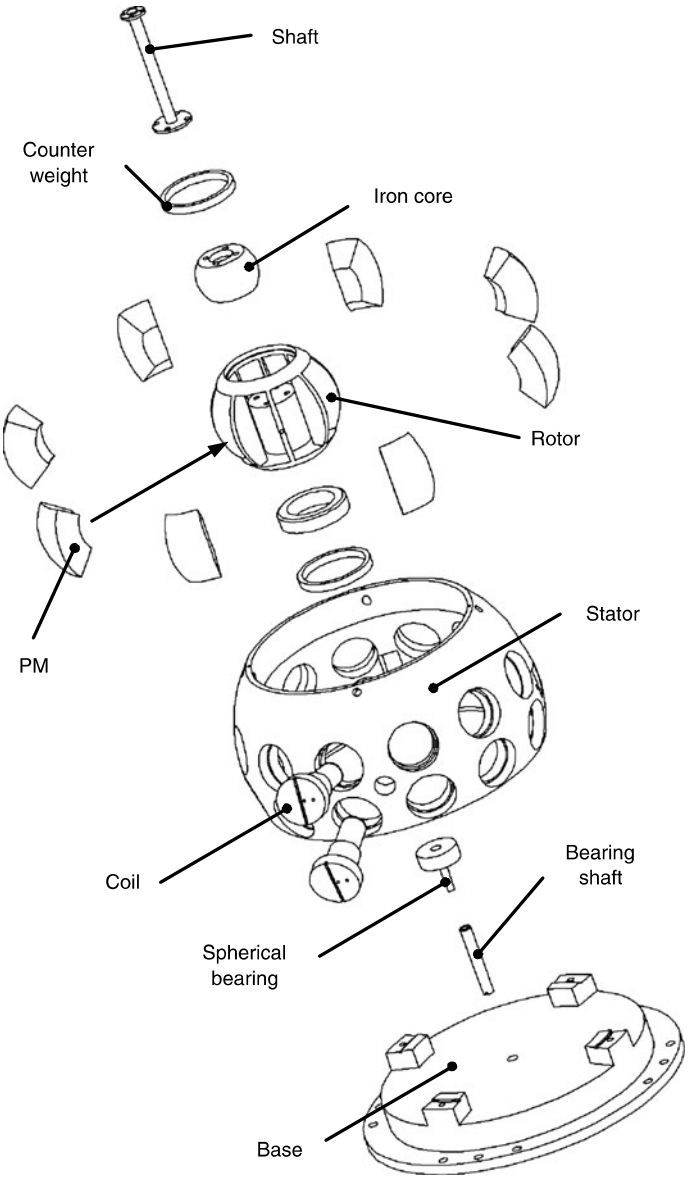

Fig. 4.1: Exploded view of spherical actuator prototype

Table 4.2: Equations used for prototype design

Torque model	$\mathbf{T} = T_c \boldsymbol{Q} \mathbf{J}$	Eqn. (3.33)
Torque matrix	$\boldsymbol{Q} = \begin{bmatrix} g_x(\theta_1,\phi_1)\ g_x(\theta_2,\phi_2)\ \cdots\ g_x(\theta_N,\phi_N) \\ g_y(\theta_1,\phi_1)\ g_y(\theta_2,\phi_2)\ \cdots\ g_y(\theta_N,\phi_N) \\ g_z(\theta_1,\phi_1)\ g_z(\theta_2,\phi_2)\ \cdots\ g_z(\theta_N,\phi_N) \end{bmatrix}$	Eqn. (3.34)
Constant T_c	$T_c = \frac{15}{16}\sqrt{\frac{35}{2}}\mu_0 M_0 a c d_4 R_c G_\zeta$	Eqn. (3.31)
Constants a, b, c	$a \pm bi \equiv \int_0^{2\pi} f(\phi) e^{-im\phi} d\phi,\ (m = \pm 4)$	Eqn. (2.23)
	$c/\sqrt{\pi} \equiv \int_0^{\pi} \sqrt{\frac{2n+1}{4\pi}\frac{(n-m)!}{(n+m)!}} \sin^2\theta [P_n^m(\cos\theta)] d\theta$ $(n = 4, m = \pm 4)$	Eqn. (2.24)
	$f(\phi) = (-1)^{p-1}\cos[\phi - \frac{\pi}{4}(p-1)],\ p = 1,2,...,8.$	Eqn. (2.22)
	$\frac{\pi}{4}(p-1) - \frac{\alpha}{2} < \phi < \frac{\pi}{4}(p-1) + \frac{\alpha}{2}$	Eqn. (2.17)
	$\frac{\pi}{2} - \frac{\beta}{2} < \theta < \frac{\pi}{2} + \frac{\beta}{2}$	Eqn. (2.18)
Constant d_4	$d_4 = -d_4^{\top}/d_4^{\perp}$	Eqn. (2.42)
	$d_4^{\top} = R_r^6 + \frac{9\mu_m R_b^6 R_r^9}{4(\mu_r - \mu_m)R_b^9 - (4\mu_r + 5\mu_m)R_r^9}$	
	$d_4^{\perp} = 5(\mu_m - 1) + \frac{9\mu_m(4\mu_r + 5\mu_m)R_r^9}{4(\mu_r - \mu_m)R_b^9 - (4\mu_r + 5\mu_m)R_r^9}$	
Constant R_c	$R_c = R_0^{-2} - R_1^{-2}$	Eqn. (3.12)
Constant G_ζ	$G_\zeta = G_\zeta'' - \frac{3G_\zeta'}{4}$	Eqn. (3.25)
	$G_\zeta' = \frac{1}{5}\sin^5\zeta_1 - \frac{1}{5}\sin^5\zeta_0$	
	$G_\zeta'' = \frac{1}{5}\cos^4\zeta_0 \sin\zeta_0 - \frac{1}{15}\cos^2\zeta_0 \sin\zeta_0 - \frac{2}{15}$ $\sin\zeta_0 - \frac{1}{5}\cos^4\zeta_1 \sin\zeta_1 + \frac{1}{15}\cos^2\zeta_1 \sin\zeta_1 + \frac{2}{15}\sin\zeta_1$	
Magnetic field	$B_{Ir} = \frac{15\mu_0 M_0 a c d_4}{8\pi}\sqrt{\frac{35}{2}} r^{-6}\sin^4\theta\cos 4\phi$	Eqn. (2.52)

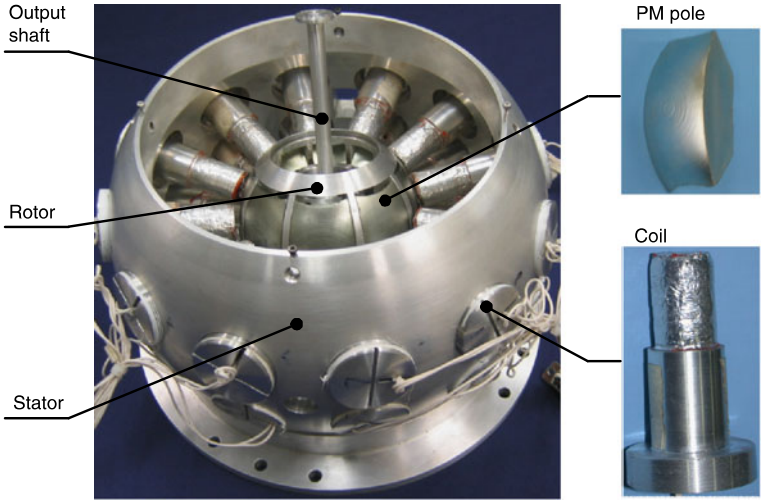

Fig. 4.2: Fabricated 3-DOF PM spherical actuator

R_0, the center distance of the outer surface of the coil R_1, the angular diameter of the air-core ζ_0 and the angular diameter of the coil ζ_1 in Fig. 3.5). Each of constants a, c, d_4, R_c and G_ζ in T_c can be calculated from pole parameters. Therefore, the effect of pole parameters on the torque output of the actuator can be evaluated through these constants.

The relation between pole parameters and the torque output is illustrated in Fig. 4.3 specifically. The longitudinal angle α of the PM pole (Fig. 2.2) is related to constant a through Eqns. (2.23) and (2.17), whereas latitudinal angle β is related to constant c through Eqns. (2.24) and (2.18). Constant d_4 is specified by the rotor radius R_r and rotor core radius R_b through Eqn. (2.42). According to the torque model of Eqns. (3.33), (3.31) and the magnetic field model of Eqn. (2.52), large a, c and d_4 can increase the torque output of the actuator as well as the magnetic flux density of PM rotor, which is consistent with the fact that high magnetic flux density can produce high torque generally. By inspecting the variation of a, c and d_4 with respect to pole parameters, values of PM-pole parameters can be determined to achieve high torque output capacity as well as high magnetic flux density of the actuator.

Similarly, R_c is defined by coil parameters R_0 and R_1 through Eqn. (3.12) and G_ζ is defined by angular parameters ζ_0 and ζ_1 through Eqn. (3.25). Eqn. (3.31) indicates that high values of R_c and G_ζ are preferred by high torque output. Therefore, coil dimensions can be designed to achieve high torque output capacity through observing the variation of R_c and G_ζ with respect to coil parameters.

According to the above discussion, it can be found that the constants a, c, d_4, R_c and G_ζ are affected by different pole parameters separately. Therefore, appropriate

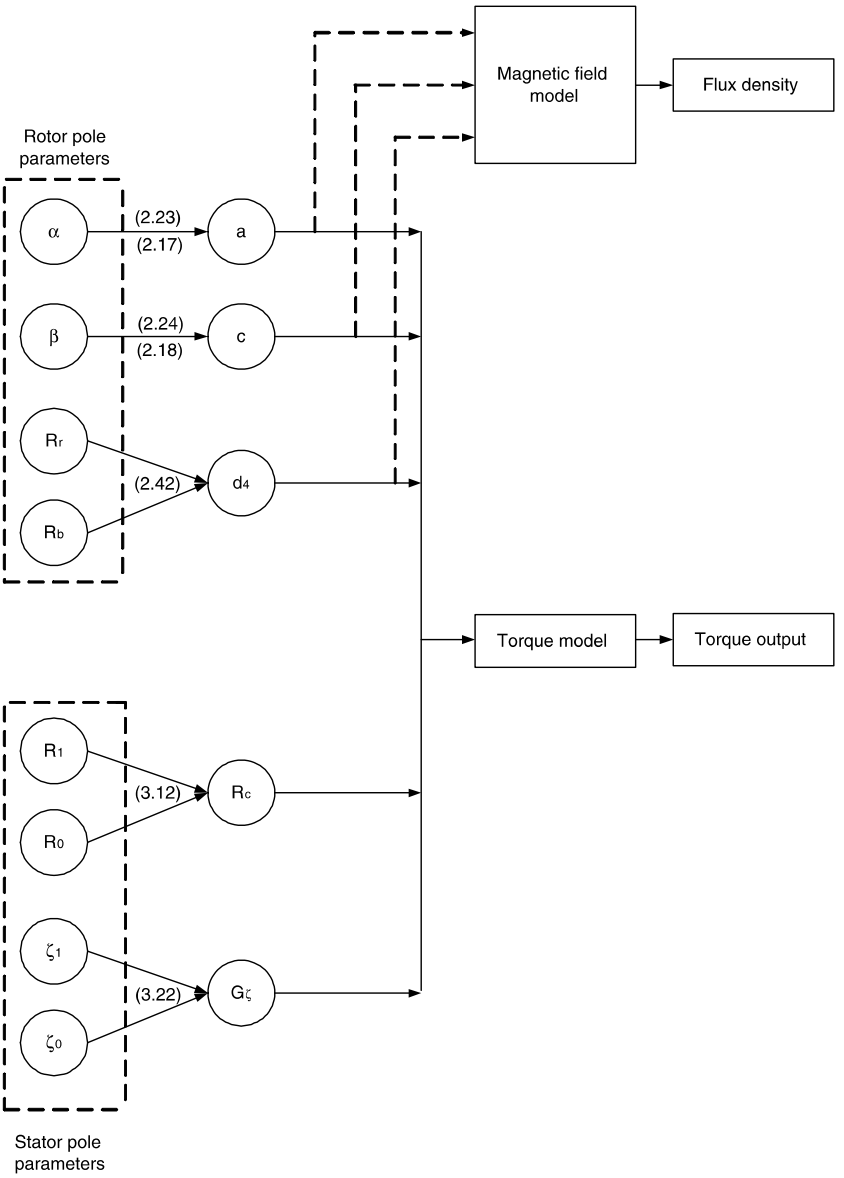

Fig. 4.3: Relation between pole (PM & coil) parameters and torque output

pole parameters can be selected to achieve maximum value for each constant, thus to maximize the torque output.

4.2 Rotor Pole Design

The task of the rotor pole design is to select appropriate rotor pole dimensions α, β, R_r and R_b to maximize the actuator torque output capability.

4.2.1 Longitudinal Angle α versus a

Constant a can be calculated from α through Eqn. (2.23) and the integral range in Eqn. (2.17). Because eight PM poles are installed along the equator of the rotor, the maximum value of α is 45°. By varying the value of α between 0 to 45 degrees, the relation between α and a is shown in Fig. 4.4. According to Fig. 4.4, a increases with the increase of α. Furthermore, according to Eqns. (3.31) and (3.32), large value of a is helpful for high torque output. Therefore, in order to achieve high torque output of the spherical actuator, the optimum value of α is supposed to be 45°.

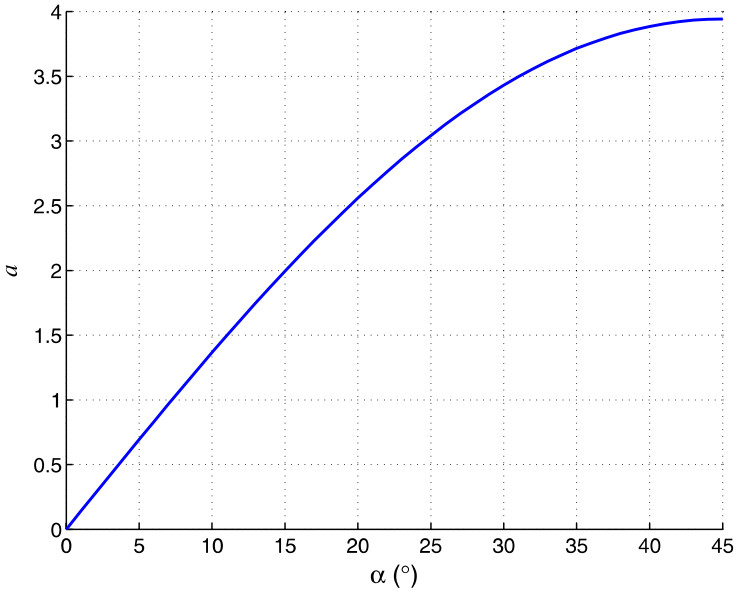

Fig. 4.4: Pole parameter α vs. constant a

From physical perspective, large α represents large volume of magnetized material, which can create large flux density thus large torque output generally.

4.2.2 Latitudinal Angle β versus c

Similarly, according to Eqns. (3.32) and (3.31), large c also contributes to high torque output. Constant c is calculated from Eqn. (2.24) and the integral range in Eqn. (2.18) specified by the angle β ($0 \sim 180^\circ$) of the PM pole. Let $\beta_1 = \beta/2$, where β_1 varies from 0 to 90°. The relation between β_1 and the constant c is shown in Fig. 4.5 and it shows that after $\beta_1 = 60^\circ$, c reaches the largest value. Hence, high torque output can be achieved within the range of $60^\circ \leq \beta_1 \leq 90^\circ$. For $\beta_1 > 60^\circ$, the inertia moment of the rotor increases, which affects the dynamic performance of the spherical actuator. Thus, the optimum value of β_1 should be 60°. The curve in Fig. 4.5 has the following physical meaning. The increase of β_1 indicates increase of magnet volume, which leads to high flux density and thus high torque output. However, when β_1 increases to a certain degree, the volume increase of magnet is much less. Furthermore, as illustrated in Fig. 4.6, when β is large ($\beta'' > \beta'$), the distance between neighboring PM poles becomes smaller ($L'' < L'$), thus the reducing effect of flux density between these two opposite magnetized poles becomes evident.

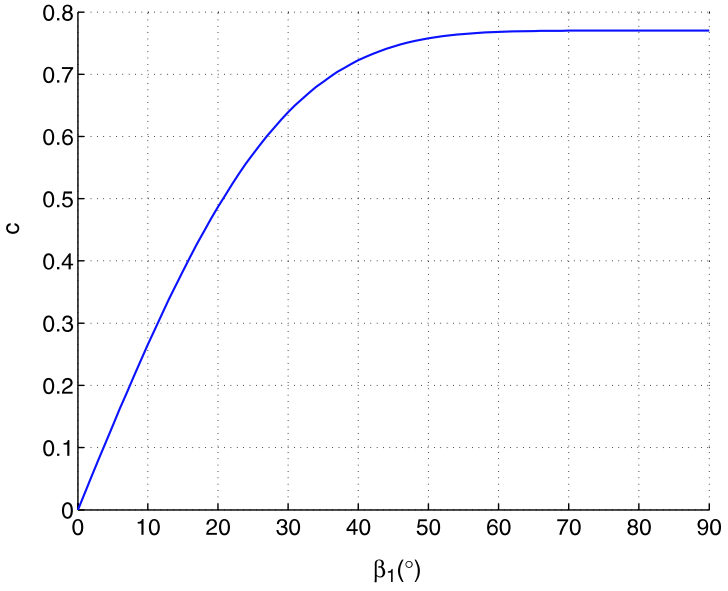

Fig. 4.5: Pole parameter β_1 vs. c

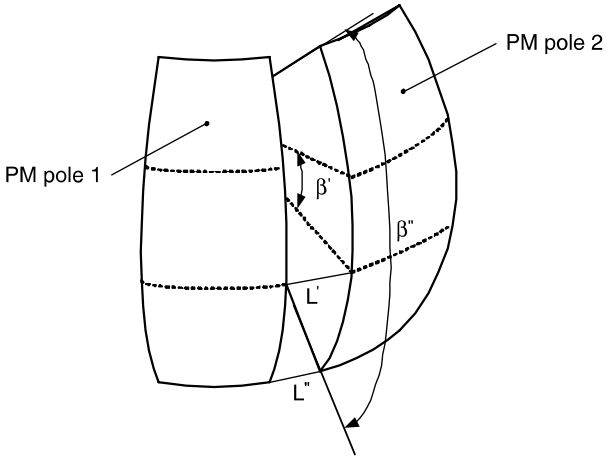

Fig. 4.6: Distance between PM poles

Therefore, the effect of β on the increase of actuator torque output is negligible when it is large.

4.2.3 Rotor Radius R_r versus d_4

According to Eqns. (3.31) and (2.52), both torque output and magnetic flux density are proportional to the constant d_4. In order to simplify the study of R_r, let $R_b = 0$. Figure 4.7 illustrates the relationship between R_r and d_4 explicitly. Approximately, d_4 increases exponentially with respect to R_r. This is due to the fact that the increase of magnet volume with respect to R_r is fast when R_r is large, which yields fast increase of magnetic field and torque output. Therefore, large rotor is preferred to create a high flux density as well as high torque output. Due to mechanical constraint in the spherical actuator, the rotor size is chosen as 46.5mm for prototype development.

4.2.4 Rotor Core Radius R_b versus d_4

Similarly, from the torque model, large d_4 is preferred in order to achieve high torque. With $R_r = 46.5$mm, the relation between R_b and d_4 is shown in Fig. 4.8. It can be seen that small R_b produces large d_4, and thus high torque output as well as high flux density. However, when R_b is reduced to a certain size, i.e., 23mm, there is no increase of constant d_4. In other words, when $R_b < 23$, the decrease of R_b

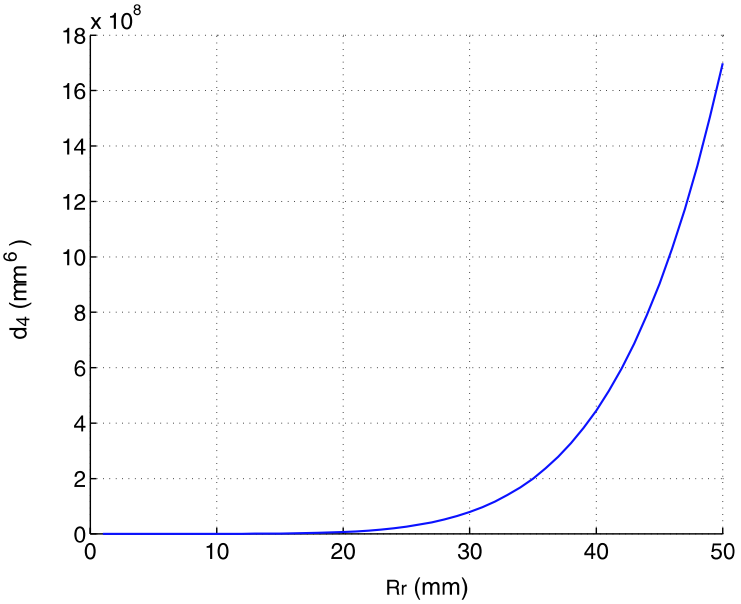

Fig. 4.7: R_r vs. d_4

does not contribute much to increase magnetic flux density and torque output. This justifies the assumption of $R_b = 0$ when evaluating the effect of R_r in Section 4.2.3. The relation in Fig. 4.8 can be explained as follows. It is known that the smaller is R_b, the larger the size of PM pole is. Thus the magnetic field and torque output increase. However, when R_b is less than a certain degree, the volume increase of magnetized material is much less and the contribution to the magnetic flux density and torque output is negligible. As a result, the optimum R_b is equal to 23mm. This design creates a hollow space at the center of the rotor core for assembly of a spherical bearing. The hollow core also reduces the inertia moment of the PM-pole rotor.

4.2.5 Relative Permeability μ_r versus d_4

Constant d_4 in Eqn. (2.42) can also be used to observe the effect of relative permeability μ_r of ferromagnetic materials on the torque output of the spherical actuator. According to Eqn. (2.42), the relation between μ_r and d_4 can be seen in Fig. 4.9. When μ_r is less than 50 in Fig. 4.9(a), its effect on d_4 is evident. However, when μ_r is greater than 400 (Fig. 4.9(b)), d_4 does not change with respect to μ_r. In other words, when the permeability of Region *III* is very large, the impact of material

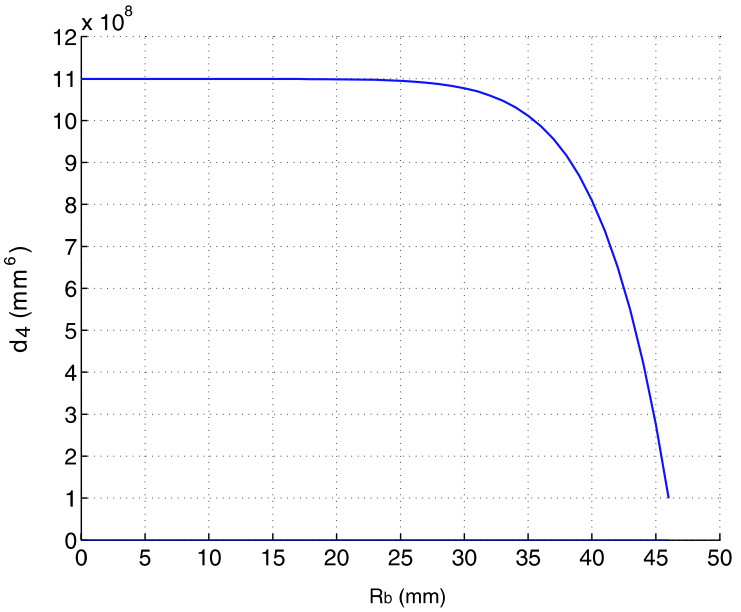

Fig. 4.8: Determination of R_b

selection of the rotor core in Region Ⅲ on the torque output of the PM spherical actuator becomes invariable.

4.2.6 Result of PM Pole Design

The final dimensions of the PM pole using rare-earth material NdFeB 37N25EH have been determined based on the above discussion, i.e., $\alpha = 45°$, $\beta = 120°$, $R_r = 46.5$mm and $R_b = 23$mm. However, for the actual prototype, $\alpha = 40°$ is used to replace $\alpha = 45°$ and $\beta = 70°$ is used to replace $\beta = 120°$ to facilitate the fabrication of PM poles. It can be seen from Fig. 4.4 and 4.5, this replacement does not change the torque output much. Instead, the size reduction of PM poles provides a space for a fixture design to hold PM poles. Furthermore, the mass/inertia moment of the rotor is reduced considerably (about 50%).

4.3 Coil Pole Design

Besides the PM poles, the other critical element generating torque in the PM spherical actuator is the air-core coil. Similar to the PM pole design, the effect of coil parameters on the torque output of the actuator can be described so that appropriate values of coil parameters can be chosen to achieve high torque output capacity of the spherical actuator. In addition to the geometric parameters of coils, large number

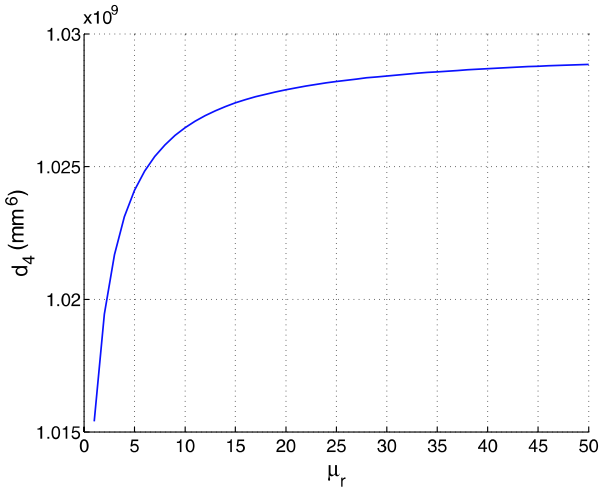

(a) $0 < \mu_r < 50$

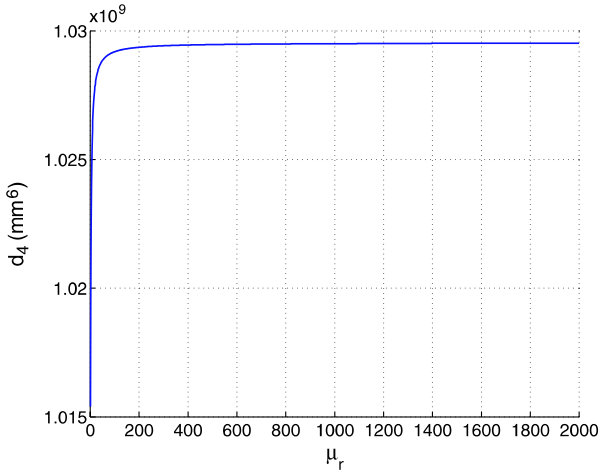

(b) $0 < \mu_r < 2000$

Fig. 4.9: Effect of μ_r on d_4

of winding turns also benefits high torque output. Several factors of fabricating coils that can increase the winding turns are discussed here, such as the packing patterns of coils, diameter of wires and optional coil-frame structures.

4.3.1 Geometric Parameters of Coil

As shown in Fig. 3.5, four parameters are used to specify the coil shape, i.e., R_0, R_1, ζ_0 and ζ_1. R_0 and R_1 can be replaced by the length of coil denoted as $L_c = R_1 - R_0$. In the following discussion, the values of three parameters ζ_0, ζ_1 and L_c will be determined.

4.3.1.1 Determination of Coil Length

Constant R_c is defined with R_0 and R_1 as indicated in Eqn. (3.12). Let $R_0 \approx R_r$(46.5mm), i.e., the coil tip is very close to the rotor surface, because the flux density is high near the rotor surface. By using L_c, Eqn. (3.12) becomes

$$R_c = R_0^{-2} - R_1^{-2} = R_r^{-2} - (R_r + L_c)^{-2}. \tag{4.1}$$

The relation between L_c and R_c is illustrated in Fig. 4.10(a). It can be seen that increasing L_c, R_c will increase, and thus torque output increases. Large L_c implies that more wires are enclosed in the winding volume, for high actuator torque output. The rate of increment in R_c versus L_c is illustrated in Fig. 4.10(b). It can be found that when the length of coil exceeds 230mm, $\Delta R_c/\Delta L_c$ is close to zero. R_c does not increase further when $L_c > 230$mm as the magnetic flux density becomes very small at the distance far away from the rotor surface. The increased wire winding in this region, therefore, has negligible effect on the torque generation. Hence, to achieve high torque output, the optimum value of L_c can be kept at 230mm theoretically. Nevertheless, according to $\Delta R_c/\Delta L_c$-curve in Fig. 4.10(b), the increment rate $\Delta R_c/\Delta L_c$ for $L_c = 30$mm is only one quarter of the maximum $\Delta R_c/\Delta L_c$, i.e., the torque contribution from coil turns beyond $L_c = 30$mm is not evident. Excessive winding increases the electrical power consumption. Therefore, $L_c = 30$mm can be chosen for the actual coil design of the PM spherical actuator.

4.3.1.2 Determination of Coil Angles

As indicated in Eqn. (3.25), G_ζ is defined with two coil angles ζ_0 and ζ_1. Therefore, by describing the relation between G_ζ and these angular parameters, appropriate ζ_0 and ζ_1 can be determined to obtain high torque.

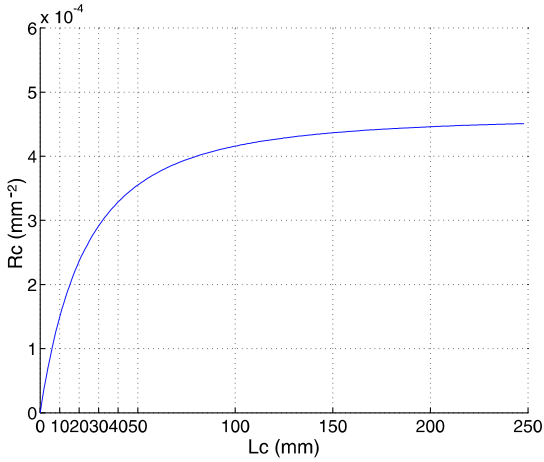

(a) R_c vs. L_c

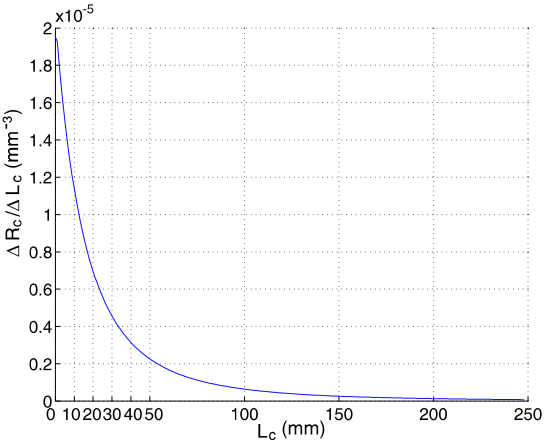

(b) Increasing speed of R_c vs. L_c

Fig. 4.10: Effect of L_c on R_c

Determination of ζ_1:

To facilitate the discussion, let $\zeta_0 = 0$, hence G_ζ is a function of angle ζ_1. According to Eqn. (3.25), the relation between ζ_1 and G_ζ is plotted in Fig. 4.11. It can be found that the effect of ζ_1 on G_ζ is prominent. With reference to Fig. 3.5, when ζ_1 is large, the same increment of ζ_1 results in a large increment of wire length, and thus the torque increases fast. The maximum value of ζ_1 is approximately 15° because there are twelve coils for each layer of stator poles. To achieve high torque output, $\zeta_1 = 15°$ is the optimum value.

Determination of ζ_0:

The core angle ζ_0 in the coil also affects the torque output capacity of the spherical actuator. By fixing ζ_1 at 15°, the relation between G_ζ and ζ_0 is plotted in Fig. 4.12 according to Eqn. (3.25). When ζ_0 increases, the value of G_ζ decreases, thus the torque output decreases. However, when ζ_0 is less than 2°, G_ζ is approximately a constant of 1.39×10^{-3}. Usually the smaller ζ_0, the longer the winding length and the larger the torque output. But when ζ_0 is smaller than a certain value, variation of ζ_0 does not affect the wire length on the coil evidently and the variation of torque is ignorable. This justifies the condition of $\zeta_0 = 0$ when we discuss the optimum value of ζ_1. The value of $\zeta_0 = 2°$ offers two additional advantages. First, it reduces the electrical power consumption whereas the torque output is not affected. Second, it provides the space for the design of coil frame on which the wire is wound. Therefore, $\zeta_0 = 2°$ can be used as the optimum value for the coil design of the PM spherical actuator.

4.3.1.3 Optimized and Actual Coil Structures

Thus far, an optimized coil geometry has been obtained as illustrated in Fig. 4.13(a). However, in the actual prototype, off-the-shelf cylindrical coils (Fig. 4.13(b)) are utilized to facilitate the fabrication. It has inner radius (R_{ci}) of 2mm, outer radius (R_{co})

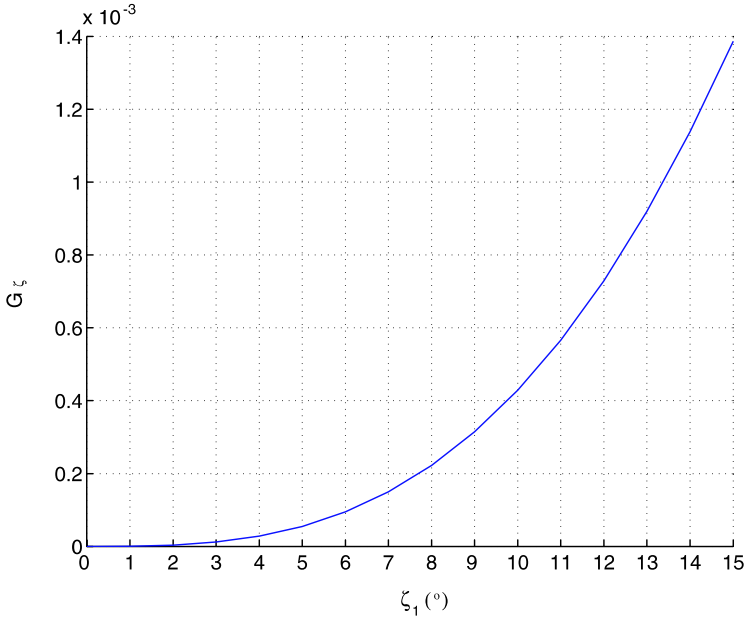

Fig. 4.11: Coil parameter ζ_1 vs. G_ζ ($\zeta_0 = 0$)

of 10mm, length (L_c) of 30mm and 900 turns of winding. It can be approximated with a conical coil with $\zeta_0 = 2°$, $\zeta_1 = 9.5°$ and $L_c = 30$mm in terms of the winding volume. It can be seen from Fig. 4.11 that the value of G_ζ (1.39×10^{-3}) at $\zeta_1 = 15°$ is approximately four times the value (3.5×10^{-4}) at $\zeta_1 = 9.5°$.

Volume comparison between two coil geometries:

In previous study, it is known that the torque model is formulated by integrating the differential torque within the entire coil volume. In order to show the cylindrical coil can be approximated with a conical coil for torque computation, the volumes of these two types of coils will be compared.

1. Volume of conical coil

The conical coil presented in Fig. 4.13(b) can be computed with the difference between the volume enclosed by $ABCD$ (V_{ABCD}) and that enclosed by $A^{'}B^{'}C^{'}D^{'}$ ($V_{A'B'C'D'}$). V_{ABCD} and $V_{A'B'C'D'}$ can be calculated by following equations [1],

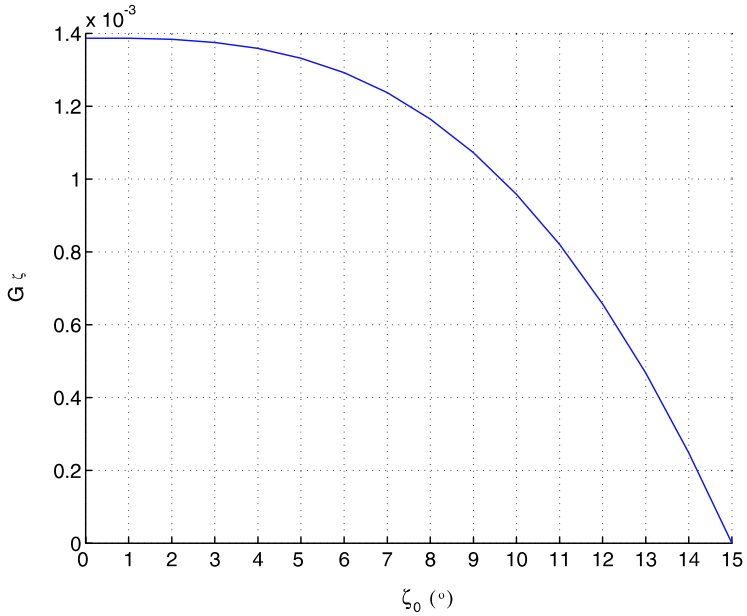

Fig. 4.12: Coil parameter ζ_0 vs. G_ζ ($\zeta_1 = 15°$)

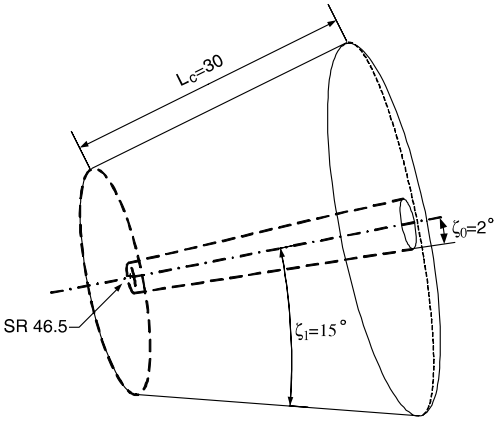

(a) Optimized conical coil

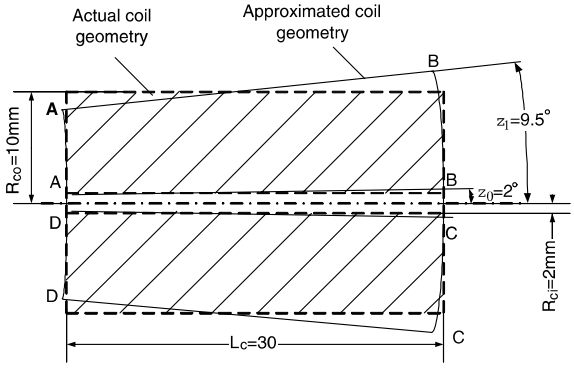

(b) Actual coil (section view)

Fig. 4.13: Different coil geometry

$$
\begin{aligned}
V_{ABCD} &= \frac{2}{3}\pi R_1^3(1-\cos\zeta_1) - \frac{2}{3}\pi R_0^3(1-\cos\zeta_1) \\
&= \frac{2}{3}\pi(R_1^3 - R_0^3) + \frac{2}{3}\pi(R_0^3 - R_1^3)\cos\zeta_1, \\
V_{A'B'C'D'} &= \frac{2}{3}\pi R_1^3(1-\cos\zeta_0) - \frac{2}{3}\pi R_0^3(1-\cos\zeta_0) \\
&= \frac{2}{3}\pi(R_1^3 - R_0^3) + \frac{2}{3}\pi(R_0^3 - R_1^3)\cos\zeta_0.
\end{aligned}
$$

Therefore, the volume of the conical coil is

$$
\begin{aligned}
V_{co} &= V_{ABCD} - V_{A'B'C'D'} \\
&= \frac{2}{3}\pi(R_0^3 - R_1^3)(\cos\zeta_1 - \cos\zeta_0). \qquad (4.2)
\end{aligned}
$$

2. Volume of cylindrical coil
The volume of the cylindrical coil is

$$V_{cy} = \pi R_{co}^2 L_c - \pi R_{ci}^2 L_c = \pi (R_{co}^2 - R_{ci}^2) L_c. \tag{4.3}$$

Substituting parameter values into Eqns. (4.2) and (4.3), it can be found that the ratio between V_{co} and V_{cy} is 1.03. The volumes of two coil geometries are approximately the same. As a result, replacement of the cylindrical coil with the conical coil does not have significant effect on the torque computation.

4.3.2 Increase Number of Winding Turns

Current density of the coil is defined as the electric current passing through unit sectional area of the coil, i.e., [2]

$$J = \frac{\Delta I}{\Delta A} = \frac{\Delta N I_w}{\Delta A}, \tag{4.4}$$

where I_w is the current passing through a single wire, $\Delta I = \Delta N I_w$ is the total current passing through a cross section ΔA of coil. Therefore, increasing the number of winding turns within per unit sectional area of coil improves the current density of the coil and thus the torque output capacity of the spherical actuator. Several approaches are discussed in order to increase the number of winding turns such as, packing pattern of wires, reduction of wire diameters, geometry of coil frames, etc.

4.3.2.1 Comparison of Packing Patterns

The packing pattern of winding affects the number of wire turns placed within a given area. Two possible stacking patterns are studied here. Figure 4.14(a) illustrates the regular packing pattern in which the wires are stacked on row upon another, and Fig. 4.14(b) is the staggering pattern in which each wire conductor is placed above and between the previous row's wires. The density of the patterns can be computed and compared for their effectiveness. Here, the stacking density is defined as the ratio of the occupied cross section area of the wires and the area of the designated square space (Fig. 4.14).

For the regular pattern, stacking density can be computed as following

$$E_1 = \frac{4\pi r_w^2}{16 r_w^2} = 78.5\%, \tag{4.5}$$

where r_w is the radius of the wire.

As for the staggering packing pattern, the total area of wire sections within the square in Fig. 4.14(b) can be expressed as

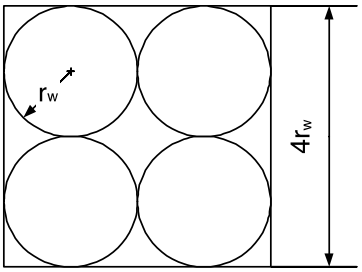

(a) Regular pattern

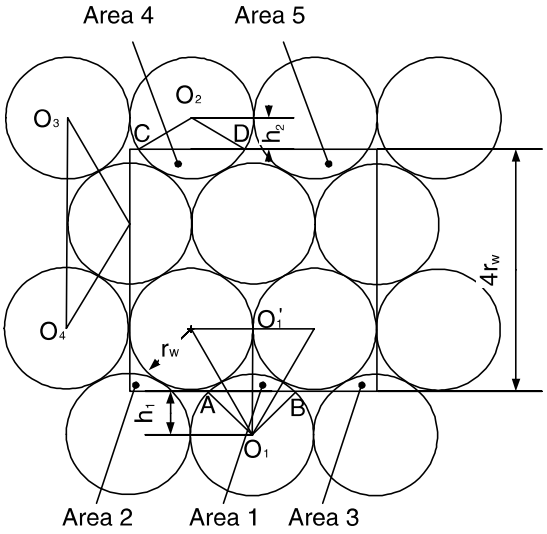

(b) Staggering pattern

Fig. 4.14: Wire packing patterns

$$A_t = 4\pi r_w^2 + 2[r_w^2 \arccos(\frac{h_1}{r_w}) - \sqrt{r_w^2 - h_1^2}h_1] + 2[r_w^2 \arccos(\frac{h_2}{r_w}) - \sqrt{r_w^2 - h_2^2}h_2].$$

Hence, the stacking density is

$$\begin{aligned} E_2 &= \frac{A_t}{16r^2} \\ &= \{4\pi r^2 + 2[r^2 \arccos(\frac{h_1}{r}) - \sqrt{r^2 - h_1^2}h_1] + 2[r^2 \arccos(\frac{h_2}{r}) - \sqrt{r^2 - h_2^2}h_2]\}/16r^2 \\ &= 87.2\%. \end{aligned} \tag{4.6}$$

Comparing E_1 and E_2 shows that the staggering packing pattern offers 10% more stacking density than the regular packing pattern.

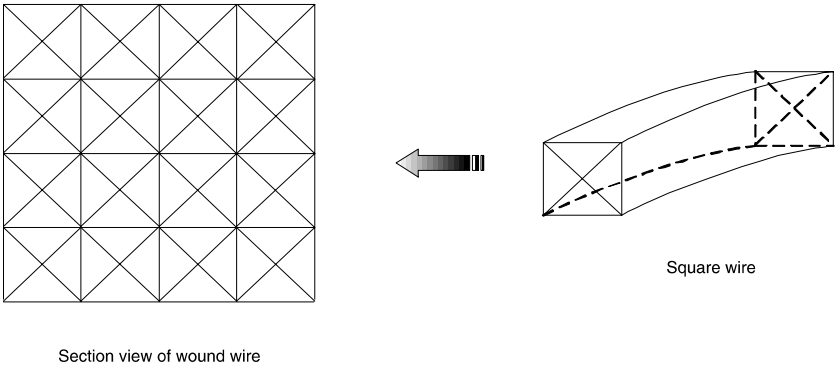

Fig. 4.15: Coil wound with square wire

* Square wire

The above discussion is based on wires with round section. An alternative option is to use square section wire as shown in Fig. 4.15. With the square wire, the packing density will be much larger than the round wire. This square wire also aids in heat dissipation. However, the winding of square wires is more complex than that of round wires due to the fragileness and cost of the square wire. Therefore, in this prototype development, the round wire is employed for coils.

4.3.2.2 Properties of Wires

Wire material:

Presently, most available wires are made either of copper or of aluminum. Specialty magnet wire can be made from silver, gold or platinum whose prices are very high. Aluminum has the advantage of light weight. According to Table 4.3, its density (2.7 g/cm^3) is less than 1/3 of copper's (8.9 g/cm^3). However, comparing with aluminum wires, copper wires also possess significant advantages.

Table 4.3: Properties of copper and aluminum wires [3]

Properties	Copper	Aluminum
Density (g/cm^3)	8.9	2.7
Cross section for same conductivity (cm^2)	100	160
Tensile strength (lb/in^2)	55,000	25,000
Corrosion resistant	good	not good
Compatibility with connectors	good	not good

- The conductivity of copper wires is larger than that of aluminum wires. To offer the same conductance, copper wires can have smaller cross-sections than the equivalent aluminum wires. This means windings wound with copper wires will likely have smaller volume compared with an equivalent aluminum windings. This also indicates that copper building wire requires less insulation and smaller conduits than aluminum.
- The strength of copper (55,000 lb/in^2) is much higher than aluminum conductors (25,000 lb/in^2). It can resist stretching, neck-down, creep, nicks and breaks.
- Copper is corrosion resistant. As a noble metal, copper gives a system high reliability and longevity. The pure copper used in building wire is not subject to galvanic corrosion when connected to other, less noble metals and alloys. Copper wiring will also resist corrosion from moisture, humidity, industrial pollution and other atmospheric influences - to insure safe, trouble-free performance for the life of a system.
- One of the inherent properties of aluminum is that in the presence of oxygen, it quickly forms a very tight oxide skin. A connection to aluminum wire must be properly plated and crimped (or soldered with a special solder) to be gas-tight. This prevents the formation of aluminum oxide film that could raise the resistance of the joint and cause a problem. In contrast, copper, with its compatibility with connectors and other devices, safeguards against these conditions occurring.

Based on the comparison between copper and aluminum wires, copper wire is employed for the windings of this spherical actuator.

Reduction of wire diameter:

Diameter of wires affects the number of winding turns which in turn is closely related to the torque output of the spherical actuator. Generally, small diameter of wires allows more turns of winding to occupy the same area. Analysis is carried out to estimate the increased turns of coils due to diameter reduction of wires. It can be seen from Fig. 4.16 that the height of a single row of coil t_1 is equal to the diameter of the wire $2r_w$. The height of an n_c-layer coil can be computed as:

$$t_{n_c} = 2r_w[1 + \frac{\sqrt{3}}{2}(n_c - 1)]. \tag{4.7}$$

Assuming that the section area of winding is constraint by the height t_v and the width t_h as shown in Fig. 4.16. The height of the coil stack must be equal or less than the height t_v, i.e.

$$2r_w[1 + \frac{\sqrt{3}}{2}(n_c - 1)] \leq t_v. \tag{4.8}$$

The number of layers can be obtained as:

$$n_c = Int[1 + \frac{2}{\sqrt{3}}(\frac{t_v}{2r_w} - 1)], \tag{4.9}$$

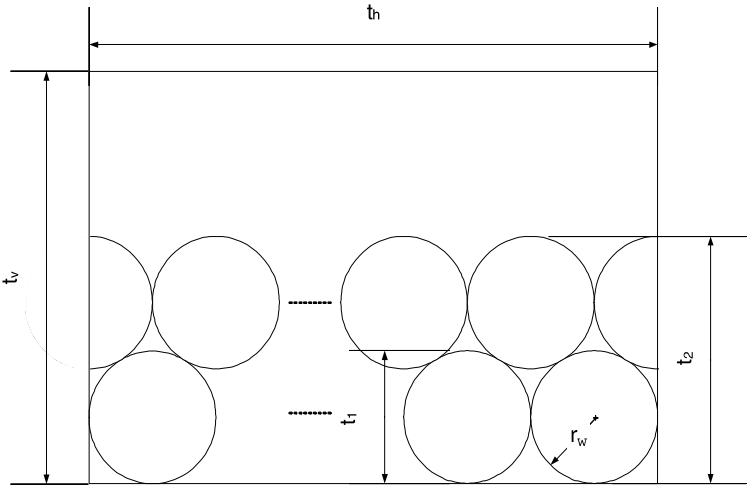

Fig. 4.16: Number of winding turns vs. wire diameter

where *Int* represents the integer of the result value. Similarly, the number of turns m_c for each layer can be computed as

$$m_c = Int(\frac{t_h}{2r_w}). \tag{4.10}$$

Hence, the number of turns that occupies the sectional area in Fig. 4.16 is

$$N_{turn} = Int[1 + \frac{2}{\sqrt{3}}(\frac{t_v}{2r_w} - 1)]Int(\frac{t_h}{2r_w}). \tag{4.11}$$

Suppose that there are two type of wires with radius of r_{w1} and r_{w2}. Correspondingly, the winding numbers of coils using these two type of wires are denoted as N_{turn1} and N_{turn2}. The ratio of N_{turn1} and N_{turn2} can be calculated as

$$\frac{N_{turn1}}{N_{turn2}} = \frac{Int[1 + \frac{2}{\sqrt{3}}(\frac{t_v}{2r_{w1}} - 1)]Int(\frac{t_h}{2r_{w1}})}{Int[1 + \frac{2}{\sqrt{3}}(\frac{t_v}{2r_{w2}} - 1)]Int(\frac{t_h}{2r_{w2}})}. \tag{4.12}$$

Normally, $t_v/2r_{w1}, t_v/2r_{w2} \gg 1$. In this case, Eqn. (4.12) is reduced to

$$\frac{N_{turn1}}{N_{turn2}} \simeq (\frac{r_{w2}}{r_{w1}})^2. \tag{4.13}$$

Given two examples of wires, i.e., American Wire Gauge (AWG) 21 with $r_{w2} =$ 0.38mm (bare wire ϕ0.70mm, with isolation ϕ0.76mm) and AWG24 with $r_{w1} =$ 0.225mm (bare wire ϕ0.40mm, with isolation ϕ0.45mm), it can be known from

Eqn. (4.13) that the ratio of winding turns N_{turn1}/N_{turn2} is nearly equal to 3. Hence, the number of winding turns with AWG24 can increase about three folds than with the coil using AWG21 wire.

Operating temperature of wires:

Besides wire diameters, another important factor that affects the choice of the wire type is the operating temperature of insulation layer of wires. The electric wire used for winding includes the bare wire and the insulation layer. For each kind of insulation layer, there is a maximal working temperature, i.e., heat resistance grade. The highest heat resistance grade (Grade H) of wire, can withstand $220°C$. While the coil with thin wire is preferred for generating high torque, it also produces more heat due to the increased wire turns. Experiments are carried out on the working temperature of AWG21 and AWG24 wires. By using AWG21 wire, it is found that the coil can work continuously with an input current of 3A. However, the torque produced is small relatively because of the less number of turns. Using AWG24 wire will have more turns and produce more heat. By using a simple cooling system, AWG24 wire can work stably in the spherical actuator.

4.3.2.3 Winding Geometry

In formulating the torque model, the conical coil is used. However, this type of coils is difficult to fabricate massively in practice. Therefore, several other types of winding geometries like straight coil, stepped coil and trapezoid coil, are introduced as alternative options. Large sectional area of coils allows more wire turns, which helps in achieving large torque output. Sectional areas of these type of coil frames are shown in Fig. 4.17. According to Fig. 4.17(a), the sectional winding area of the straight coil is computed as

$$A_1 = lD_1 - ld. \tag{4.14}$$

Similarly, the sectional areas of the stepped coil and the trapezoid coil are

$$A_2 = l_1D_1 + (l - l_1)D_3 - l_2(D_2 - d) - ld, \tag{4.15}$$

$$A_3 = \frac{l(D_1 + D_2)}{2} - ld. \tag{4.16}$$

In order to show how much the stepped and trapezoid coils can increase the winding turns, let

$$D_2 = 2D_1, \tag{4.17}$$

$$D_3 = \frac{3}{2}D1, \tag{4.18}$$

$$l = 2l_1, \tag{4.19}$$

Using Eqns. (4.17)-(4.19) and ignoring the terms of ld and $l_2(D_2 - d)$, Eqns. (4.14)-(4.16) become

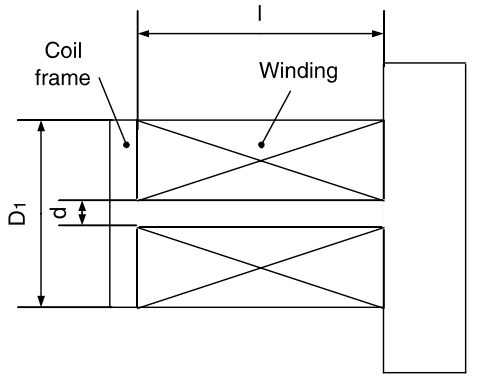

(a) Straight coil

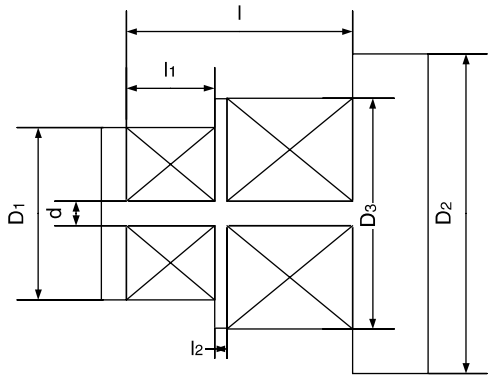

(b) Stepped coil

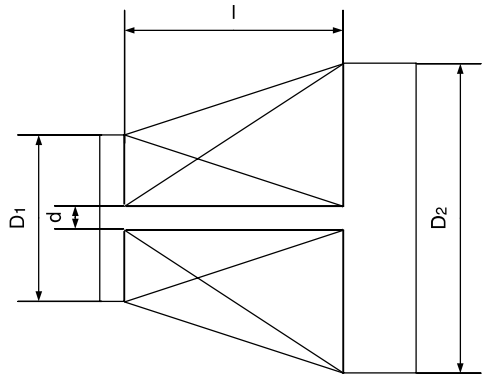

(c) Trapezoid coil

Fig. 4.17: Section view of different coil frames and coil geometry

$$A_1 = 2D_1 l_1, \tag{4.20}$$

$$A_2 = \frac{5}{2} D_1 l_1, \tag{4.21}$$

$$A_3 = 3D_1 l_1, \tag{4.22}$$

It can be seen that, compared to the straight coil, the stepped coil can increase the winding area by 25%, while the trapezoid coil can increase it by 50%, which is preferable for large torque generation. However, special winding approaches are necessary to be considered for the trapezoid coil to prevent from loosing wires. By contrast, the stepped coil and straight coil are relatively easy to be wound. Selection of the coil frame type could depend on specific requirements.

4.3.3 Material of Coil Frame

The material of the coil frame used is important as it might generate eddy current under the action of the PM-pole rotor. If the size of the coil frame, especially the inner core angle ζ_0, is large, nonmetal material such as Delrin or laminated metal material is favorable for the coil frame because there is no or little eddy current produced. However, if angle ζ_0 is very small, the eddy current produced in the coil frame can be neglected. In this case, metal material such as aluminium can be chosen as the coil frame material.

4.4 Stator

The primary function of the spherical-shell-like stator is to house air-core coils. As shown in Fig. 4.18, twenty-four circumferential holes are drilled through the stator shell and arranged in two layers symmetrically about the stator equator. Coils will be mounted through these holes and pointed to the center of the stator. The threads in the holes allow coil frames to be screwed in and out for adjusting the radial position of coils. The assembling slot is to facilitate the operation of tools such as pliers.

In the assembly of the spherical actuator, it is required that the rotor is concentric with the spherical-shell-like stator. Two cylindrical holes separated 90° apart are drilled at the equator plane of the stator as shown in Fig. 4.19. Likewise, two holes that are separated 90° apart and pointed to the rotor center are drilled at the equator plane of the rotor. Two centering pins can be inserted through the holes on the stator shell to the holes on the rotor. In this way, the concentricity of the rotor and the stator can be maintained. The stator can also be used for hosting optical/Hall effect sensors to detect the rotor orientation for motion control of the spherical actuator.

The stator is made of aluminum due to its low cost and ease of fabrication. The inner radius of the stator (95mm) is much larger than that of the rotor (46.5mm) due to the following facts.

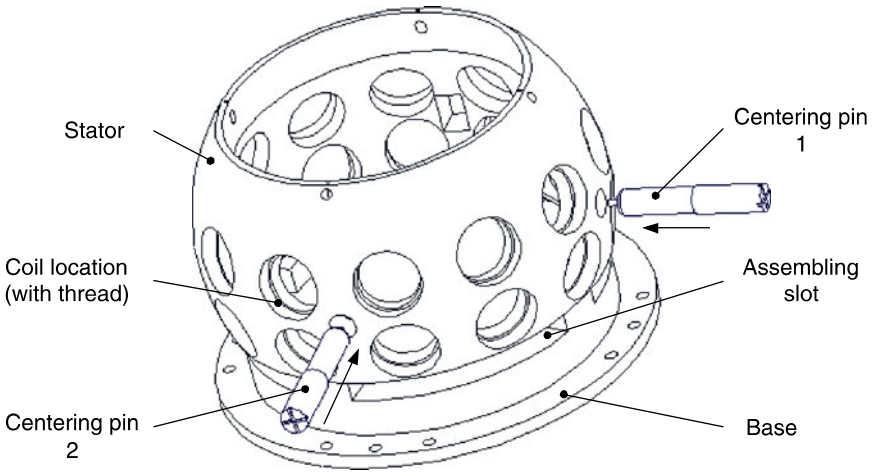

Fig. 4.18: Stator

- The eddy current induced on the aluminum stator due to PM poles on the rotor may affect the rotor motion, large space between the rotor and the stator can reduce it significantly.
- Large space between the rotor and the stator facilitates the flux density measurement inside the actuator and heat dissipation.

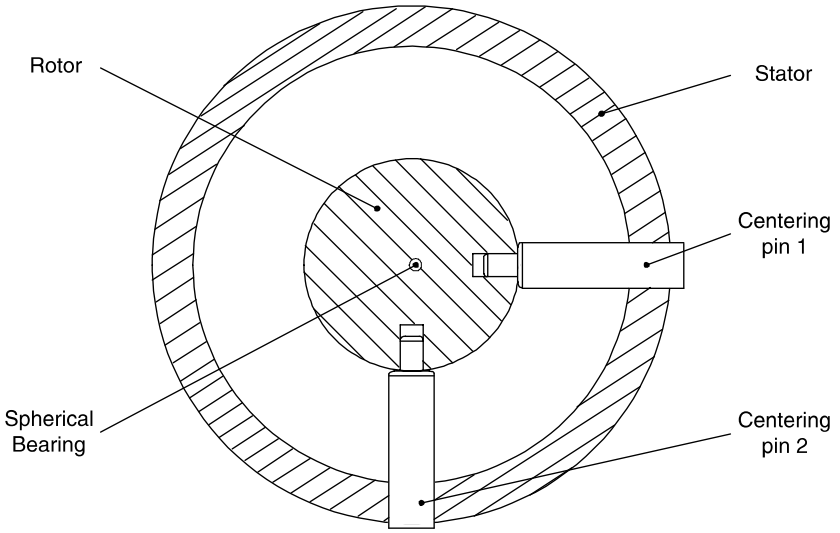

Fig. 4.19: Positions of centering pins (section view on the equator plane)

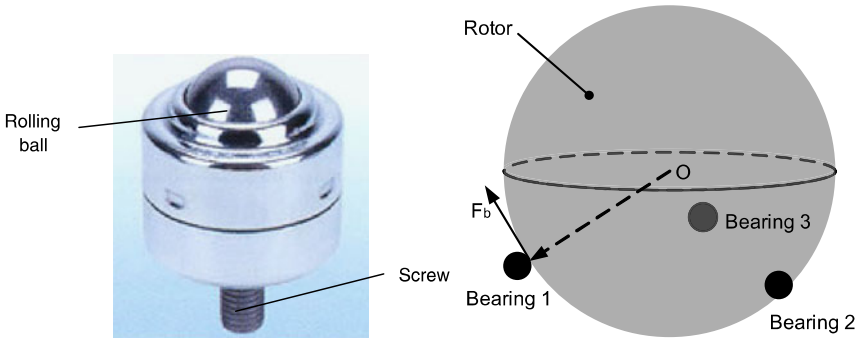

(a) Transfer bearing [11] (b) Rotor support

Fig. 4.20: Support spherical rotor with transfer bearings

For industrial products, the stator can be made from nonmetal material such as Delrin or laminated metal materials so that stator size can be reduced about 50%. Laminated ferromagnetic material not only reduces the eddy current significantly, but also improves the efficiency of the spherical actuator by "converging" the magnetic flux and reducing the magnetic energy loss.

4.5 Spherical Bearing

In order to secure the rotor position in the spherical actuator, a supporting mechanism is necessary. In the spherical actuator developed by Wang *et al*. [4, 5], the spherical rotor is housed within the spherical stator directly. Although a low friction coating was made on the stator inner surface, the sliding friction between the rotor and the stator may cause unfavorable effect on the rotor motion. In some spherical motors [6, 7], transfer bearings or analog are used to support the rotor. A typical transfer bearing is shown in Fig. 4.20(a). This bearing consists of a rolling ball on the top, which can create a rolling motion with respect to the contact surface. The screw on the other end can fix the bearing on the stator for adjusting its position. As indicated in Fig. 4.20(b), to support a spherical rotor stably, at least three transfer bearings are necessary. The rolling motion of these transfer bearings produces rolling friction lower than the sliding friction. Nevertheless, the torque of friction from the transfer bearing relative to the rotor center is large due to the rotor radius. The non-negligible resultant frictional torque generated by three transfer bearings may suppress the system efficiency. The effect of frictional torque on the rotor of the VRSM has been analyzed by Zhou [8]. To effectively reduce the friction, an air bearing system has been proposed by Lee *et al* [9, 10]. Because the rotor floats on air, the friction can be played down significantly. However, the requirement of the air source complicates the application of this bearing system.

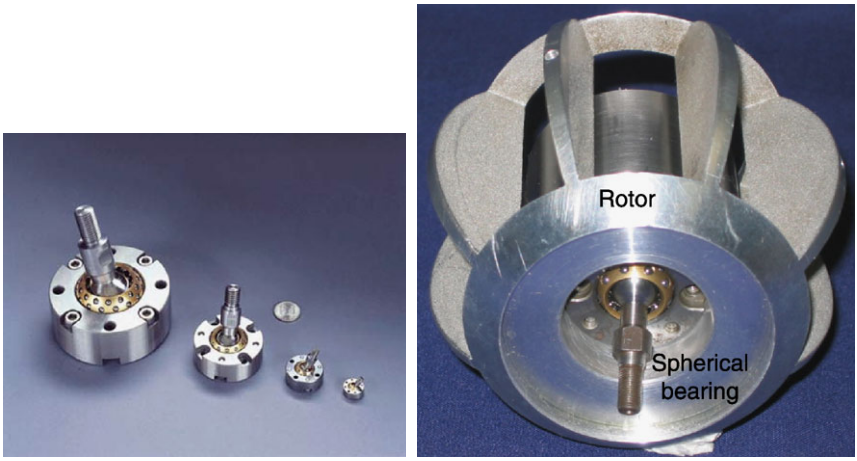

(a) Spherical bearing [12] (b) Spherical bearing at the rotor center

Fig. 4.21: Implementation of spherical bearing on the rotor

In our spherical actuator, a spherical bearing (Fig. 4.21(a)) [12] is employed to support the rotor housed in the stator. This spherical bearing can achieve a smooth 3-DOF rotational motion. The tilting motion range of this bearing is up to $\pm 35^{\circ}$. It can be assembled at the rotor center as shown in Fig. 4.21(b). Because the friction produced by this spherical bearing is very small and the moment arm of the frictional force is less than 6mm, the frictional torque produced by the spherical bearing is negligible. Compared with the air bearing, the implementation of this spherical bearing is also easy.

4.6 Summary

In order to achieve high torque output of the PM spherical actuator, the design of two major force/torque generating elements, PM-pole rotor and coil has been the main concerns in this chapter. Due to the parametrization of PM poles and coils, the relationship between these parameters and torque output can be described. According to these relationship, suitable values of the parameters are determined to achieve high torque output of the actuator. In addition to the analysis of geometric dimensions of PM and coil poles, several winding techniques are proposed to increase the number of coil turns and the torque output. A spherical bearing is employed to reduce the frictional torque exerted on the rotor. Based on the theoretical analysis, a research prototype is fabricated. This prototype will be used for experimental measurement on magnetic field and torque output to verify the theoretical models.

References

1. Mathematical group (1984) Mathematical Handbook. High Educational Press, China, 1984.
2. Miner G F (1996) Lines and Electromagnetic Fields for Engineers. Oxford University Press, USA, 1996.
3. Integrated Publishing (2005) Properties of copper and aluminum. In: The website on properties of copper and aluminum. Available online: http://www.tpub.com/content/neets/14176/css/14176_25.htm. Cited May 2005
4. Wang J, Jewell G W, Howe D et al (1997) Modelling of a novel spherical permanent magnet actuator. Proceedings of 1997 IEEE International Conference on Robotics and Automation, Hague, Netherlands, vol. 145, no. 1:1190–1195, Albuquerque, New Mexico, USA, April 1997.
5. Wang J, Wang W, Jewell G W, Howe D et al (1998) A novel spherical actuator with three degrees-of-freedom. IEEE Transactions on Magnetics, vol. 34, no. 4:2078–2080, July 1998.
6. Chirikjian G S, Stein D et al (1999) Kinematic design and commutation of a spherical stepper motor. IEEE/ASME Transactions on Mechatronics, vol. 4, no. 4:342–353, December 1999.
7. Lee K M, Sosseh R A et al (2002) Effects of fixture dynamics on back-stepping control of a VR spherical motor. Proceedings of the 7^{th} International Conference on Robotics, Automation and Computer Vision, vol. 145, no. 1:1–6, Singapore, 2–5 December 2002.
8. Zhou Z (1995) Real-Time Control and Characterization of a Variable Reluctance Spherical Motor. Thesis of Georgia Institute of Technology, GA, USA, May 1995.
9. Lee K M, Ezenekwe D E, He T et al (2003) Design and control of a spherical air-bearing system for multi-d.o.f ball-joint-like actuators. Mechatronics, vol. 13:175–194, 2003.
10. Ezenekwe D E (1998) Design Methodology of an Air Bearing System for Multi-DOF Spherical Actuator Motion Control Applications. Thesis of Georgia Institute of Technology, GA, USA, December 1998.
11. Yuhuan Appear Ball Transfer Units Factory of Zhejiang (2005) Specification of transfer bearings. In: The website of Ball Transfer Units. Available online: http://www.balltransfergroup.com. Cited May 2005
12. Hephaist Seiko Co., Ltd. (2005) Specification of spherical bearings. In: The website of Hephaist Seiko Co., Ltd. Available online: http://www.hephaist.co.jp/e/pro/ball.html. Cited May 2005

Chapter 5
Experimental Investigation

In this chapter, the experimental investigation is conducted on the prototype of the PM spherical actuator to verify the analytical magnetic field model and torque model proposed in Chapter 2 and Chapter 3. The experimental result also facilitate the visualization of the magnetic field distribution and the torque variation of the actuator. As shown in Fig. 5.1, the experimental investigation of the PM spherical actuator consists of two major tasks: measurement of magnetic field distribution and torque output variation.

This chapter begins with description of magnetic field measurement procedure of the PM-pole rotor, and the corresponding data processing and analysis. The force/torque measurement is carried out on the PM spherical actuator and compared with the theoretical torque model. The experimental results confirm the proposed magnetic field model and torque model for further control study of the actuator.

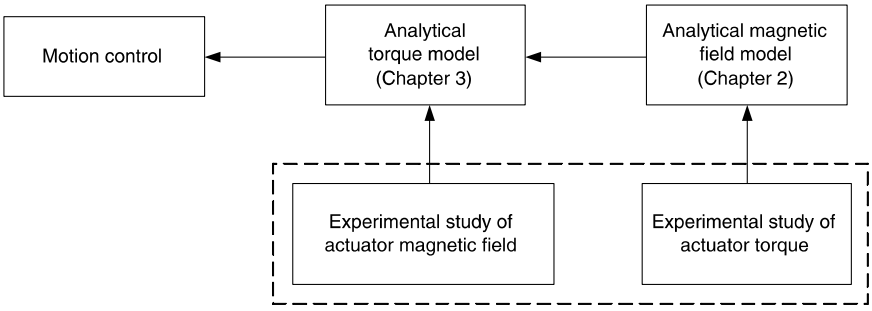

Fig. 5.1: Experimental investigation on PM spherical actuator

L. Yan et al., *Design, Modeling and Experiments of 3-DOF Electromagnetic Spherical Actuators*, Mechanisms and Machine Science 4,
DOI 10.1007/978-94-007-1646-9_5, © Springer Science+Business Media B.V. 2011

5.1 Measurement of PM Rotor Magnetic Field

Experimental measurement on the magnetic flux density can be done readily in some special cases. For example, the magnetic flux distribution of rectangular cross-section electromagnets proposed by Mintchev *et al*. [2, 3] is relatively simple. As illustrated in Fig. 5.2(a), a magnetic field is excited by a current-carrying coil. The magnetic flux lines form a closed loop through ferromagnetic material such as soft iron disrupted by a narrow airgap. Because of the small size of the airgap, the fringing flux can be ignored and the flux lines can be regarded as evenly distributed within the airgap volume. In other words, the magnetic flux in the airgap forms a 1D field. In this case, the flux density data can be taken easily at points inside the airgap by using the single-axis Hall probe that has a tip as thin as 0.5mm (Fig. 5.2(b)). The rigorous requirement on the airgap in the magnetic flux loop limits the application of this measurement method. Furlani [4] simplified the flux density measurement of a PM motor by sampling the data in a characteristic point within the workspace. However, the data at this point can only reflect the variation of the magnetic field roughly. It is no longer applicable for precise measurement. As an improvement, Enokizono *et al*. [5] have proposed a method to measure the flux density on a 2D plane of a single-axis motor accurately. Due to the axial symmetric structure of this motor, the magnetic field on one plane perpendicular to the axis suffices to represent the entire magnetic field. However, this method is not suitable for the 3D flux density measurement of magnetic elements with complex structures. In recent years, 3-DOF electromagnetic spherical actuators have been developed by researchers to overcome the drawbacks of conventional spherical motion mechanisms realized by

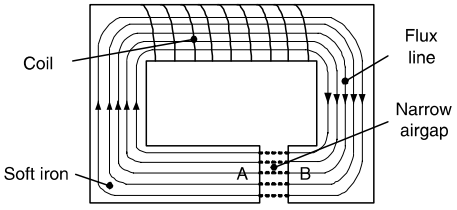

(a) Narrow airgap

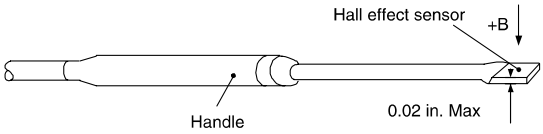

(b) Single-axis probe(MFT-2903-VH) [1]

Fig. 5.2: Flux density measurement in a narrow airgap

several single-axis actuators. FEM approach has been used to simulate the variation of the flux density [6, 7]. However, so far complete experimental measurement on the three components of the flux density distribution in 3D space of these motors has not been reported in the literature. The challenge for experimental study of the magnetic field of the spherical actuator lies in the complexity of measurement for all three components of the flux density varying in the 3D space around the rotor.

In our study, an apparatus for the 3D flux density measurement of the PM rotor is developed. By using this apparatus, the complete experimental measurement of the magnetic field distribution of the PM-pole rotor is carried out in 3D space. The measured data can be nondimensionalized and normalized to eliminate the effect of the specific rotor dimensions. The result can be referred by other similar rotor designs by multiplying several pre-defined constants. Furthermore, these data can be visualized and compared with the analytical result from the magnetic field model derived previously.

5.1.1 Flux Density Measurement Apparatus

The flux measurement apparatus developed for this project can move a magnetic field measuring probe (Hall probe) to any 3D point of concern and take the flux density data at the point. It includes a three-axis Hall probe, a Gauss meter, a three-axis translational stage, a personal computer (PC) and a single-axis servo motor.

5.1.1.1 Three-axis Hall Probe

The flux density is a 3×1 vector. A complete measurement of the magnetic field needs to acquire all three components of the flux density at any measuring point surrounding the rotor. A three-axis Hall probe (Lake Shore MMZ-2502-UH [8]) as shown in Fig. 5.3 is employed for this task with specifications listed in Table 5.1. According to the theoretical analysis, the maximum flux density of the PM poles on the rotor surface is about $\pm$6kG which is within the measuring range of the probe,

Fig. 5.3: Three-axis Hall probe (Lake Shore MMZ-2502-UH) [1]

±30kG. With a resolution of 0.1G and the operating temperature range from 10°C to 40°C, this Hall probe meets the measurement requirement in most cases.

Table 5.1: Specifications of a three-axis Hall probe [8]

Model	LakeShore MMZ-2502-UH (three-axis)
Type	HSE-1 (High sensitivity probe)
Stem material	Aluminum
Measuring range	±30kG
Measuring resolution	0.1G
Operating temperature	10°C to 40°C

5.1.1.2 Setup of Measurement Apparatus

Figure 5.4 shows the setup of the flux density measurement apparatus with specifications listed in Table 5.2. The Hall probe is mounted on a high precision three-axis translational motion stage (NSK XY-HRS 040-H201 [9]) with a motion resolution of 0.01mm, so that it can pinpoint to any location near the rotor. This probe is connected to a Gauss meter that can display the measured magnetic flux density in three

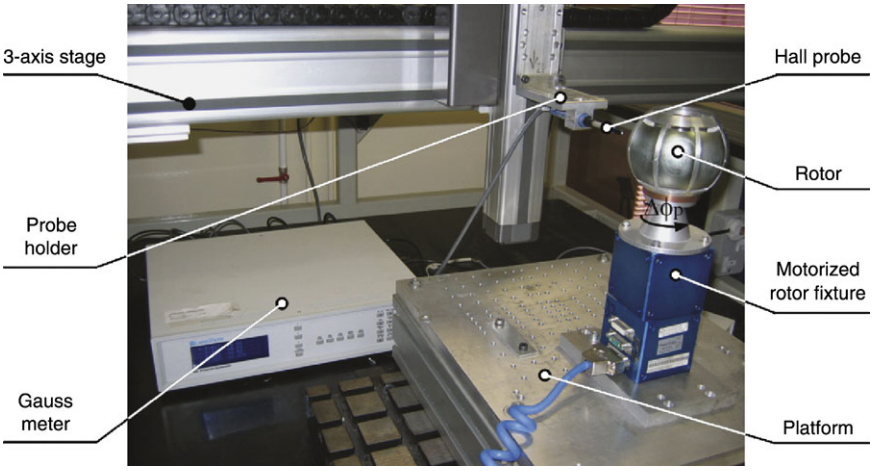

Fig. 5.4: Apparatus setup

components. The Gauss meter is linked to a PC through a data acquisition (DAQ) card. The measured flux density then can be automatically stored in the PC. The rotor is mounted on a motorized fixture that can spin along the rotor axis in 360°. Thus, the Hall probe can measure the magnetic flux density in the longitudinal direction of the rotor by simply rotating the rotor using the fixture without re-orienting the Hall probe.

Table 5.2: Specifications of the magnetic field measurement apparatus

Gauss meter	Model	LakeShore 460 [8]
	Number of Channel	3 Channels
	Update rate	18 readings/s
Platform	Size	340x440mm
Three-axis translational stage	Model	NSK XY-HRS 040-H201 [9]
	Resolution	0.01mm
	Maximum velocity	1200mm/s
Motorized fixture	Model	PowerCube PDU 070 [10]
	Resolution	6 Arcsec
	Maximum angular velocity	238°/s

5.1.1.3 Measurement Coordinates

To facilitate measurement of the magnetic field of the PM-pole rotor, the measurement coordinates r_p, ϕ_p and θ_p are introduced as illustrated in Fig. 5.5. The origin of the measurement coordinate system (r_p, θ_p, ϕ_p) coincides with that of the rotor coordinate system (r, θ, ϕ). The latitudinal angle θ starts from the z-axis whereas θ_p starts from the equatorial plane of the rotor; the longitudinal angle ϕ coincides with ϕ_p; the radial coordinates r_p and r are identical.

5.1.1.4 Measurement Process

The Hall probe moves along a pre-determined path illustrated in Fig. 5.6 and takes measurement of flux density at sampling points along the path. As the rotor structure is symmetric about the equatorial plane, the measurement is only carried out for the upper hemisphere. The measuring path starts from a point along the center axis of a PM pole and very close to the rotor surface. The measuring path is kept along a vertical plane called a measuring plane. The probe moves along an arc upwards on the plane while keeping at a constant normal distance d_a to the rotor surface. The neighboring sampling points keep a constant angle of $\Delta\theta_p$ with respect to the rotor center as shown in Fig. 5.6. After the probe completes an arc of $\theta_p = 25°$, the probe

offsets a distance of Δr_p radially and then carries out measurement along the subsequent arc path. This measuring process is repeated with increasing radial distance r_p until the flux density is significantly small. For our measurement, the maximum motion in the r_p-direction is 30mm. This radial distance is beyond the possible position of the stator coil. Because of the constant angular sampling pattern, the measuring points are sparsely located when the radius r_p increases. It is coincident with the fact that the gradient of the flux density decreases with increasing r_p. Therefore,

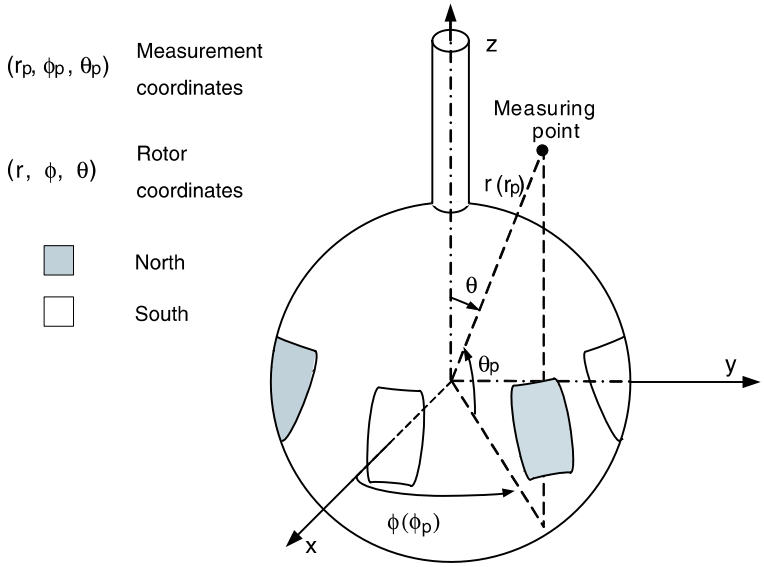

Fig. 5.5: Definition of measurement coordinate system for Hall probe

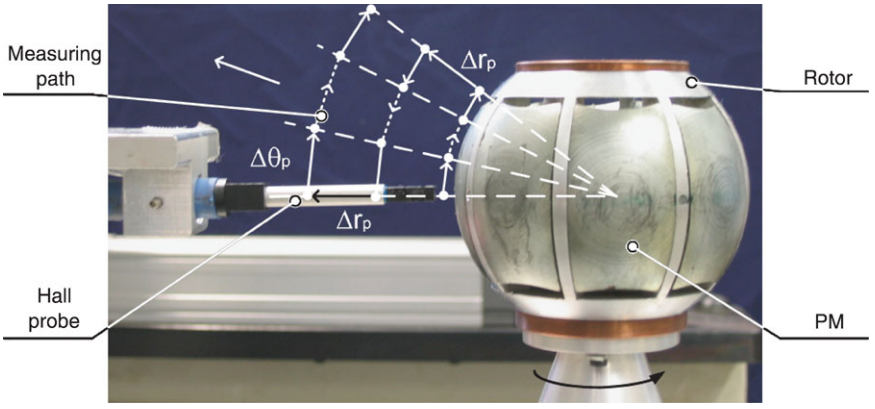

Fig. 5.6: Magnetic flux density measurement of the PM-pole rotor

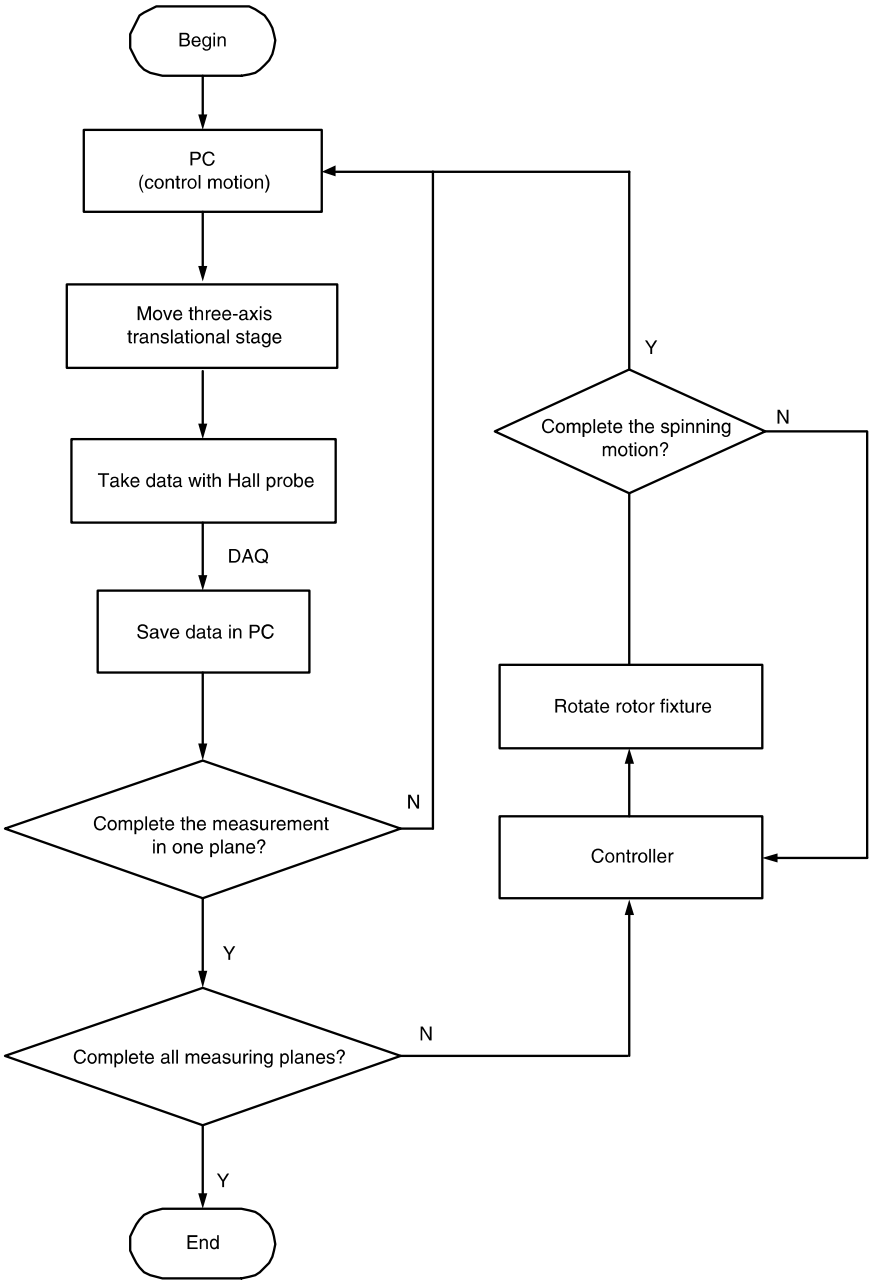

Fig. 5.7: Magnetic flux density measurement process

Fig. 5.8: Calibration of alignment

this sampling method requires less sampling points than that of the equal distance sampling method.

After completing the measurement task in one measuring plane, the PC sends commands to the controller of the rotor fixture to turn the rotor with an angle of $\Delta\phi_p$, while the probe keeps stationary. The Hall probe is then positioned in a new measuring plane with respect to the rotor and the same data acquisition procedure is repeated. The entire process of positioning the probe, taking measurement and turning the rotor can be fully automated as shown in Fig. 5.7.

By using this apparatus, the flux density around the rotor has been measured several times. It was found that the maximum difference between measurements is about 50G or 1% of the maximum flux density. This repeatability could be acceptable.

5.1.1.5 Calibration of Spinning Center of Rotor

In the magnetic field measurement apparatus, the rotor of the PM spherical actuator is mounted on a single-axis servo motor (PowerCube PR070 [11]). This single-axis servo motor rotates the rotor in the ϕ_p-direction. Thus, alignment of the axes of the servo motor and the rotor is important for accurate magnetic field measurement. In order to ensure the alignment of the two axes, a calibration of the eccentricity of the rotor axis is carried out by using the apparatus shown in Fig. 5.8.

The servo motor along with the rotor of the spherical actuator is first secured on a stage. This single-axis servo motor can attain a resolution as high as 6 arcsec. A displacement sensor probe (Probe 5313180 [10]) is put in contact with the rotor surface gently. When the rotor rotates by the single-axis servo motor, the probe tip detects

the variation of the rotor surface and transmits the variation information to the Millitron (Mahr Millitron-1240 [12]). The Millitron has a resolution of 10μm and a measurement range of $\pm 300\mu$m. With distance variation data, the rotor position on the servo motor is adjusted to minimize the distance variation or the misalignment of the servo motor axis and the rotor axis. In this experiment, the distance variation is calibrated below 50μm to minimize its effect on the magnetic field measurement.

5.1.2 Flux Density Data Processing

Nondimensionalization and normalization techniques are used to process the measured magnetic flux density from the Hall probe. In this way, the experimental data can be used as a reference for similar spherical actuator designs without referring to specific rotor dimensions.

5.1.2.1 Transformation of Coordinates

When the tip of the Hall probe reaches a measuring point as shown in Fig. 5.9, three components of the flux density, B_{X_h}, B_{Y_h} and B_{Z_h} are obtained based on the coordinates of the Hall probe, X_h, Y_h and Z_h. The Hall probe is always kept in horizontal direction. As the magnetic field model of the PM rotor is expressed in the spherical coordinates (r, θ, ϕ) on the rotor (The Hall probe does not align with r.), it is necessary to convert these data from the sensor coordinates to the spherical coordinates on the rotor. According to Fig. 5.9, the following relation can be derived:

$$\begin{aligned} B_{Ir} &= -B_{Y_h}\cos\theta + B_{Z_h}\sin\theta, \\ B_{I\theta} &= B_{Y_h}\sin\theta + B_{Z_h}\cos\theta, \\ B_{I\phi} &= B_{X_h}. \end{aligned} \tag{5.1}$$

Table 5.3 presents some sampling data converted from sensor coordinates to spherical coordinates. Because $B_{I\theta}$ and $B_{I\phi}$ do not contribute to the actuator torque in spherical configuration, and only the radial component B_{Ir} will do, the following discussion is focused on B_{Ir} only.

5.1.2.2 Nondimensionalization and Normalization of Experimental Result

Nondimensionalization is the partial or full removal of units from a mathematical equation by a suitable substitution of variables. It is generally used in sociological, economic or mechanical areas to evaluate the weight of different inputs, such as the oil gap in the hydrodynamic lubrication system [13, 14, 15]. By using the technique of nondimensionalization, the behavior of the system can be analyzed regardless of the units used to measure the variables. One notable example is the Reynolds

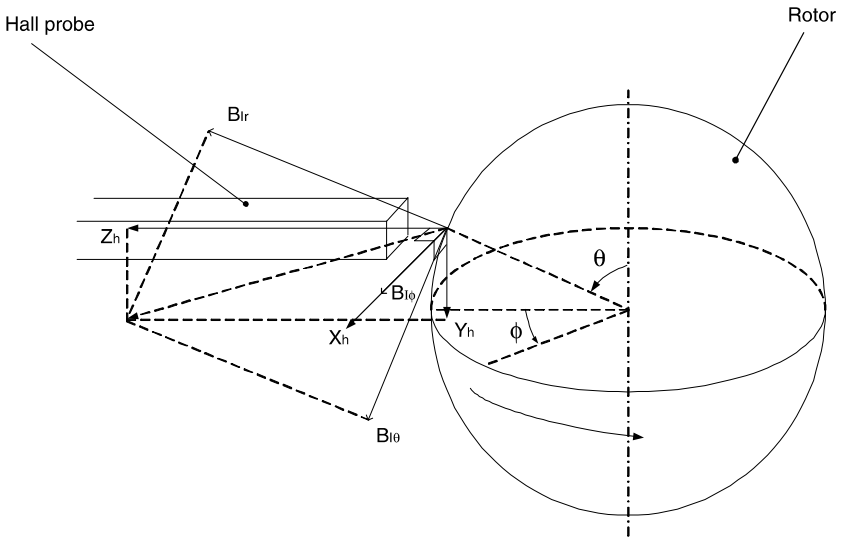

Fig. 5.9: Transformation from Hall-probe coordinates to spherical coordinates

number frequently used in fluid mechanics that is the ratio of inertial force and the viscous force. In addition, the number of variables in the flux density function can be reduced.

After nondimensionalization of experimental data of the magnetic flux density measurement, the flux density becomes a function of dimensionless arguments. Normalization of the nondimensionalized data is then followed. Normalized data set can be used as a benchmark result to be used by other spherical actuators with similar rotor design.

Nondimensionalization of the radial parameters in magnetic field model:

The radial parameter r in the magnetic field model can be scaled by rotor radius R_r. Thus Eqn. (2.52) and the related constant d_4 can be reorganized as

$$B_{Ir} = \frac{15\mu_0 M_0 acd_4^{'}}{8\pi}\sqrt{\frac{35}{2}}(\frac{R_r}{r})^6 \sin^4\theta\cos 4\phi, \tag{5.2}$$

where

Table 5.3: Magnetic flux density data conversion from sensor coordinates to spherical coordinates ($\phi_p = 0$, $d_a = 0.5$mm)

θ_p (°)	B_{X_h} (kG)	B_{Y_h} (kG)	B_{Z_h} (kG)	B_r (kG)	B_θ (kG)	B_ϕ (kG)
0	0.7638	0.5037	-6.2135	-6.2135	0.5037	0.7638
1	1.0086	0.4979	-6.1921	-6.1998	0.3898	1.0086
2	1.2179	0.4800	-6.1845	-6.1975	0.2639	1.2179
3	1.3691	0.4703	-6.1746	-6.1908	0.1465	1.3691
4	1.5860	0.4427	-6.1028	-6.1188	0.0159	1.5860
5	1.7680	0.4382	-6.0478	-6.0630	-0.0906	1.7680
6	1.9618	0.3867	-5.9676	-5.9753	-0.2392	1.9618
7	2.1247	0.3879	-5.8748	-5.8783	-0.3309	2.1247
8	2.2865	0.3683	-5.8010	-5.7958	-0.4426	2.2865
9	2.4550	0.3485	-5.6722	-5.6569	-0.5431	2.4550
10	2.6562	0.3164	-5.5846	-5.5547	-0.6582	2.6562
11	2.8175	0.2670	-5.4552	-5.4059	-0.7788	2.8175
12	2.9740	0.2550	-5.2905	-5.2279	-0.8505	2.9740
13	3.1255	0.2470	-5.1099	-5.0345	-0.9088	3.1255
14	3.2383	0.2226	-4.9629	-4.8693	-0.9846	3.2383
15	3.4186	0.1903	-4.7742	-4.6608	-1.0518	3.4186
16	3.6008	0.1677	-4.5640	-4.4334	-1.0968	3.6008
17	3.7007	0.1658	-4.3939	-4.2504	-1.1261	3.7007
18	3.8790	0.1472	-4.1720	-4.0133	-1.1492	3.8790
19	4.0733	0.1103	-3.9549	-3.7753	-1.1833	4.0733
20	4.2697	0.1033	-3.7040	-3.5160	-1.1698	4.2697
21	4.4738	0.0193	-3.4245	-3.2040	-1.2092	4.4738
22	4.7021	0.0135	-3.1232	-2.9008	-1.1575	4.7021
23	4.9161	0.0099	-2.7956	-2.5772	-1.0832	4.9161
24	5.2382	0.0034	-2.3262	-2.1265	-0.9430	5.2382
25	5.6152	-0.0090	-1.7727	-1.6028	-0.7573	5.6152

$$d_4^{'} = -d_4^{\top'}/d_4^{\perp'}, \tag{5.3}$$

$$\begin{aligned} d_4^{\top'} &= d_4^{\top}/R_r^6 \\ &= 1 + \frac{9\mu_m R_b^6 R_r^3}{4(\mu_r-\mu_m)(R_b^9 - (4\mu_r+5\mu_m)R_r^9} \\ &= 1 + \frac{9\mu_m}{4(\mu_r-\mu_m)(\frac{R_b}{R_r})^3 - (4\mu_r+5\mu_m)(\frac{R_r}{R_b})^6}, \end{aligned} \tag{5.4}$$

$$\begin{aligned} d_4^{\perp'} &= d_4^{\perp} \\ &= 5(\mu_m-1) + \frac{9\mu_m(4\mu_r+5\mu_m)R_r^9}{4(\mu_r-\mu_m)R_b^9 - (4\mu_r+5\mu_m)R_r^9} \\ &= 5(\mu_m-1) + \frac{9\mu_m(4\mu_r+5\mu_m)}{4(\mu_r-\mu_m)(\frac{R_b}{R_r})^9 - (4\mu_r+5\mu_m)}. \end{aligned} \tag{5.5}$$

Let $\nu_1 = R_r/r$, $\nu_2 = R_b/R_r$, Eqns. (5.2)-(5.5) can be rewritten as

$$B_{Ir} = \frac{15\mu_0 M_0 a c d_4^{'}}{8\pi}\sqrt{\frac{35}{2}}\nu_1^6 \sin^4\theta\cos 4\phi, \tag{5.6}$$

where

$$d_4^{'} = -d_4^{\top'}/d_4^{\perp'}, \tag{5.7}$$

$$d_4^{\top'} = 1 + \frac{9\mu_m}{4(\mu_r-\mu_m)\nu_2^3 - (4\mu_r+5\mu_m)(\frac{1}{\nu_2})^6}, \tag{5.8}$$

$$d_4^{\perp'} = 5(\mu_m - 1) + \frac{9\mu_m(4\mu_r+5\mu_m)}{4(\mu_r-\mu_m)\nu_2^9 - (4\mu_r+5\mu_m)}. \tag{5.9}$$

Both ν_1 and ν_2 are dimensionless coefficients varying between 0 and 1. Therefore, computing the flux density based on the dimensional parameters R_b, R_r and r becomes computing the flux density from dimensionless parameters ν_1 and ν_2.

Normalization of measured flux density:

The normalization technique is applied to the measured magnetic field. For convenience, denote radial component of the measured flux density under rotor coordinates with coordinate transformation from the probe coordinates, Eqn. (5.1) as B_{Ir}^e. The process of normalization is as follows.

Step One: The relationship between ν_2 and $d_4^{'}$ is plotted in Fig. 5.10 based on Eqns. (5.7)-(5.9). When $0 < \nu_2 < 0.5$, the value of $d_4^{'}$ does not change much, but always kept at 0.1087. It means that the magnetized material at the core of the rotor does not help much to improve the flux density of the rotor. Between $0.5 < \nu_2 < 0.7$, $d_4^{'}$ decreases slightly. After $\nu_2 = 0.7$, $d_4^{'}$ decreases drastically, which indicates that when R_b is close to R_r or when the thickness of the PM pole is very small, the flux density of the rotor drops quickly. Recall the design parameters of the PM-pole rotor. It is known that for this spherical actuator, $\nu_2 = 23/46.5 < 0.5$, and $d_4^{'}$ maintains the maximum value. Hence, the maximum value of $d_4^{'}$ is chosen as the normalization constant for the measured data. In other words, the experimental result on the rotor can be normalized by $B_{Ir}^e/0.1087$ or $9.2B_{Ir}^e$.

Step Two: Inspection of Eqn. (5.6) shows that the term $\mu_0 M_0 a c$ is related to the parameters of this particular rotor design. In order to produce useful benchmark data, the measured result needs to be normalized further by $B_{Ir}^e/(\mu_0 M_0 a c)$. Note that this is also a nondimensionalization process because all variables are dimensionless.

Eventually, the dimensionless flux density, denoted as B_{Ir}^N, will be related to the measured flux density B_{Ir}^e by

$$B_{Ir}^N = \frac{9.2B_{Ir}^e}{\mu_0 M_0 a c}. \tag{5.10}$$

The dimensionless B_{Ir}^N is a function of dimensionless variables ν_1, ϕ and θ.

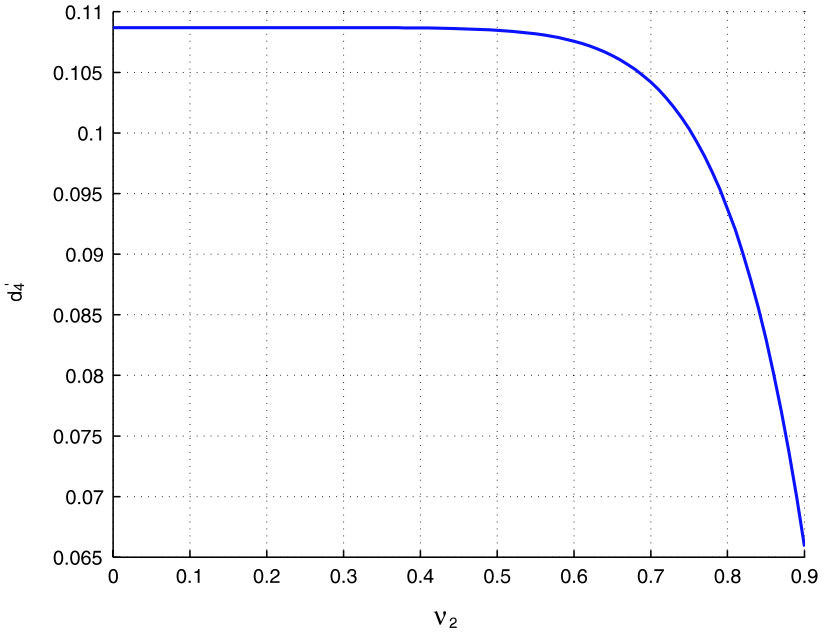

Fig. 5.10: Dimensionless variables ν_2 vs. $d_4^{'}$

5.1.2.3 Computation of Magnetic Flux Density from B_{Ir}^N

After the normalized data set B_{Ir}^N is established, it is necessary to consider how to obtain the magnetic flux density of another PM-pole rotor with similar structure from this data set.

To distinguish from the proposed spherical actuator design, a generic spherical rotor can be specified with parameters denoted as M_0^g, a^g, c^g and $d_4^{'g}$, where a^g can be obtained from α^g with Eqn. (2.23), c^g from β^g with Eqn. (2.24) and $d_4^{'g}$ from R_b^g and R_r^g with Eqn. (5.3). The magnetic flux density of the new spherical rotor can be computed based on the normalized measurement data as

$$B_{Ir}^{New} = \mu_0 M_0^g a^g c^g d_4^{'g} B_{Ir}^N, \tag{5.11}$$

where B_{Ir}^{New} is the data for the new rotor.

5.1.3 Visualization and Analysis of Experimental Result

The flux density B_{Ir} is a function of the rotor coordinates (r, θ, ϕ) or the measurement coordinates (r_p, θ_p, ϕ_p) with suitable coordinate transformation. Visualizing the distribution of B_{Ir} in the coordinates is difficult because it becomes a 3D manifold in a 4D space. Hence, by fixing the value of one of the coordinates, B_{Ir} can be plotted or visualized as a 2D manifold in a 3D space. Logically, by fixing r_p, the flux density B_{Ir} can be plotted against θ_p and ϕ_p as a 2D surface.

5.1.3.1 Magnetic Flux Density B_{Ir} Variation with Respect to θ_p and ϕ_p

Let d_a be the normal distance from the measuring point to the rotor surface. Besides the angular parameters θ_p and ϕ_p, magnetic flux density B_{Ir} is a function of r_p (Eqn. (2.52)) which in turn can be replaced by the normal distance from measuring point to the rotor surface d_a as

$$r_p = d_a + R_r. \tag{5.12}$$

Comparisons between the measured result and the analytical model of B_{Ir} are summarized in Fig. 5.11 and 5.12. The experimental and analytical values of B_{Ir} at $d_a = 0.5$mm, $d_a = 2.5$, $d_a = 4.5$ and $d_a = 6.5$mm are presented in Fig. 5.11(a), 5.11(b), 5.12(a) and 5.12(b). The values of B_{Ir} decrease when d_a becomes large as the magnetic flux density reduced its strength away from the rotor. Along the equator of the rotor in the ϕ_p-direction, eight positive/negative ridges can be observed due to the eight alternately magnetized PM poles on the rotor equator. This variation can be clearly seen in 2D presentation of the flux density data. Figures 5.11(e), 5.11(f), 5.12(e) and 5.12(f) show the variation of B_{Ir} along the rotor equator at $\theta_p = 0$.

Differences between the experimental data and analytical model can be observed in Figure 5.11(c), 5.11(d), 5.12(c) and 5.12(d) for flux density at $d_a = 0.5$mm $d_a = 2.5$mm, $d_a = 4.5$mm and $d_a = 6.5$mm respectively. This difference of flux density modeling is mainly caused by the omission of high order harmonic terms in developing the scalar potential function of the magnetic field. The maximum difference between the experimental data and analytical result is about $400G$ or 7% of the actual measured data, which indicates that the accuracy of the proposed analytical magnetic field model is acceptable. With the inclusion of high order harmonics, the magnetic field model can be more accurate.

5.1.3.2 Magnetic Flux Density B_{Ir} with Respect to d_a

By fixing the angular parameters (θ_p, ϕ_p), the relationship between magnetic flux density B_{Ir} and d_a can be illustrated. Figure 5.13(a) and 5.13(b) present the change of B_{Ir} along the radial direction at $\theta_p = 0^\circ$, $\phi_p = 45^\circ$ and $\theta_p = 10^\circ$, $\phi_p = 35^\circ$. It

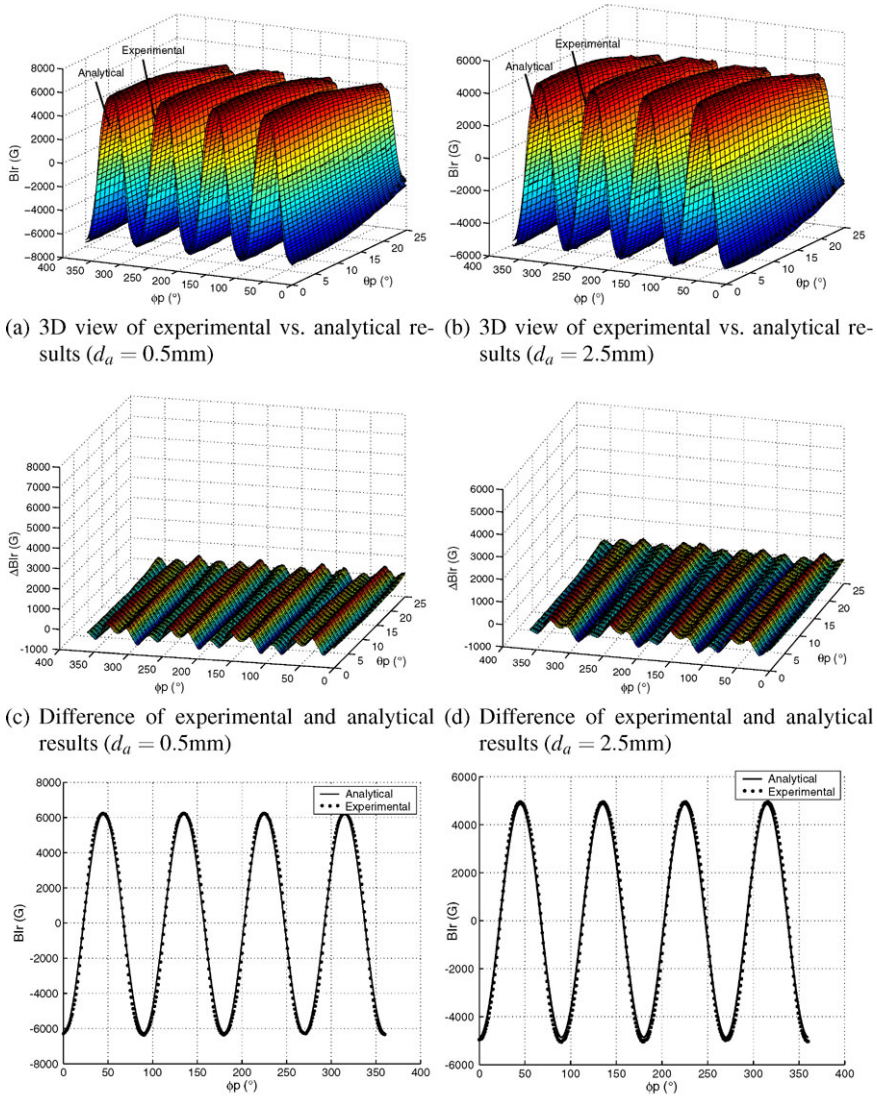

(a) 3D view of experimental vs. analytical results ($d_a = 0.5$mm)

(b) 3D view of experimental vs. analytical results ($d_a = 2.5$mm)

(c) Difference of experimental and analytical results ($d_a = 0.5$mm)

(d) Difference of experimental and analytical results ($d_a = 2.5$mm)

(e) 2D view of experimental vs. analytical results ($d_a = 0.5$mm, $\theta_p = 0$)

(f) 2D view of experimental vs. analytical results ($d_a = 2.5$mm, $\theta_p = 0$)

Fig. 5.11: Experimental and analytical values of magnetic flux density B_{Ir} ($d_a = 0.5$mm and 2.5mm)

can be seen that the analytical model also fits the experimental result well along the radial direction.

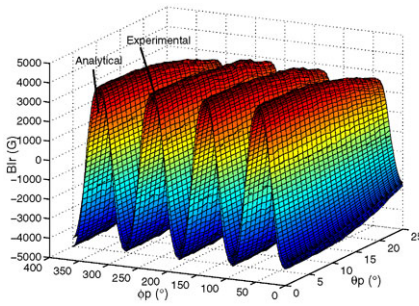

(a) 3D view of experimental vs. analytical results ($d_a = 4.5$mm)

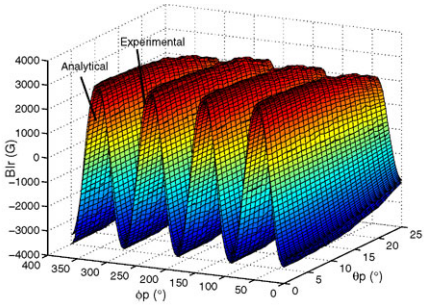

(b) 3D view of experimental vs. analytical results ($d_a = 6.5$mm)

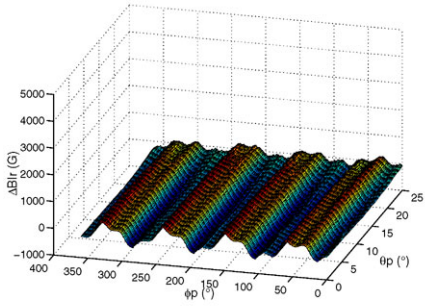

(c) Difference of experimental and analytical results ($d_a = 4.5$mm)

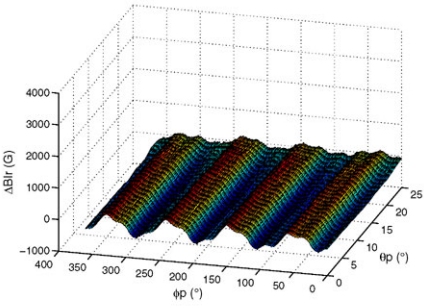

(d) Difference of experimental and analytical results ($d_a = 6.5$mm)

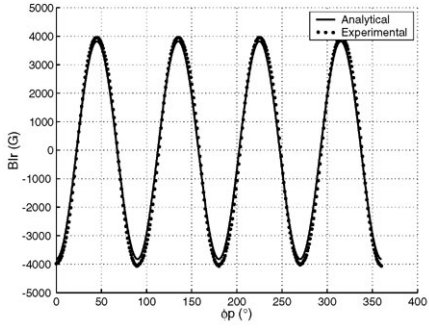

(e) 2D view of experimental vs. analytical results ($d_a = 4.5$mm, $\theta_p = 0$)

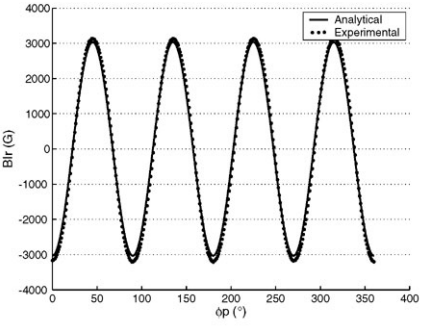

(f) 2D view of experimental vs. analytical results ($d_a = 6.5$mm, $\theta_p = 0$)

Fig. 5.12: Experimental and analytical values of magnetic flux density B_{Ir} ($d_a =$ 4.5mm and 6.5mm)

5.2 Measurement of Actuator Torque Output

To verify the analytical torque model, a series of experiments are conducted on the torque measurement of the spherical actuator.

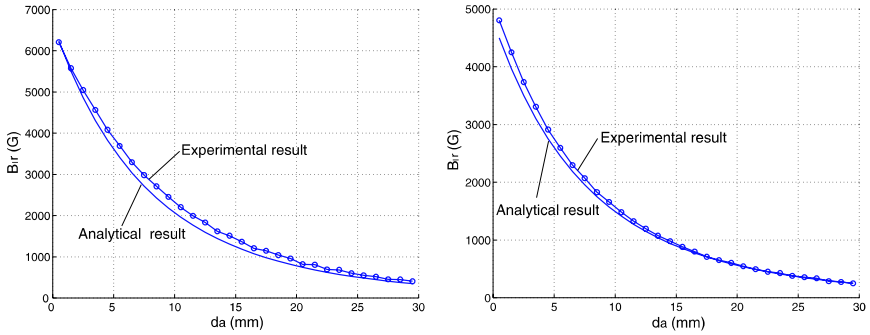

(a) $\theta_p = 0^\circ$, $\phi_p = 45^\circ$ (b) $\theta_p = 10^\circ$, $\phi_p = 35^\circ$

Fig. 5.13: Magnetic flux density B_{Ir} in radial direction

Torque measurements for single-axis actuators is relatively simple because the fixed rotor-axis position facilitates the design of measuring structure. Stark *et al*. [16] have conducted the torque measurement on an outer-rotor micro motor by attaching a beam to the rotor on one side, and a fixed pad at the other side. The torque value can be obtained from the deflection of the beam. Lin *et al*. [17] have designed a structure to measure the torque of a large gap magnetic suspension system. A pendulum is mounted on the rotor. From the angular position measurement of pendulum motion, the magnetic torque can be obtained. Beihoff [18] has made a survey of torque transduction methodologies applicable to single-axis actuators. In recent years, the emergence of multi-DOF spherical actuators brings forward requirement of different force/torque measurement techniques because the torque of spherical actuators is dependant on rotor orientations. Amano *et al*. [19] have conducted the measurement of the horizontal direction torque on a 3-DOF ultrasonic actuator by adding pre-loading weight on the rotor. Mitchell *et al*. [20] have measured the reluctance torque of a 2-DOF spherical PM actuator by using an experimental test rig in which the rotor is fixed on the base and the stator angle can be adjusted. Roth [21] and Zhou [22] have conducted the torque measurement of VRSM by using a customized apparatus which can change the rotor shaft orientation.

A force/torque measurement apparatus is developed here to measure the six components of force/torque generated by the 3-DOF PM spherical actuator at any rotor orientation within the workspace. The actuator torque produced by a single stator coil within the magnetic field of the PM rotor is investigated first. The measured result is then compared with the analytical torque model of Eqn. (3.30) for the single coil. The linear relationship between torque output and current input in the torque model can be verified. Subsequently, experiments on measuring the actuator torque simultaneously produced by two stator coils are conducted. The measurement result should verify the principle of superposition on the actuator torque produced by multiple coils described by Eqn. (3.32).

5.2.1 Experiment on Torque Generated by a Single Coil

5.2.1.1 Apparatus of Torque Measurement

An apparatus is designed for the measurement of the torque generated between the PM-pole rotor and a single coil as shown in Fig. 5.14. The specifications of this torque measurement apparatus are listed in Table 5.4. A DC power supply (Topward 3303D [23]) provides current to the coil. A six-axis force/torque sensor (Fig. 5.15) that can measure three torque components and three force components is mounted

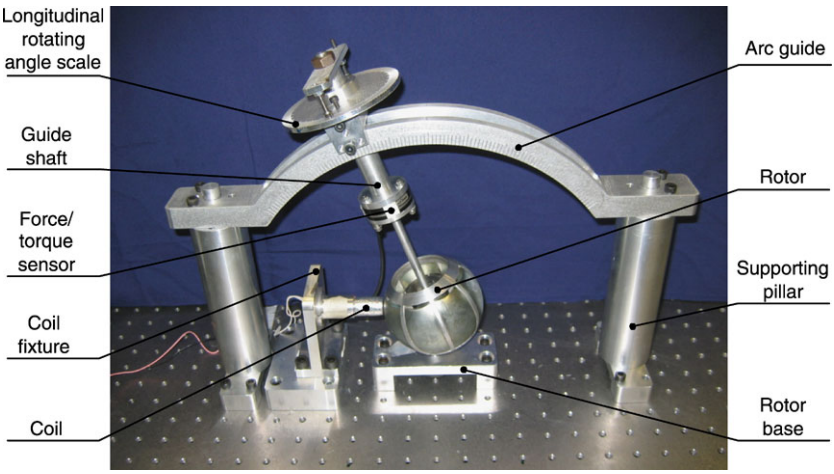

Fig. 5.14: An apparatus for force/torque measurement of single coil

on the shaft of the rotor. This sensor has a measuring range of 0.5Nm for torque component and 36N for force component. The rotor shaft is connected to a guide shaft. This guide shaft can slide along the slot of the arc guide so that the rotor can tilt. The tilting angle is indicated by the dials on the arc guide. The guide shaft can rotate about its own axis along with the rotor. The amount of rotation angle is indicated by the longitudinal rotation angle scale. The tilting and rotating motions determine the position of the coil axis (θ_p, ϕ_p) in the rotor frame. The relation between (θ_p, ϕ_p) and (θ, ϕ) is indicated in Fig. 5.5, i.e., $\theta_p = \pi/2 - \theta$, $\phi_p = \phi$. By using this apparatus, the measurement of actuator torque with respect to (θ_p, ϕ_p) can be obtained. In this experiment, the measuring range of ϕ_p is from 0° to 360°, and θ_p is from -20° to 20°, which completely covers the rotor orientations in the workspace.

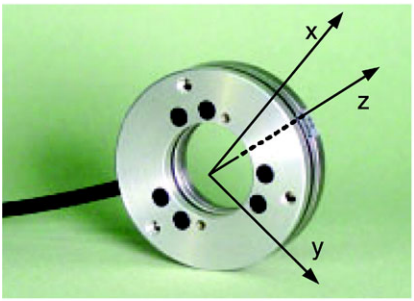

(a) Six-axis force/torque sensor

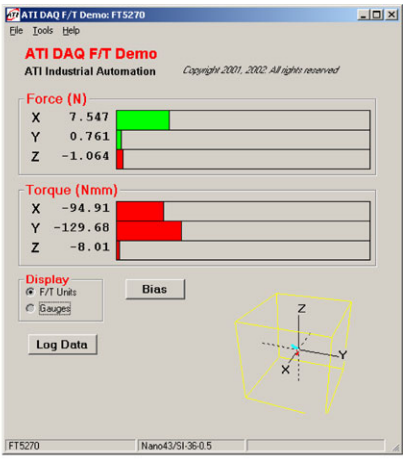

(b) DAQ interface

Fig. 5.15: Six-axis force/torque sensor and DAQ interface (ATI Nano43 [24])

Table 5.4: Specifications of the torque measurement apparatus

DC power supply	Model	Topward 3303D
	Range	0∼30V, 0∼3A
Torque sensor	Model	ATI Nano 43
	Channel	6-axis
	Force range	±36N
	Torque range	±0.5Nm
Measuring structure (Guide shaft)	Tilting range	±40°
	Rotating range	0∼360°

5.2.1.2 Coordinate Transformation from Sensor to Motor Torque

The raw data acquired from the six-axis force/torque sensor is based on the sensor coordinates as shown in Fig. 5.16; (x_e, y_e, z_e) represents the sensor coordinate system whereas (x_r, y_r, z_r) represents the rotor coordinate system. The measured data obtained from the sensor can be translated into the actual motor torque by

$$\begin{bmatrix} T_{rx} \\ T_{ry} \\ T_{rz} \end{bmatrix} = \begin{bmatrix} -\sin\delta & \cos\delta & 0 \\ \cos\delta & \sin\delta & 0 \\ 0 & 0 & -1 \end{bmatrix} \left\{ \begin{bmatrix} T_{ex} \\ T_{ey} \\ T_{ez} \end{bmatrix} + \begin{bmatrix} F_{ey} \\ -F_{ex} \\ 0 \end{bmatrix} L_e \right\}, \tag{5.13}$$

where F_{ex}, F_{ey}, F_{ez} and T_{ex}, T_{ey}, T_{ez} are force and torque components based on the sensor coordinates, T_{rx}, T_{ry} and T_{rz} are torque components based on the rotor coordinates, L_e is the distance from the origin of the sensor coordinates to the rotor center.

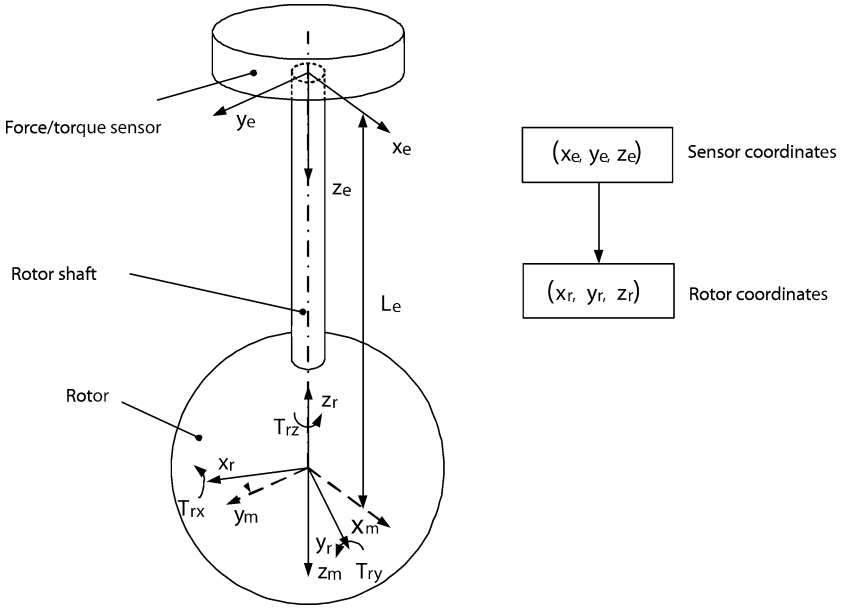

Fig. 5.16: Coordinate transformation of torque measurement

According to the assembly of this apparatus, there is a twist angle δ between the sensor coordinate system and the rotor coordinate system.

5.2.1.3 Analysis of Experimental Result

Visualization of experimental result:

The actuator torque is a (θ_p, ϕ_p)-dependant 3×1 vector consisting of three components. variation of torque output with respect to two angular parameters, θ_p and ϕ_p, can be observed in the stator coordinate system more clearly. Therefore, the three torque components in rotor coordinates are converted into the stator coordinate system (X_s, Y_s, Z_s), and denoted as T_{sx}, T_{sy} and T_{sz}. The coil is fixed in the stator coordinate system as shown in Fig. 5.17. Visualization of the actuator torque is done on each of the torque components, i.e., $(\theta_p, \phi_p, T_{sx})$, $(\theta_p, \phi_p, T_{sy})$ and $(\theta_p, \phi_p, T_{sz})$. In conducting the torque measurement, the distance from the coil to the rotor surface is kept very close to zero. 3A current is supplied into the coil.

Figures 5.18, 5.19 and 5.20 present experimental measurement result and analytical data of three torque components, T_{sx}, T_{sy} and T_{sz} respectively. The eight ridges appear in Figs. 5.18(a), 5.19(a) and 5.20(a) are caused by the eight alternately arranged PM poles along the rotor equator. The maximum difference between the experimental and analytical results is about 12%. The difference is mainly due to the

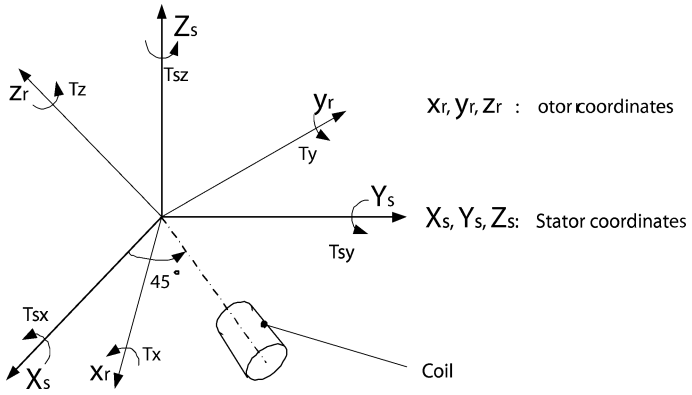

Fig. 5.17: Position of Coil in stator coordinates

omission of high order terms in formulating magnetic flux density, approximation of coil shape, fabrication error, etc.

Figure 5.18(d), 5.19(d) and 5.20(d) illustrates the torque variation at ϕ_p direction. It can be found that T_{sx} and T_{sy} change the direction when θ_p varies, whereas T_{sz} is always positive. In order to facilitate the comprehension of the torque variation shown in Fig. 5.18-5.20, Fig. 5.21 presents three positions of coil axis at (θ_p, ϕ_p)=(0°, 21°), (18°, 21°) and (−18°, 21°) respectively. In Fig. 5.21(a), the coil axis is on the rotor equator plane and between two neighboring PM poles. The interaction between the coil and the pole produces an attraction force (PM 1) and a repulsion force (PM 2). Due to the symmetry of PM poles, directions of both forces are on the rotor equator plane. Thus, a torque is generated about the z-axis of the rotor to create a spinning motion, whereas the torque components in the x- and y-direction are negligible. Therefore, one can see clearly that at $\theta_p = 0$ in Fig. 5.18(a) and 5.19(a), the torque in x- and y-directions are very small. In Fig. 5.21(b) and 5.21(c), the attraction and repulsion force can pull the rotor to spin in the z-axis. Because the resultant force is not on the rotor equator plane, torque in x and y directions can also be generated to tilt the rotor in different directions.

Torque variation with respect to airgap:

The torque output of the spherical actuator is also a function of the gap between coils and rotor surface. Based on the torque model of a single coil Eqns. (3.30) and (3.31), the actuator torque is related to the coil parameters R_0 and R_1, which, in turn, can be expressed by the gap d_a between the rotor surface and the coil tip as

$$R_0 = R_r + d_a, \tag{5.14}$$

$$R_1 = R_0 + L_c = R_r + d_a + L_c, \tag{5.15}$$

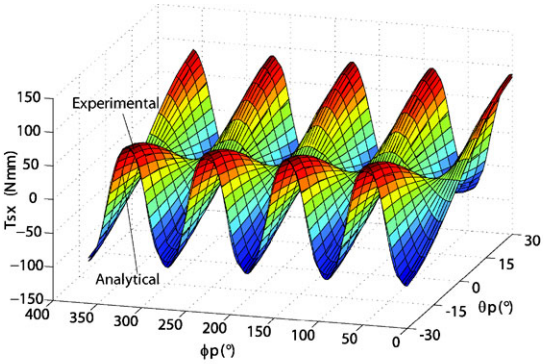

(a) T_{sx} torque variation in 3D space

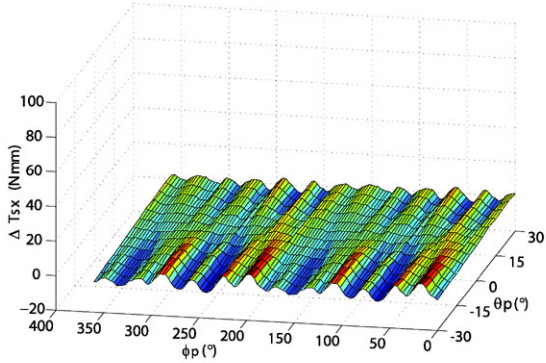

(b) Difference of analytical and experimental torque data

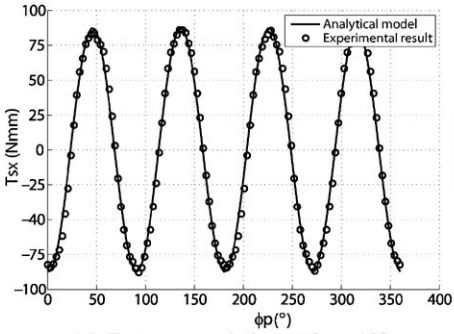

(c) T_{sx} torque variation at $\theta_p = 18°$

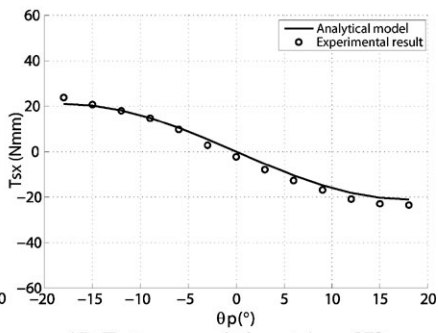

(d) T_{sx} torque variation at $\phi_p = 27°$

Fig. 5.18: Actuator torque in x-direction T_{sx}

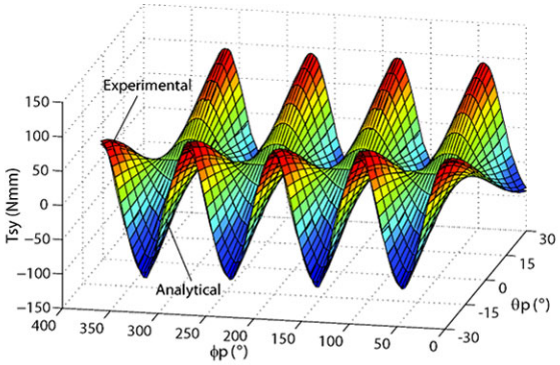

(a) T_{sy} torque variation in 3D space

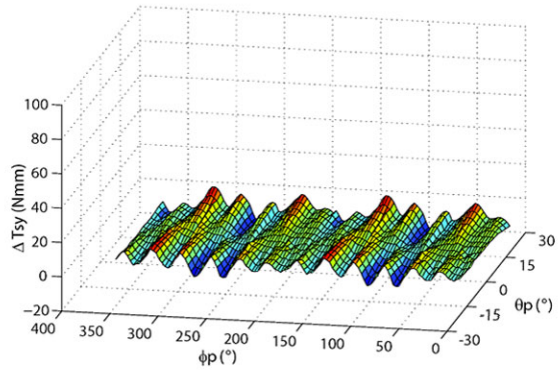

(b) Difference of analytical and experimental torque data

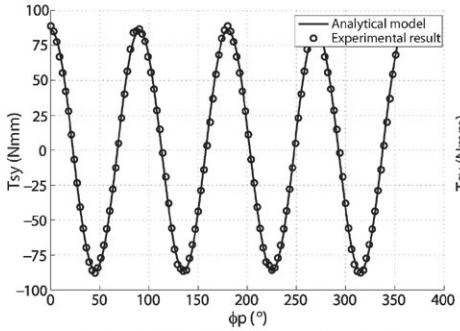

(c) T_{sy} torque variation at $\theta_p = 18°$

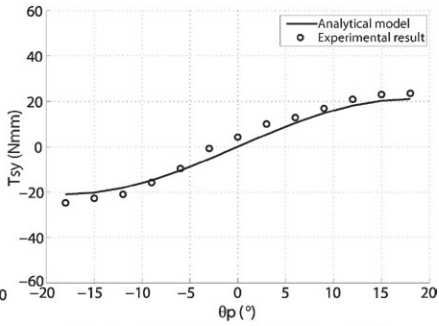

(d) T_{sy} torque variation at $\phi_p = 27°$

Fig. 5.19: Actuator torque in y-direction T_{sy}

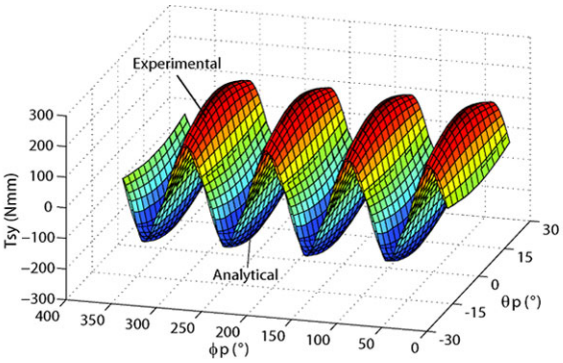

(a) T_{sz} torque variation in 3D space

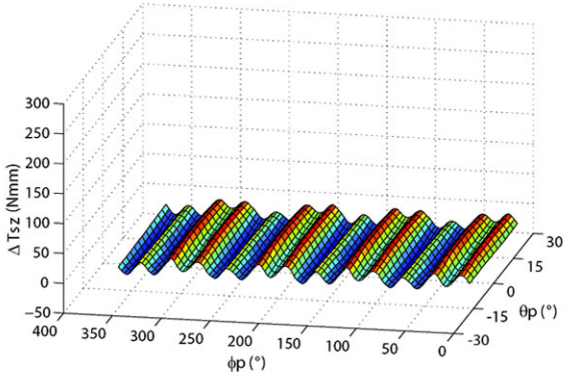

(b) Difference of analytical and experimental torque data

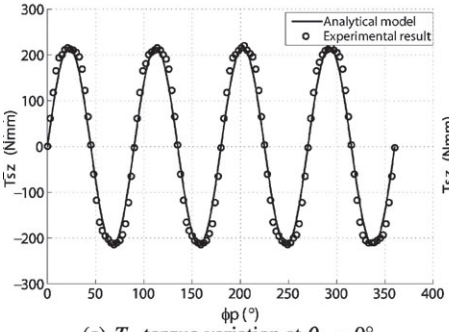

(c) T_{sz} torque variation at $\theta_p = 0°$

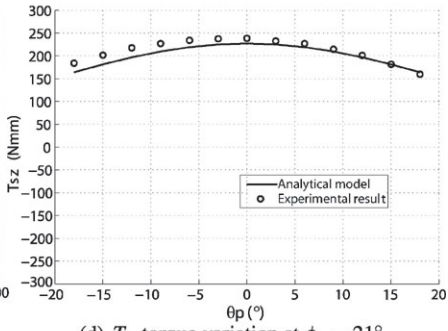

(d) T_{sz} torque variation at $\phi_p = 21°$

Fig. 5.20: Actuator torque in z-direction T_{sz}

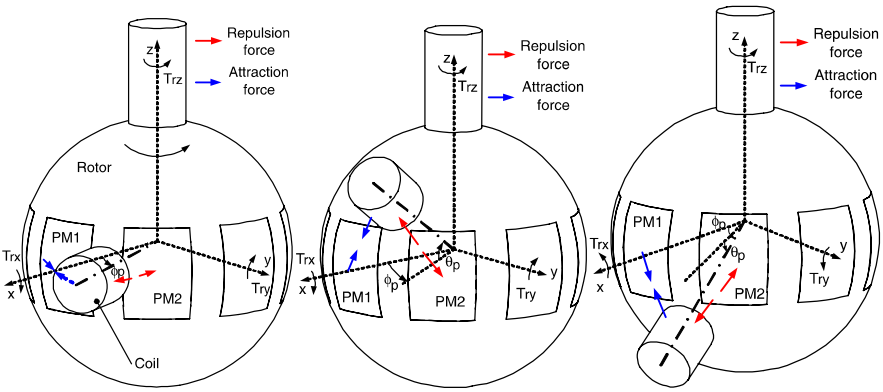

(a) $\theta_p = 0, \phi_p = 21^\circ$ (b) $\theta_p = 18^\circ, \phi_p = 21^\circ,$ (c) $\theta_p = -18^\circ, \phi_p = 21^\circ,$

Fig. 5.21: Rotor motion generated by torque components

where L_c is the coil length. By fixing the values of θ_p and ϕ_p and varying d_a, the relation between torque output and d_a can be obtained. In the torque measurement apparatus, the airgap d_a can be adjusted by screwing the coil in or out the fixture. Figure 5.22 shows the torque variation with respect to d_a at (θ_p, ϕ_p)=(15°, 25°). It can be seen that the torque decreases with increasing d_a. Therefore, to achieve high torque output, smaller value of d_a is preferred.

Linearity of torque model:

According to Eqn. (3.27) and (3.32), the torque output of this PM spherical actuator is always directly proportional to the current input in a linear fashion. This linearity of the torque model can facilitate real-time motion control of the actuator. Experiments are carried out here to verify this linearity relationship. In the experiment, the coil is mounted on a fixed position with respect to the rotor frame, $\phi_p = 21^\circ$, $\theta_p = -9^\circ$. By varying the current input, the torque output are measured. Figure 5.23 shows both experimental data and analytical calculation results. It can be found that three components of the torque are all proportional to the current input. The experimental result is interpolated with straight line of slope k', whereas the analytical linear relationship is characterized by the straight line of slope k. It can be shown that both analytical and experimental lines are close to each other. The difference is caused by approximation of coil shape, measurement error etc.

5.2.2 Experiment on Torque Generated by Multiple Coils

According to Eqn. (3.32), the total torque output of the spherical actuators is the superposition of torques generated by individual coils. To verify the viability of superposition principle, torque measurement is conducted on two arbitrarily chosen coils.

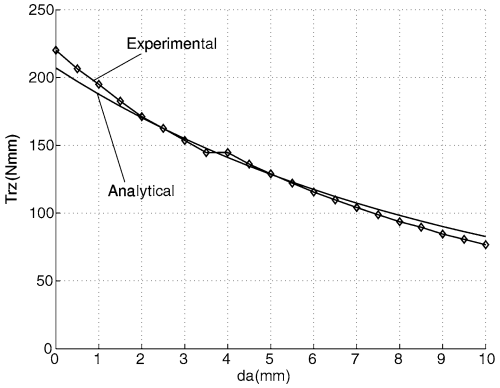

(a) Torque z

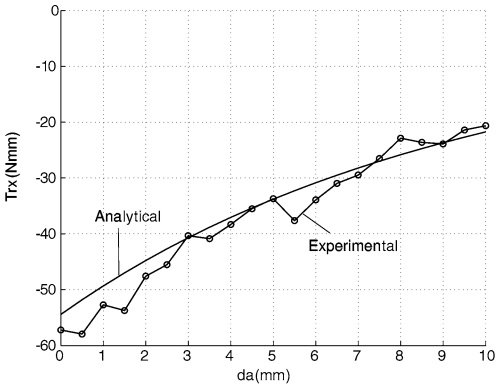

(b) Torque x

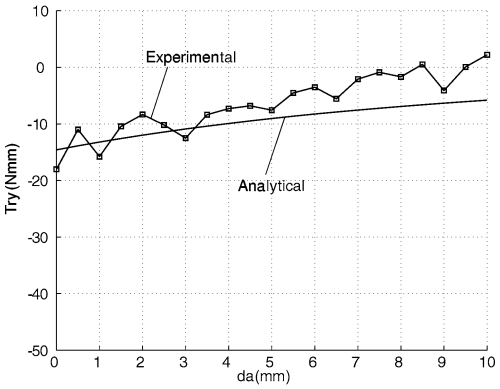

(c) Torque y

Fig. 5.22: Torque variation in the radial direction d_a ($\theta_p = 15°$, $\phi_p = 25°$)

5.2.2.1 Torque Measurement on Multiple Coils

Figure 5.24 shows that the same apparatus for torque measurement is used for multiple coils. The coils are mounted on the stator of the spherical actuator prototype instead of a special fixture.

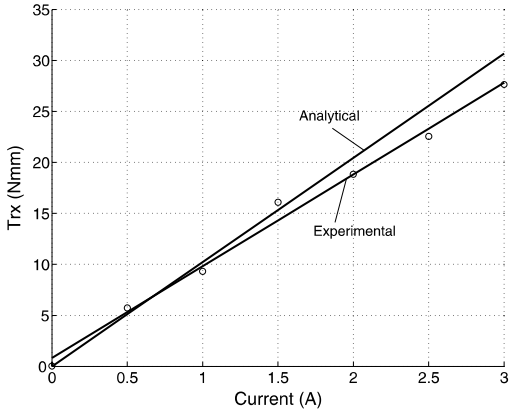

(a) Torque x ($k = 10.2$, $k' = 9.1$)

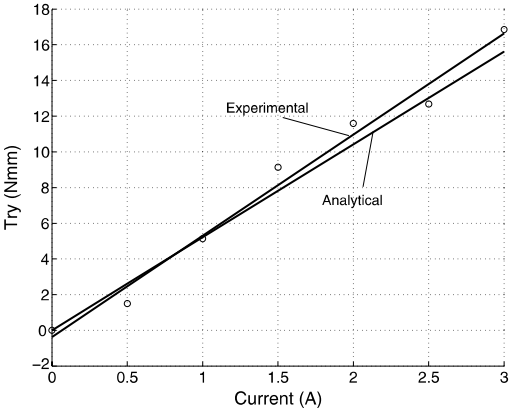

(b) Torque y ($k = 5.2$, $k' = 5.6$)

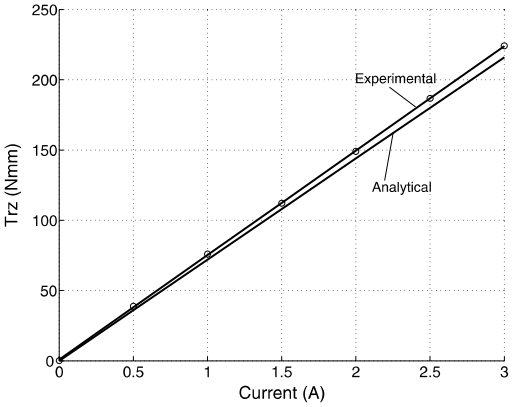

(c) Torque z ($k = 72.0$, $k' = 74.3$)

Fig. 5.23: Linearity of actuator torque and coil currents ($\phi_p = 21^\circ$, $\theta_p = -9^\circ$, k and k': slopes of analytical and experimental results respectively)

Two coils, Coil 1 and Coil 2 indicated in Fig. 5.24 are used for the experiment. The initial position of these coils in the rotor frame are (θ_p, ϕ_p)=(11°, 0) and (θ_p, ϕ_p)=(11°, 30°) respectively. The supplied current is 2.5A. Sliding the guide shaft along the arc guide will change orientation of the rotor. For any specified rotor orientation, three sets of data are captured: torque obtained by energizing Coil 1 alone, Coil 2 alone, and Coils 1 and 2 simultaneously. Then we compare the summation of the separate torque from the two coils and torque from the two simultaneously activated coils. The same measuring process is carried out for another pair of coils at Coil 3 (θ_p=−11°, ϕ_p=120°) and Coil 4 (θ_p=11°, ϕ_p=150°).

5.2.2.2 Experimental Result

The experimental result of the actuator torque is shown in Fig. 5.25 and 5.26. In each of these figures, there are five curves representing experimental torque generated by Coil 1 alone, by Coil 2 alone, sum of these two sets of data, experimental torque by Coil 1 and 2, as well as analytical torque produced by Coil 1 and 2. The sum of two sets of data and the experimental torque by Coil 1 and 2 fit closely to each other. The maximum differences between analytical and experimental results (Coil 1 and 2) of three torque components are about 18%, 12% and 9% of the experimental result respectively. For Coil 3 and 4, the maximum differences are about 12%, 15% and 16% respectively. Additionally, the torque generated by these four coils are also measured. The seven curves in each figure of Fig. 5.27 represents the experimental torque generated by Coil 1 alone, Coil 2 alone, Coil 3 alone, Coil 4 alone, sum of these four sets of data, experimental torque by Coil 1-4 together and

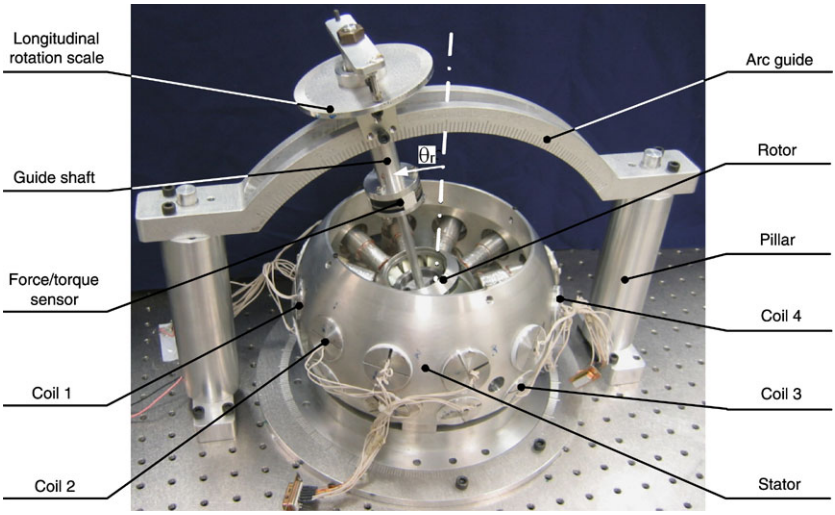

Fig. 5.24: Measurement apparatus of torque generated by multiple coils

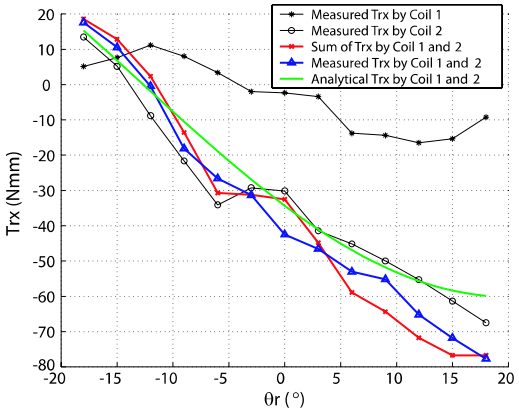

(a) Torque x

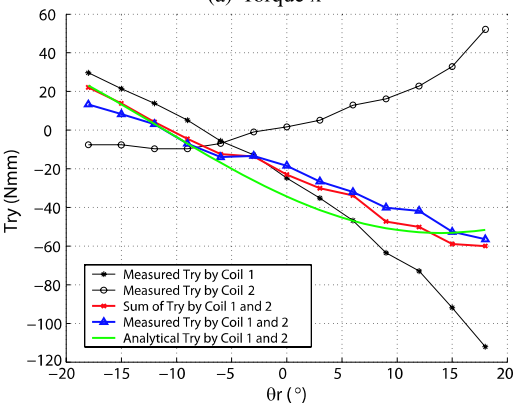

(b) Torque y

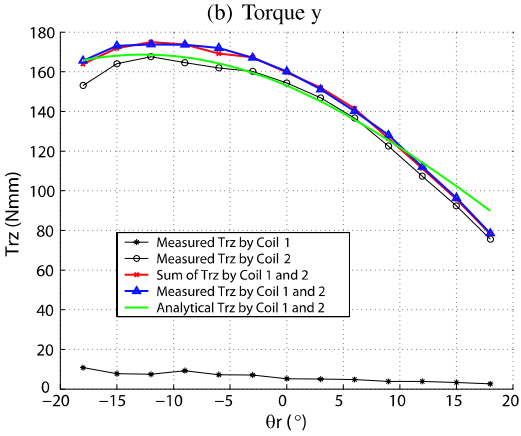

(c) Torque z

Fig. 5.25: Superposition of actuator torque for multiple coils (Coil 1 and Coil 2)

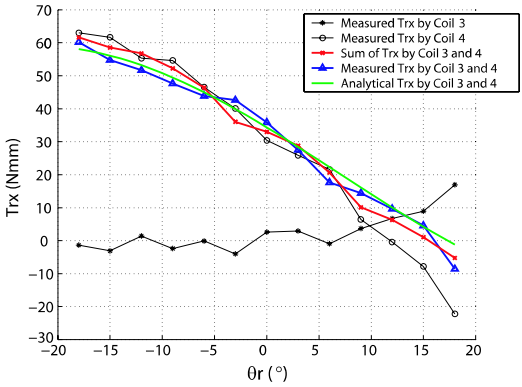

(a) Torque x

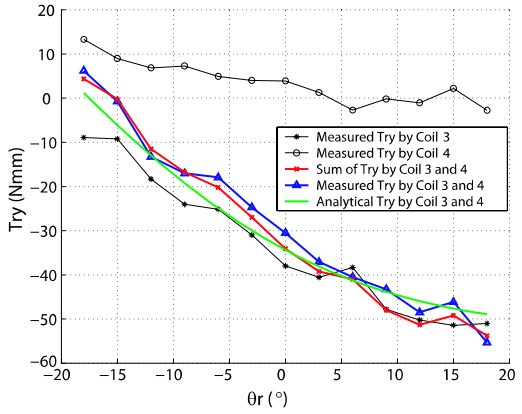

(b) Torque y

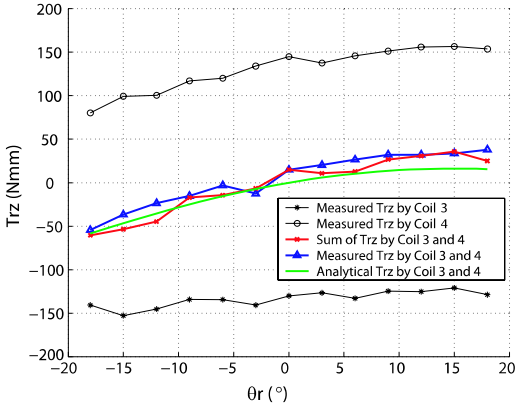

(c) Torque z

Fig. 5.26: Superposition of actuator torque output (Coil 3 and Coil 4)

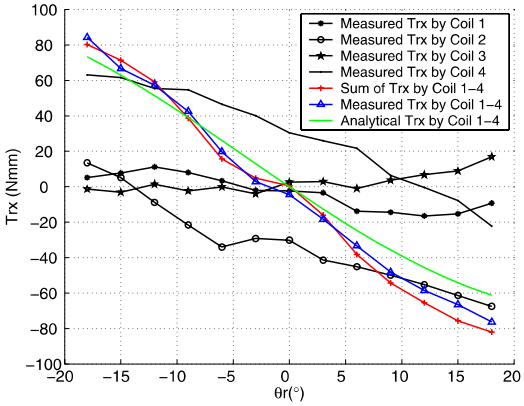

(a) Torque x

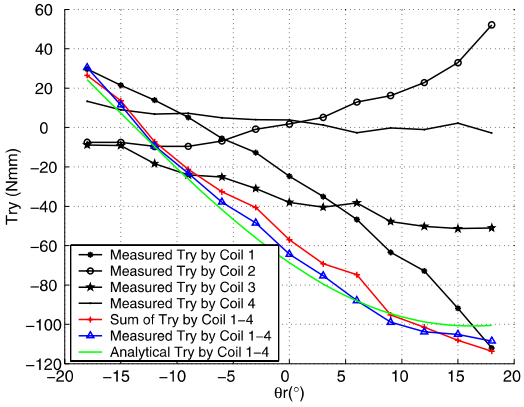

(b) Torque y

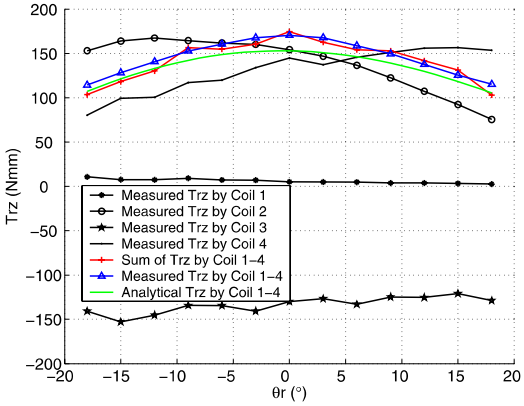

(c) Torque z

Fig. 5.27: Superposition of actuator torque output (Coils 1-4)

analytical torque produced by Coil 1-4. The trend of analytical result matches with the experimental result closely. The maximum differences between analytical and experimental results of three torque components are about 14%, 13% and 11% of the experimental result respectively. The different between analytical and experimental results could be caused by omission of higher order terms of magnetic scalar potential, approximation of coil shape, measurement error etc.

5.3 Summary

By taking advantage of the developed spherical actuator with dihedral-shaped PM rotor poles, experimental investigation has been carried out on the magnetic field distribution of the PM rotor and actuator torque variation in this chapter. An automated apparatus is developed to measure the magnetic field distribution in 3D space surrounding the PM-pole rotor. The experimental result verifies the analytical magnetic field expression of the PM rotor. The maximum difference between analytical and experimental result is about 7%. Furthermore, nondimensionalization approach is used to process the measured magnetic field as benchmark result to be referred by other similar rotor designs. An apparatus is designed to measure the actuator torque output within the workspace. The measurement result is compared with analytical model, which shows that the maximum difference is about 12% of the experimental result. The difference can be produced by the omission of higher-order terms of magnetic scalar potential, approximation of coil shape, measurement error etc. One of the advantages of the PM spherical actuator is the linear torque model, i.e., the torque output is always directly proportional to the current input. Compared with nonlinear model, the computation of linear torque model is more effective for real-time control algorithm. In this chapter, experimental torque measurement with respect to current input verifies the linearity of the torque model. In addition, according to the actuator torque model for full set of coils, the total actuator torque is equal to the sum of torques generated by individual coils. Torque measurement on multiple coils mounted on the stator verifies the superposition principle of the actuator torque output.

References

1. Lake Shore Cryotronics, Inc. (2005) Specification of Gauss Meter. In: The website of Lake Shore Cryotronics, Inc. Available online: http://www.lakeshore.com/. Cited May 2005
2. Mintchev P M, Christov C D, Rahman A M et al (1975) Analysis of flux in electromagnets having rectangular cross-section. IEEE Transactions on Magnetics, vol. 11, no. 5:1550–1551, September 1975.
3. Mintchev P M (1987) Optimum design of electromagnets by means of the goodness factor approach. IEEE Transactions on Magnetics, vol. 23, no. 5:3777–3779, September 1987.
4. Furlani E P (1992) A method for predicting the field in permanent-magnet axial-field motors. IEEE Transactions on Magnetics, vol. 28, no. 5:2061–2066, September 1992.

5. Enokizono M, Morikawa M, Fujiyama S, Sievert J, Serikawa I et al (1999) Distribution of local magnetic properties in three-phase induction motor model core. IEEE Transactions on Magnetics, vol. 35, no. 5:3937–3939, September 1999.
6. Wang J, Jewell G W, Howe D et al (1998) Spherical actuators with multiple degrees-of-freedom. IEE Colloquium on Limited motion electrical actuation systems, Hague, Netherlands, no. 1998/494:8/1–8/6, Seoul, Korea, 13-15 October 1998.
7. Wang J, Jewell G W, Howe D et al (1998) Analysis, design and control of a novel spherical permanent-magnet actuator. IEE Proceedings: Electric Power Applications, Hague, Netherlands, vol. 145, no. 1:61–71, January 1998.
8. Lake Shore Cryotronics, Inc. (1997) Model 460: 3-Channel Gaussmeter Manual. USA, 1997.
9. NSK, Ltd. (1996) Robto Modules system: User's manual. USA, 1996.
10. Deterco Inc. (2005) Specification of the Millitron Probe. Available online: http://www.deterco.com/products/Mahr%20Federal/mahr/millimar/militron1318.htm. Cited May 2005
11. Amtec Inc. (2005) Specification of the single-axis servo motor. Available online: http://www.amtec-robotics.com/. Cited May 2005
12. Deterco Inc. (2005) Specification of the Millitron. Available online: http://www.deterco.com/products/Mahr%20Federal/mahr/millimar/eval/1240/techdata.htm. Cited May 2005
13. Zhang Z M, Zhang Y Y, Xie Y B, Chen Z X, Qiu D M, Zhu J et al (1986) Theory of Hydrodynamic Lubrication of Journal Bearing. China Higher Education Press, China, 1986.
14. Lin C C, Segel L A et al (1974) Mathematics applied to deterministic problems in the natural sciences. Macmillan Publishing Co., Inc., USA, 1974.
15. Fowler A C (1997) Mathematical Models in the Applied Sciences. Cambridge University Press, USA, 1997.
16. Stark K C, Mehregany M, Phillips S M et al (1997) Mechanical Coupling and Direct Torque Measurement of Outer-rotor Polysilicon Micromotors. Proceedings of the 10^{th} International Workshop on Micro Electro Mechanical Systems, Nagoya, Japan, 26–30, Albuquerque, New Mexico, USA, January 1997.
17. Lin C E, Jou H L, Yan J H et al (1994) A dynamic method for magnetic torque measurement using pendulum motion system. IMTC'94 IEEE Conference, Nagoya, Japan, vol. 3:376–379, Hamamatsu, Japan, 10–12 May 1994.
18. Beihoff B (1996) A survey of torque transduction methodologies for industrial applications. Conference Record of 1996 Annual, Pulp and Paper Industry Technical Conference, Birmingham, Alabama, USA, vol. 3:220–229, Hamamatsu, Japan, 10–14 June 1996.
19. Amano T, Ishii T, Nakamura K, Ueha S et al (1998) An ultrasonic actuator with multi-degree of freedom using bending and longitudinal vibrations of a single stator. Proceedings of 1998 IEEE International Ultrasonic Symposium L-5, vol. 22:667–670, Sendai, Japan, October 1998.
20. Mitchell J K, Jewell G W, Wang J, Bingham C M, Howe D et al (2002) Influence of an aperture on the performance of a two-degree-of-freedom iron-cored spherical permanent-magnet actuator. IEEE Transactions on Magnetics, vol. 38, no. 6:3650–3653, November 2002.
21. Roth R B (1992) An Experimental Investigation and Optimization of a Variable Reluctance Spherical Motor. Thesis of Georgia Institute of Technology, GA, USA, 1992.
22. Zhou Z (1995) Real-Time Control and Characterization of a Variable Reluctance Spherical Motor. Thesis of Georgia Institute of Technology, GA, USA, May 1995.
23. Deterco Inc. (2005) Specification of the Millitron. Available online: http://www.testmart.com/in.cfm/DCPWR/TOPWAR/3303D.html. Cited May 2005
24. ATI Industrial Automation (2002) Manual of Multi-Axis Force/Torque Sensor. USA, 2002.

Chapter 6
Three Degree-of-freedom Optical Orientation Measurement

6.1 Introduction

The displacement measurement technologies based various working principles for single direction motions [1, 2, 3, 4, 5, 6, 7] or planar linear motions [8, 9, 10] have been widely used for long history. However, the emergence and advance of multi-DOF rotary actuators in recent years bring forward the requirement on simultaneous measurement of multi-DOF rotational motions. Some 2/3-DOF orientation measurement methods have been proposed by researchers previously. For example, Lee *et al*. have developed a 3-DOF orientation measurement system by using three single-axis encoders to detect the rotor motion of VRSM [11, 12]. The same approach has been employed by Weck *et al*. for the orientation measurement of a 3-DOF spherical motor. This type of orientation measurement method is capable of achieving high-resolution measurement results. However, it requires a mechanism that consists of two arc-shaped guides and a sliding block to connect the rotor shaft to the encoders. The bulky structure of this measuring system contributes two-thirds of the total inertia moment to the motor, and large friction exists on the bearings, which compromises the rotor dynamics and complicates the control implementation of the measurement system. To avoid additional inertial moment and friction, non-contact type orientation measurement method, i.e., there is no contact between the measurement system and the moving body, is preferred for orientation measurement. A non-contact real-time vision-based absolute orientation sensor has been proposed by Garner *et al* [13, 14]. A spherical shell surface marked with grid patterns is mounted on the rotor shaft, and an image processing vision system is developed to capture and analyze the grid pattern images. The orientation of the spherical shell can thus be detected. Although there is no contact between the rotor surface and the vision system, the spherical shell still adds extra inertia moment on the rotor. The spherical shell's center must be coincident with that of rotor. The resolution of this vision-based orientation measurement system depends on the density of grid pattern. Lee *et al*. have proposed another non-contact orientation measurement sensor, a microscopic-surface-based optical sensor [15, 16]. Its performance

L. Yan et al., *Design, Modeling and Experiments of 3-DOF Electromagnetic Spherical Actuators*, Mechanisms and Machine Science 4,
DOI 10.1007/978-94-007-1646-9_6,

has been evaluated through experiments. For this measurement method, the grid pattern on a spherical surface is no longer required. However, the output of the optical sensor is very sensitive to the gap size as well as the relative motion speed between the moving surface and the sensor tip. Its practical availability needs to be validated further. Another possible solution for orientation measurement is Hall effect sensor. The orientation measurement method with Hall sensors has been used in the spherical actuator developed by Wang *et al*. [17, 18], and the spherical wheel developed by Lee *et al* [19]. Several Hall effect sensors can be placed at different positions relative to the rotor. Compared with the magnetic field model formulated analytically, the rotor orientation could be derived from the measured value of flux density by these Hall sensors. Similar approach was used by Foggia *et al*. to detect the position of bottom aperture of a 3-DOF spherical actuator [20]. Jin *et al*. [21] have also demonstrated a single Hall sensor to measure the direction of a non-contact electronic joystick. The horizontal vector of the magnetic flux is detected by the Hall sensor while a PM rotates with the joystick bar. Hence, the direction of the joystick handle can be computed. However, because the magnetic field of the moving body with PM poles does not vary too much at certain positions, it is difficult to detect the rotor orientation in high resolution, which constrains the implementation of Hall-effect-based orientation measurement method. Furthermore, the reading of magnetic flux is also very sensitive to the gap size between the PM and the Hall sensor, and easy to be disturbed by environment magnetic field, which may cause large orientation measurement error.

In this study, a 3-DOF high-precision laser-based non-contact orientation measurement methodology is proposed for the application of spherical actuators. A laser detector is used to measure the distance between the light spots on a flat plane of a moving body and the laser, and thus to compute the orientation of the moving body. It can achieve high-precision orientation measurements for multi-DOF rotational rigid bodies. As there is no contact between the moving body and measurement system, the extra mass/inertia moment and friction that may compromise the system measurement performance do not exist any more. Compared with other non-contact orientation measurement methods, the precision of this measurement method is not affected by the gap size between the moving body and the sensor tip, as well as the environmental field.

6.2 Operating Principle

Laser sensors fall into the general category of non-contact measurement devices based on the principle of triangulation. As indicated in Fig. 6.1(a), the sensors work by projecting a beam of light onto the object of interest (e.g. anodized aluminum) and capturing the reflected light with a detector. The sensor enclosure, the emitted laser and the reflected laser light form a triangle. The distance from the target to sensor reference point can thus be calculated by determining where the reflected light falls on a detector. A triangulation laser sensor can be broken down into three

subsystems: transmitter, receiver, and electronic processor (Fig. 6.1(b)). The transmitter, typically a laser diode with beam-shaping optics, projects a beam that illuminates the target object. The receiver/detector subsystem gathers the light reflected off the target, images the light onto a detector, and reports the spot position to the processor, which then determines the measured distance. Laser sensors can achieve very impressive measurement performance. The data rate is in the order of 200 kHz, the measuring range from 0.5 mm up to 500 mm, and the resolution up to 0.01 μm.

Due to the laser sensor's high performance, it can be employed to conduct the high-precision measurement on 3-DOF rotations of a rigid body in 3D space. The basic operating principle of this orientation measurement methodology is illustrated in Fig. 6.2. It is known that any orientation of a rigid body can be achieved with three sequential rotations about global coordinate system or moving coordinate system [22]. The axis direction OO' of the plate indicated in Fig. 6.2(a) can be achieved with two rotations about the moving coordinates, and then the orientation of the rigid body in 3D space can be determined by the third rotation, i.e., the spinning motion around OO' axis. Imagine a flat plane on the bottom of the rigid body. Three laser beams that are not on the same plane point upward to the plane. It can be verified that the direction of axis OO' can be determined if the distances of AA', BB' and CC' are all known. Furthermore, if the position of O is fixed, only two of the three beams such as AA' and BB' can give the OO' direction. (O is not on the plane formed by AA' and BB'.) In order to measure the spinning angle, slots are fabricated on the bottom plane of the rigid body as indicated in Fig. 6.2(b). Some laser beams such as CC' can be used to sense the slot numbers that pass by the laser beam and calculate the spinning angle. The measuring resolution of the spinning angle is affected by the density of slots on the bottom plane. Interpolation computation could be employed to improve the resolution further. To obtain the direction of OO' precisely, at least two points such as A' and B' should be out of the slots. If one of them is out of the slot, whereas the other is in the slot, it may cause measurement

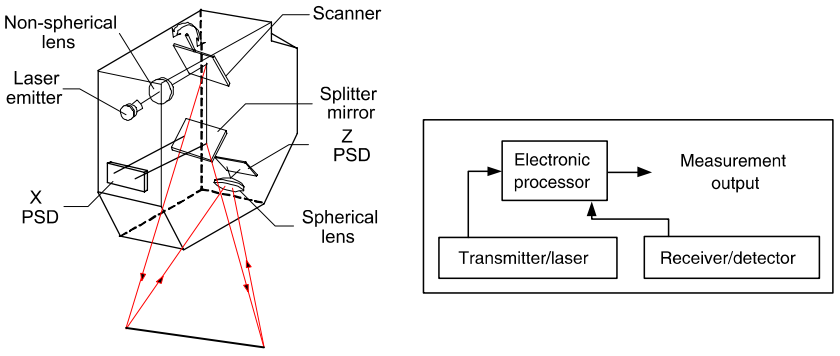

(a) Major components (b) Signal processing

Fig. 6.1: Triangulation operating principle of laser sensor

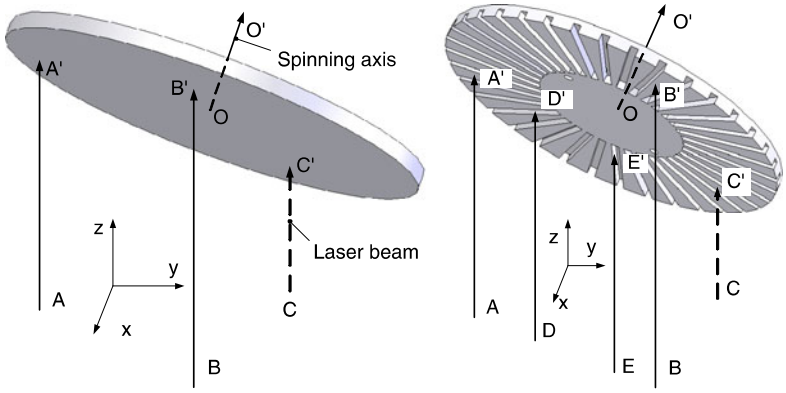

(a) Tilting angles (b) Spinning angle

Fig. 6.2: Orientation measurement of rigid body in 3D space

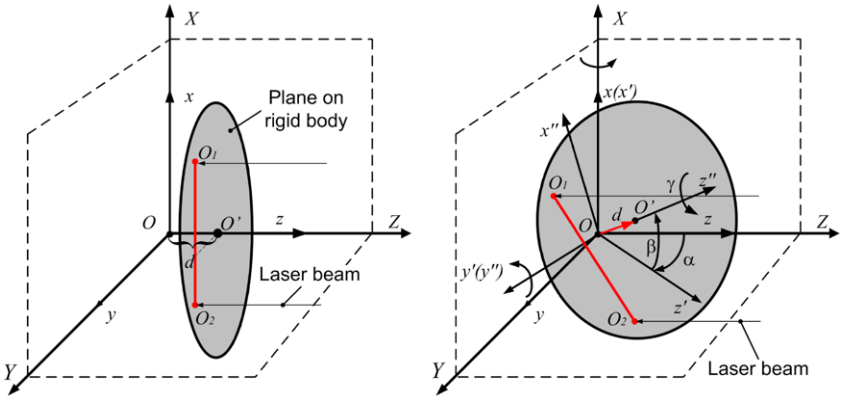

(a) Initial position of local frame (b) Rotation of local frame

Fig. 6.3: Definition of global frame and local frame on rigid body

errors of OO' direction. To prevent this situation, another one or more pairs of laser beams such as DD' and EE' could be used to ensure that at least one pair of these light spots are at outside of the slot for computation of tilting angles.

6.3 Algorithm for Computing Rotation Angles

6.3.1 Definition of Coordinate Systems

The relationship between the local frame (xyz) attached on the rotary rigid body and the global frame (XYZ) is illustrated in Fig. 6.3. Point O is the rotation center of the

rigid body. The local frame is coincident with the global frame at the initial position (Fig. 6.3(a)), and z-axis is normal to the plane on the rigid body. As indicated in Fig. 6.3(b), orientation of the rigid body can be determined by three rotations in order: first rotation about x-axis by α, second rotation about y'-axis of the moving frame by β, and third rotation about z''-axis by γ, where α and β are tilting angles, and γ is spinning angle.

6.3.2 Calculation of Tilting Angles

The coordinates of O' in the global frame XYZ can be represented as

$$\overrightarrow{OO'} = [d\sin\beta, d\cos\beta\sin\alpha, d\cos\beta\cos\alpha]^T, \tag{6.1}$$

where d is the distance between O and O'. The coordinates z_1 and z_2 of Q_1, Q_2 can be obtained from the laser sensor, whereas x_1, x_2, y_1 and y_2 can be set in the sensor's controller. Therefore, the positions of $Q_1(x_1, y_1, z_1)$ and $Q_2(x_2, y_2, z_2)$ in the global system are known. As a result, the vectors $\overrightarrow{O'Q_1}$ and $\overrightarrow{O'Q_2}$ can be computed as

$$\begin{aligned}\overrightarrow{O'Q_1} &= [x_1 - d\sin\beta, y_1 - d\cos\beta\sin\alpha, z_1 - d\cos\beta\cos\alpha]^T,\\ \overrightarrow{O'Q_2} &= [x_2 - d\sin\beta, y_2 - d\cos\beta\sin\alpha, z_2 - d\cos\beta\cos\alpha]^T.\end{aligned}$$

Because $\overrightarrow{OO'}$ is perpendicular to $\overrightarrow{O'Q_1}$ and $\overrightarrow{O'Q_2}$, we have

$$\begin{aligned}\overrightarrow{O'Q_1}\cdot\overrightarrow{OO'} &= 0,\\ \overrightarrow{O'Q_2}\cdot\overrightarrow{OO'} &= 0,\end{aligned}$$

i.e.,

$$\begin{aligned}x_1 d\sin\beta + y_1 d\cos\beta\sin\alpha + z_1\cos\beta\cos\alpha - d^2 &= 0,\\ x_2 d\sin\beta + y_2 d\cos\beta\sin\alpha + z_2\cos\beta\cos\alpha - d^2 &= 0.\end{aligned} \tag{6.2}$$

Assume $-45^\circ \leqslant \alpha \leqslant 45^\circ$ and $-45^\circ \leqslant \beta \leqslant 45^\circ$, and given $u_1 = \sin\alpha$, $u_2 = \sin\beta$. Eqn. (6.2) can thus be reorganized as

$$\begin{aligned}x_1u_2 + y_1u_1\sqrt{1-u_2^2} + z_1\sqrt{1-u_1^2}\sqrt{1-u_2^2} - d &= 0,\\ x_2u_2 + y_2u_1\sqrt{1-u_2^2} + z_2\sqrt{1-u_1^2}\sqrt{1-u_2^2} - d &= 0.\end{aligned} \tag{6.3}$$

It can be seen that u_1 and u_2 can be solved from Eqn. (6.3) with Extended Homotopy Algorithm, and thus the two tilting angles, α and β, can be obtained.

6.3.3 Calculation of Spinning Angle

The slots on the bottom of the rigid body can generate pulses signal on the laser sensor, which can be used to calculate the spinning angle γ of the rigid body. Specifically, the spinning angle can be computed as

$$\gamma = \gamma_p + \varepsilon, \tag{6.4}$$

where γ_p can be calculated from the signal pulses as

$$\gamma_p = \Delta\gamma \times n. \tag{6.5}$$

$\Delta\gamma$ is the angular density of slots, and n is the number of signal pulses. ε is the estimated angle in between two slots according to the rotation speed in the last pulse

$$\varepsilon = v \times \Delta T, \tag{6.6}$$

where ΔT is the time elapsed since the last switch of peak values, and v can be calculated from the last pulse as

$$v = \Delta\gamma / T. \tag{6.7}$$

T is the time in the last pulse period.

6.4 Experimental Measurement

Two measurement apparatuses are developed to test the workability and performance of the proposed 3-DOF orientation measurement method. The first apparatus is developed by using a high-precise single-axis servo motor to evaluate the measurement precision on three rotation angles individually, whereas the other testbed is used to verify that the laser-based measurement method can detect three rotations in 3D space simultaneously.

6.4.1 Experimental Measurement on Apparatus 1

A high-precision single-axis servo motor (Powercube) is utilized to evaluate the performance of the orientation measurement method. As shown in Fig. 6.4, an aluminum plate is mounted on the motor so that it can rotate precisely together with the motor under control. The laser sensor (Keyence) is mounted on a platform and beneath the plate. The sensor holder can adjust the sensor's position with respect to the plate. The laser sensor can emit light beams on the plate and measure the distance of each light beam from the laser to the light spot on the plate. In this study, four

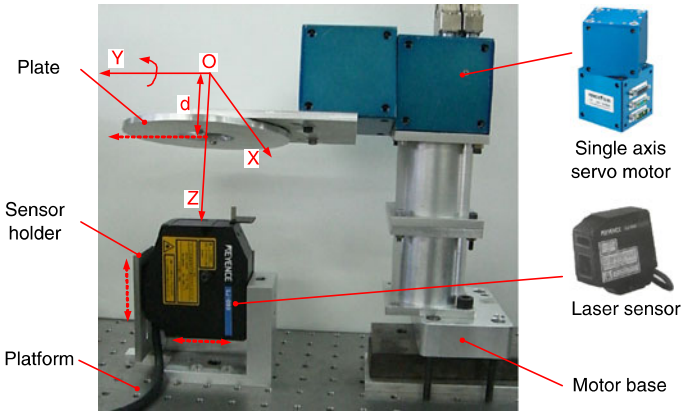

Fig. 6.4: Orientation measurement on single-axis servo motor (Position *I*)

Table 6.1: Specification of single-axis servo motor and laser sensor

Motor model	PR 070	Laser sensor	LJ-080
Precision	$\pm 0.02^{\circ}$	Controller	LJ-3000
Max. velocity	238°/sec	Resolution	10 μ
Motion range	$\pm 160^{\circ}$	Distance	80 ± 15mm
Voltage	24 ± 1V	Cycle time	30ms
Max. current	15A	Points No.	1000

laser beams are utilized for the orientation measurement. Specifications of the servo motor and the laser sensor are listed in Table 6.1. Motion resolution of the motor is up to 6 Arcsec/Inc., which helps to evaluate the orientation measurement result precisely. The laser sensor's high resolution 10μm can reduce the measurement error. The sensor's controller is connected to the computer for data collection and processing. The cycle time of 30ms can be reduced significantly by using data acquisition card. New models of laser sensors can used to provide much higher resolution (0.01 μm) and frequency (200 kHz), which may greatly improve the precision and speed of orientation measurement. In this measurement apparatus, the position of the laser sensor with respect to the plate can be changed so that it can measure the orientation in different directions. Several sensor positions are selected and corresponding measurements are conducted as follows.

6.4.1.1 Experimental Measurement of Tilting Motion at Position *I*

The sensor position indicated in Fig. 6.4 is denoted as Position *I*. The plate can be rotated precisely under the control of the servo motor. The rotation angle of the plate can be measured by the laser, and then compared with the standard value.

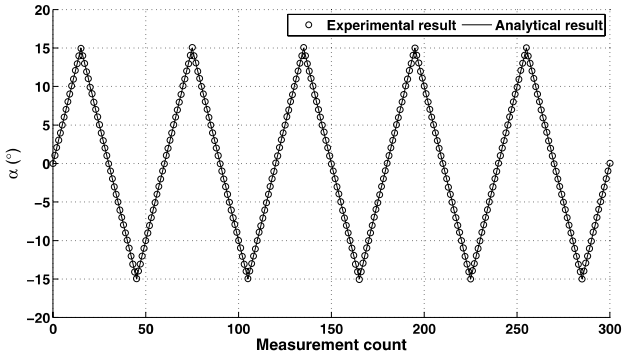

(a) Experimental & analytical results

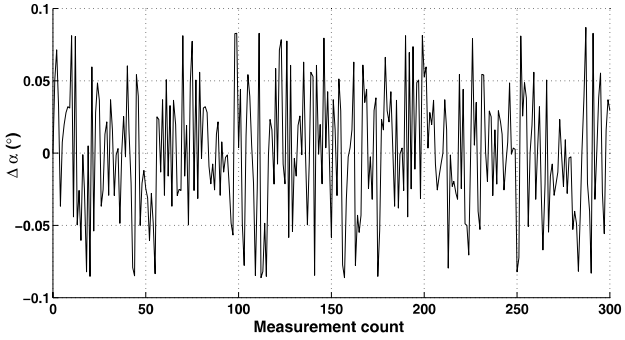

(b) Difference between experimental & analytical results

Fig. 6.5: Experimental measurement on the first tilting motion (Position *I*)

The measurement is repeated 100 times. Five cycles of the experimental result are shown in Fig. 6.5. It can be seen that the experimental result is closely fitted with the standard value. The maximum difference between them is around 0.08°. The difference may be caused by the resolution of the laser sensor, surface treatment of the plate, and the assembly error of the apparatus.

6.4.1.2 Experimental Measurement of Tilting Motion at Position *II*

As indicated in Fig. 6.6(a), the laser sensor can be rotated to Position *II* that is perpendicular to Position *I*. It is equivalent to rotating the motor axis by 90° in the opposite direction, and measuring the rotation of plate in the second DOF. The experimental and analytical results are presented in Fig. 6.7. Similarly, the two sets of data fit with each other closely. The maximum difference is about 0.065°, which

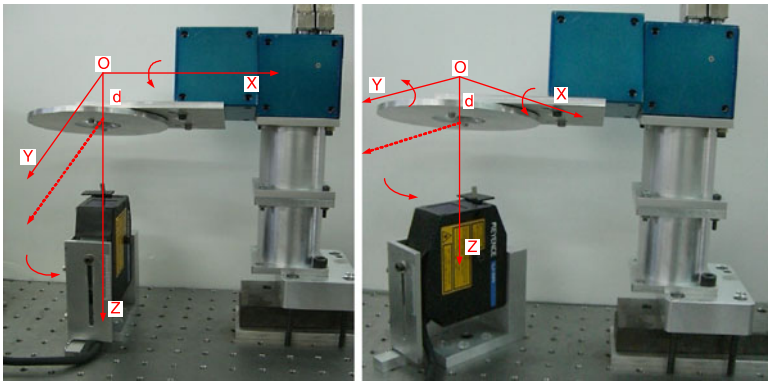

(a) Position *II* (b) Position *III*

Fig. 6.6: Experimental measurement at Position *II* and *III*

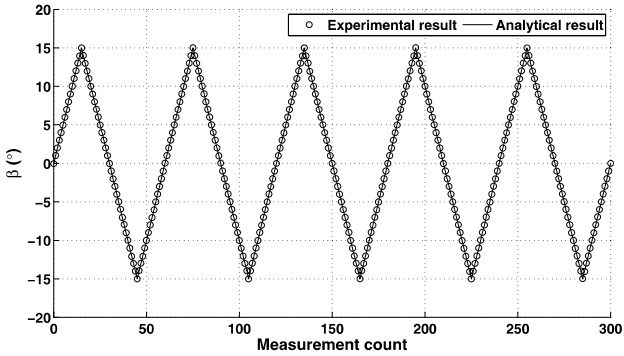

(a) Experimental & analytical results

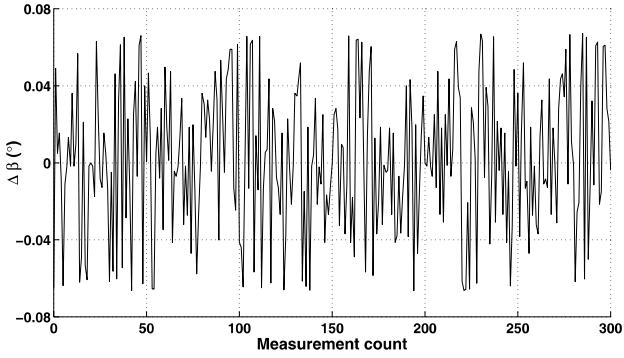

(b) Difference between experimental & analytical results

Fig. 6.7: Experiment on the second tilting motion (Position *II*)

is acceptable for requirement of most measurement situations. The major reasons that cause the difference are the same as that of measurement errors at Position *I*.

6.4.1.3 Experimental Measurement of Tilting Motion at Position *III*

Similarly, the laser sensor can rotate an angle such as 60° from position *I* to a position in between *I* and *II* (Position *III* in Fig. 6.6(b)), so that the sensor can measure two tilting angles simultaneously. The rotation of the single-axis motor together with the plate can be decomposed into two tilting motions, α and β, as

$$\alpha = \arctan(\frac{C_2}{C_3}), \quad \beta = \arctan(\frac{C_1}{\sqrt{C_2^2 + C_3^2}}), \tag{6.8}$$

where C_1, C_2 and C_3 are components of vector C that can be calculated as

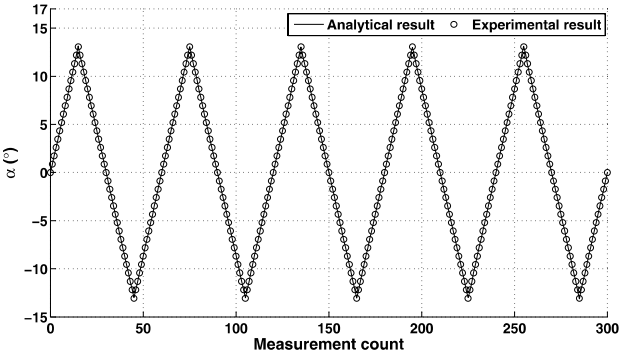

(a) Experimental & analytical results of α

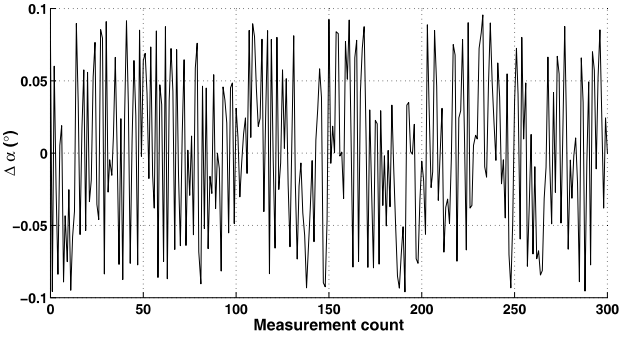

(b) Difference between experimental & analytical results of α

Fig. 6.8: Experimental measurement on the tilting motion at Position *III*

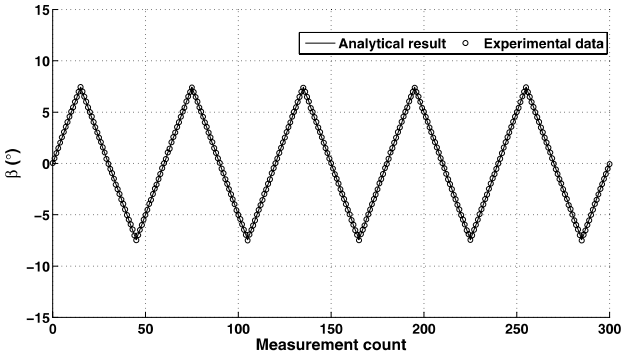

(c) Experimental & analytical results of β

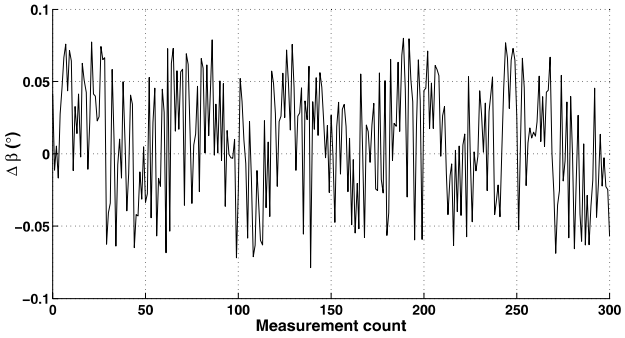

(d) Difference between experimental & analytical results of β

Fig. 6.8: Experimental measurement on the tilting motion at Position *III*

$$C = R_z(\theta_3)R_y(\theta_2)\begin{bmatrix}0 & 0 & 1\end{bmatrix}^T, \tag{6.9}$$

where

$$R_y(\theta_2) = \begin{bmatrix}\cos\theta_2 & 0 & \sin\theta_2 \\ 0 & 1 & 0 \\ -\sin\theta_2 & 0 & \cos\theta_2\end{bmatrix}, \tag{6.10}$$

$$R_z(\theta_3) = \begin{bmatrix}\cos\theta_3 & -\sin\theta_3 & 0 \\ \sin\theta_3 & \cos\theta_3 & 0 \\ 0 & 0 & 1\end{bmatrix}. \tag{6.11}$$

$\theta_3 = 60^\circ$ is determined by the rotation angle of the laser sensor from Position *I* to *II*, and θ_2 is the rotation angle of the single-axis motor. From Eqn. (6.9), the analytical result of α and β from the motor rotation can be computed and compared with the experimental result, which is presented in Fig. 6.8. It can be seen that maximum

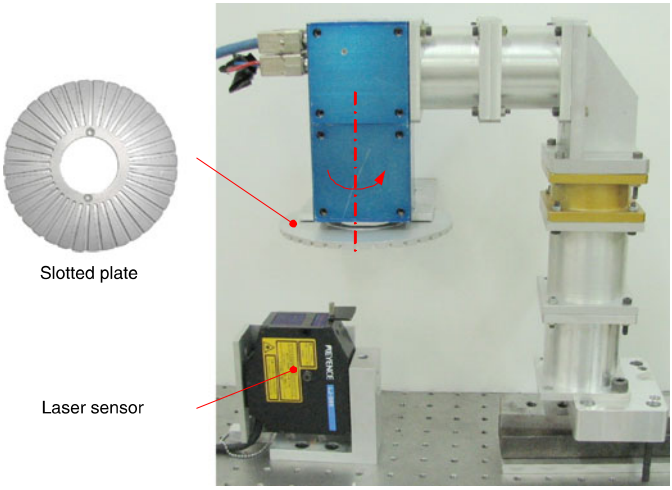

Fig. 6.9: Testbed for measurement of spinning motion

values for both tilting angles are smaller than 15° as the motor rotation is decomposed into two components. The experimental result fits the analytical result well. The maximum difference is 0.095° and 0.075° for α and β respectively. This result shows that the laser-based measurement method can measure the tilting motion of a rigid body in two directions simultaneously.

6.4.1.4 Experimental Measurement of Spinning Motion

The measurement of spinning motion is realized by using the slotted plate illustrated in Fig. 6.9. The theoretical and experimental results are presented in Fig. 6.10. It can be found that the maximum error is around 0.65°. Compared with the tilting angle measurement, the precision of spinning angle measurement is relatively low. To increase the precision further, two solutions could be employed.

• The first solution is to increase the slot numbers or reduce the size of each slot. In this way, the measurement resolution is higher. However, the minimal size cannot be too small practically due to the fabrication constraint.

• The other solution is to use new model of laser sensors that can capture many light spots on the target. As shown in Fig. 6.11, some laser sensors can project a light line on the target with slots. The line consists of many light spots, up to one thousand points in 20mm. The distance between two neighboring points ρ is 0.02mm. The laser controller can scan these spots to find points at the edge of slot. For example, for position 1 in Fig. 6.11, point m_1 is the at the edge, and for position 2, point m_2. The rotation angle can be calculated with Eqn. (6.12). With this method, the spinning angle can be measured precisely, up to 0.03° theoretically.

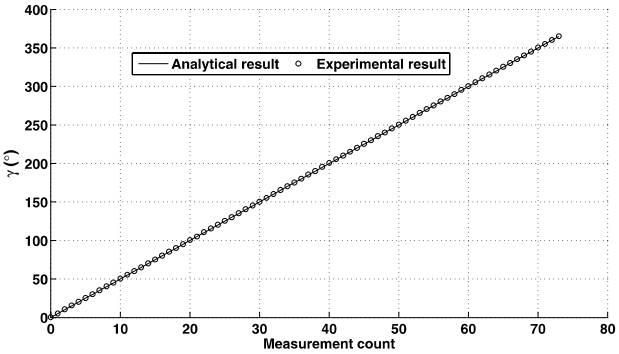

(a) Experimental & analytical results

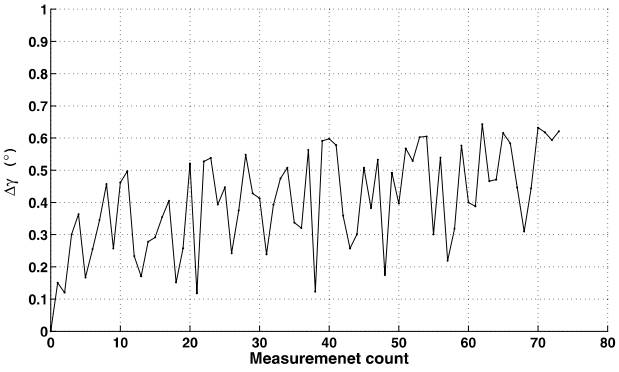

(b) Difference between experimental & analytical results

Fig. 6.10: Experimental measurement on the spinning motion

$$\gamma = \arctan \frac{\rho(m_2 - m_0)}{h} - \arctan \frac{\rho(m_1 - m_0)}{h}. \tag{6.12}$$

6.4.2 Experimental Measurement on Apparatus 2

Above experimental measurements are conducted on the single-axis motor that can achieve high-precision motion. However, it cannot realize the simultaneous measurement of three rotations. Therefore, the other apparatus as shown in Fig. 6.12 has been developed for this purpose. An arc guide is supported with two pillars on the platform. The plate is fixed on the apparatus through a spherical bearing and thin pillar. The spherical bearing indicated in Fig. 6.13(b) can achieve 3-DOF motion in

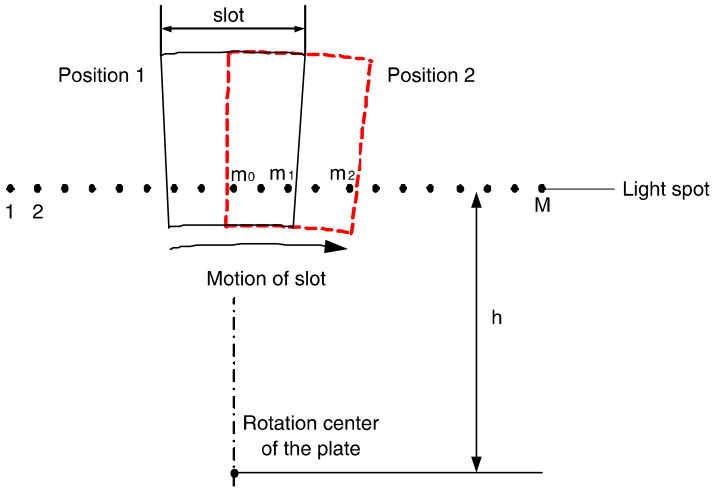

Fig. 6.11: High-density light spots of laser sensor on moving slot

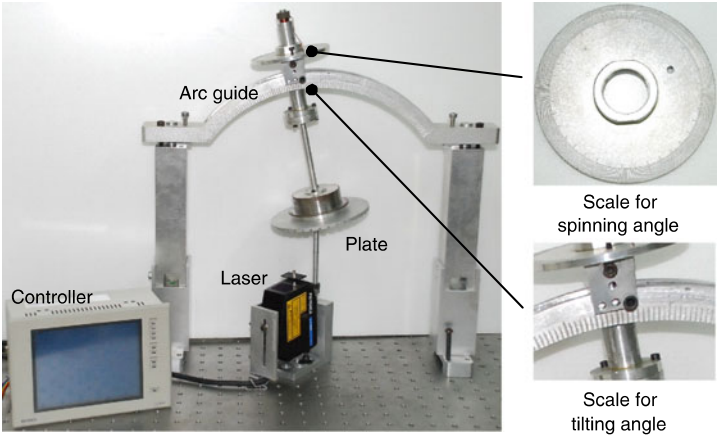

Fig. 6.12: Apparatus for measuring three directions simultaneously

only one joint. It is assembled at the center of plate to produce spherical motions (Fig. 6.13(a)). The rotation center of the bearing should be coincident with the center of the arc guide to make sure the measurement is precise. The plate is connected to the arc guide through a shaft which can slide along the guide and spin about its own axis. The tilting and spinning angles can be measured through the scales indicated in the figure. The laser sensor shifts an angle with respect to the tilting direction of the shaft so that it can generate two tilting and one spinning measurement results. The measured result is transferred to the computer for data processing. The two tilting angles are computed from Eqn. (6.8). C is obtained from

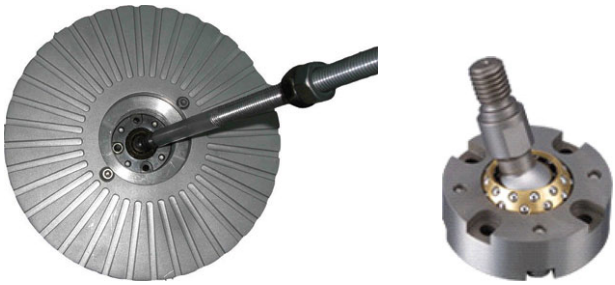

(a) Slotted plate with bearing (b) Spherical bearing [23]

Fig. 6.13: Assembly of 3-DOF spherical bearing on the plate

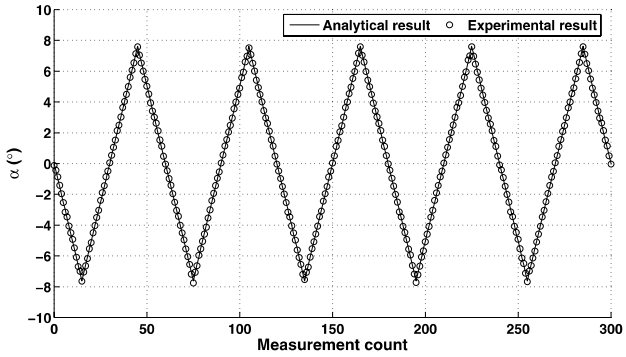

(a) Experimental & analytical results of α

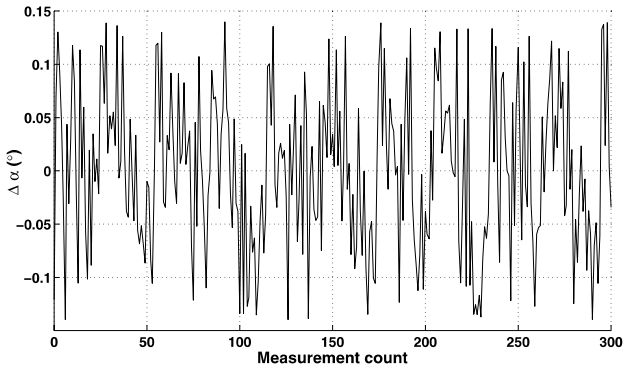

(b) Difference between experimental & analytical results of α

Fig. 6.14: Experimental measurement of tilting motion on Apparatus *II*

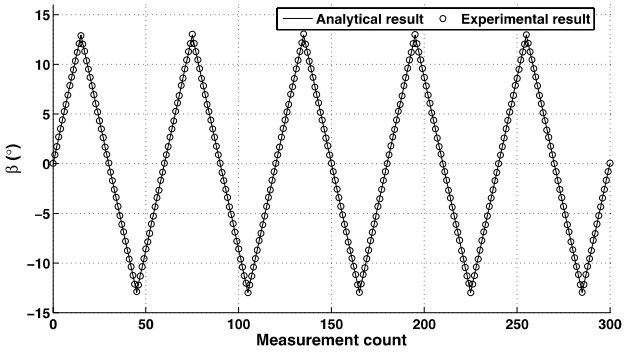

(c) Experimental & analytical results of β

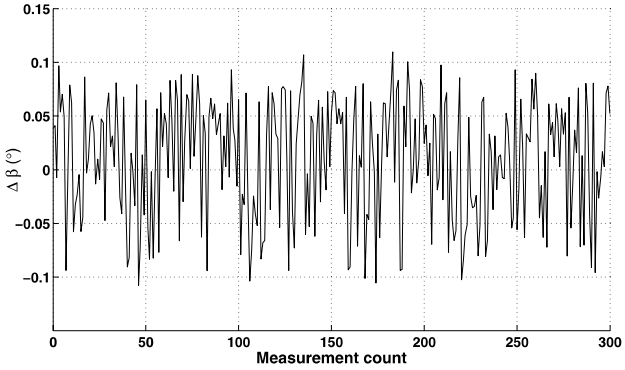

(d) Difference between experimental & analytical results of β

Fig. 6.14: Experimental measurement of tilting motion on Apparatus *II*

$$C = R_z(\theta_3)R_x(\theta_1)\begin{bmatrix}0 & 0 & 1\end{bmatrix}^T, \tag{6.13}$$

where

$$R_x(\theta_1) = \begin{bmatrix}1 & 0 & 0\\ 0 & \cos\theta_1 & -\sin\theta_1\\ 0 & \sin\theta_1 & \cos\theta_1\end{bmatrix}. \tag{6.14}$$

θ_1 is the tilting angle of the shaft mounted on the plate. The measured and analytical results are presented in Fig. 6.14. It can be found that the difference between analytical and experimental results measured with this apparatus is larger than that of first apparatus with a single-axis motor. This is due to the large assembly error, such as the non-concentricity of rotation center of plate and the arc guide. The measurement precision of the angular scale is not so precise as that of servo motor.

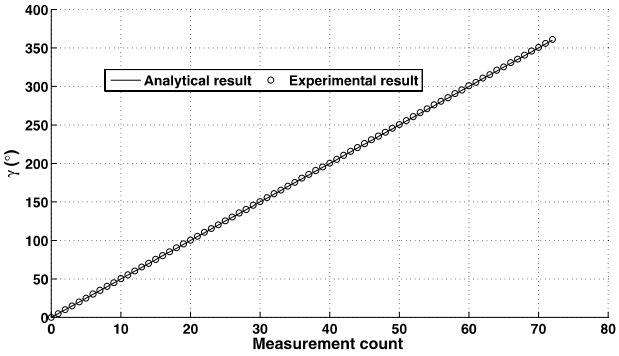

(a) Experimental & analytical results

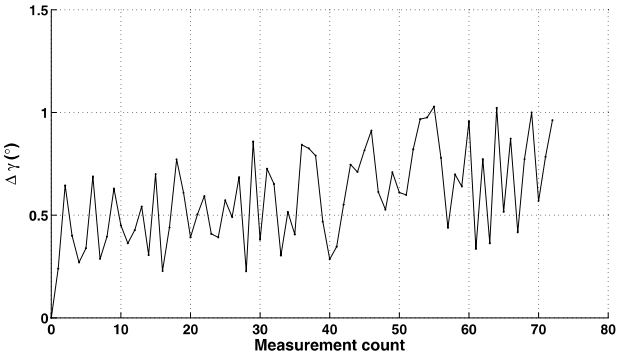

(b) Difference between experimental & analytical results

Fig. 6.15: Experimental measurement of spinning motion on Apparatus *II*

6.5 Conclusion

Orientation measurement for rigid body with multi-DOF rotational motion is an important topic for robotics, actuators, instruments and manufacturing technology. The purpose of this study is to propose a novel high-precision non-contact displacement measurement method for 3-DOF rotational motions. The operating principle of this measurement method is based on the non-contact laser detection. It has several advantages compared with other orientation measurement methods. The non-contact property avoids friction and additional mass/inertia moment exerted on the moving part that may significantly reduce the system working efficiency. Compared with other non-contact measurement methods, this laser-based method can achieve a high-precision measurement result, and its performance is not affected by environmental field. The algorithm for three rotation angles has been derived. Two experi-

mental apparatus have been developed to conduct measurements, and to evaluate the proposed orientation measurement method. The comparison between analytical and experimental results shows that the proposed orientation measurement method can achieve high precision measurement results for multi-DOF simultaneous motions, up to 0.08°. The difference could be caused by the resolution of laser sensor, surface treatment of the plate, motor resolution, assembly error and measurement error. A high resolution laser sensor could improve the precision of the proposed measurement method further. In the future, we will find ways to implement the laser based method into our spherical actuator by using simple laser diode in compact package to fit into motor assembly.

References

1. Saxena S C, Sahu C et al (1994) Differential Inductive Ratio Transducer with Short-circuiting Ring for Displacement Measurement. IEEE Transactions on Instrumentation and Measurement, vol. 43, no. 5:777–780, October 1994.
2. Dong L, Nelson B J, Fukuda T, Arai F, Coat G L et al (2006) Towards Nanotube Linear Servomotors. IEEE Transactions on Automation Science and Engineering, vol. 3, no. 3:228–235, July 2006.
3. Lee S (2005) Development of a New Variable Remote Center Compliance (VRCC) with Modified Elastomer Shear Pad (ESP) for Robot Assembly. IEEE Transactions on Automation Science and Engineering, vol. 2, no. 2:193–197, April 2005.
4. Bone G M, Ning S et al (2007) Experimental Comparison of Position Tracking Control Algorithms for Pneumatic Cylinder Actuators. IEEE/ASME Transactions on Mechatronics, vol. 12, no. 5:557–561, October 2007.
5. Shan Y, Speich J E, Leang K K et al (2008) Low-Cost IR Reflective Sensors for Submicrolevel Position Measurement and Control. IEEE/ASME Transactions on Mechatronics, vol. 13, no. 6:700–709, December 2008.
6. Ferrari P, Flammini A, Marioli D, Taroni A et al (2008) IEEE 1588-Based Synchronization System for a Displacement Sensor Network. IEEE Transactions on Instrumentation and Measurement, vol. 57, no. 2:254–260, February 2008.
7. Falkner A H (1994) The Use of Capacitance in the Measurement of Angular and Linear Displacement. IEEE Transactions on Instrumentation and Measurement, vol. 43, no. 6:939–942, December 1994.
8. Liu X, Wang Y, Sun Y et al (2009) Cell Contour Tracking and Data Synchronization for Real-Time, High-Accuracy Micropipette Aspiration. IEEE Transactions on Automation Science and Engineering, vol. 6, no. 3:536–543, July 2009.
9. Xu Q, Li Y, Xi N et al (2009) Design, Fabrication, and Visual Servo Control of an XY Parallel Micromanipulator with Piezo-Actuation. IEEE Transactions on Automation Science and Engineering, vol. 6, no. 4:710–719, October 2009.
10. Huang H, Sun D, Mills J K, Li W J, Cheng S H et al (2009) Visual-Based Impedance Control of Out-of-Plane Cell Injection Systems. IEEE Transactions on Automation Science and Engineering, vol. 6, no. 3:565–571, July 2009.
11. Lee K M, Sosseh R A et al (2002) Effects of Fixture Dynamics on Back-stepping Control of a VR Spherical Motor. Proceedings of the 2^{nd} IFAC Conference on Mechatronic Systems, Berkeley, California, USA, 9–11 December 2002.
12. Sosseh R A (2001) Finite Element Torque Modeling and Backstepping Control of a Spherical Motor. Thesis of Georgia Institute of Technology, GA, USA, December 2001.
13. Garner H D (2001) Development of a Real-time Vision Based Absolute Orientation Sensor. Thesis of Georgia Institute of Technology, GA, USA, May 2001.

14. Garner H, Lee K M et al (2000) Development of a vision based orientation sensor. Proceedings of the Dynamic Systems and Control Division, IMECE 2000, Orlando, FL, USA, vol. 1:173–180, 5–10 November 2000.
15. Lee K M, Zhou D et al (2003) A spherical encoder for real-time measurements of three-DOF wrist orientations. Proceedings of the 2003 IEEE/RSJ Intl. Conference on Intelligent Robots and Systems, 1596–1601, Las Vegas, Nevada, USA, 2–5 October 2003.
16. Lee K M, Zhou D et al (2004) A real-time optical sensor for simultanous measurment of 3-DOF motions. IEEE Transactions on Mechatronics, vol. 9, no. 3:499–506, September 2004.
17. Wang J, Jewell G W, Howe D et al (1998) Analysis, design and control of a novel spherical permanent-magnet actuator. IEE Proceedings: Electric Power Applications, vol. 145, no. 1:61–71, 2–5 January 1998.
18. Wang W, Wang J, Jewell G W, Howe D et al (2003) Design and control of a novel spherical permanent magnet actuator with three degrees of freedom. IEEE/ASME Transactions on Mechatronics, vol. 8, no. 4:457–468, December 2003.
19. Lee K M, Son H et al (2005) Torque model for design and control of a spherical wheel motor. Proceedings of the 2005 IEEE/ASME International Conference on Advanced Intelligent Mechatronics, 335–340, Monterey, California, USA, 24–28 July 2005.
20. Foggia A, Oliver E, Chappuis F et al (1988) A new three degrees of freedom electromagnetic actuator. Proceedings of IAS, vol. 35:137–141, New York, USA, 24–28 July 1988.
21. Jin H Z, Lu H, Cho S K, Lee J M et al (2007) Nonlinear Compensation of a New Noncontact Joystick Using the Universal Joint Mechanism. IEEE/ASME Transactions on Mechatronics, vol. 12, no. 5:549–556, October 2007.
22. Craig J J (1989) Introduction to Robotics: Mechanics and Control. Addison-Wesley Publishing Company, USA, 1989.
23. Hephaist Seiko Co., Ltd. (2005) Specification of spherical bearings. In: The website of Hephaist Seiko Co., Ltd. Available online: http://www.hephaist.co.jp/e/pro/ball.html. Cited May 2005

Chapter 7
Conclusions

7.1 Accomplishments and Contributions

This monograph has presented study on a permanent magnet spherical actuator with the following tasks: (1) formulation of the magnetic field produced by the PM-pole rotor; (2) torque modeling of the spherical actuator; (3) design and prototyping of the spherical actuator; (4) experimental investigation on the magnetic field distribution and torque variation; (5) investigation of a non-contact orientation measurement method base on laser detection. All these works are fundamental and critical to the position and velocity servo control of the PM spherical actuator. Specifically, the magnetic field modeling is the prerequisite of the actuator torque; design and prototyping of the actuator is necessary for experimental investigation of the magnetic field distribution and actuator torque variation; the orientation measurement method is important for closed-loop motion control of the spherical actuator.

Based on the PM pole arrangement, the magnetic field surrounding the rotor is formulated using Laplace's equation and Poisson's equation with the general solution of the magnetic scalar potentials. By utilizing appropriate boundary conditions and the spherical harmonic expansion of the radial component of the residual magnetization vector, the coefficients in the general solution of the scalar potential can be determined. Because magnetic intensity is the gradient of magnetic scalar potential, the magnetic flux density distribution in the air space surrounding the PM-pole rotor is obtained.

With knowledge of the magnetic field expression, the torque modeling of the actuator which relates current inputs to the torque output of the spherical actuator can be carried out. According to Lorentz force law, the differential torque caused by a differential wire segment can be formulated. The torque created between a single coil and the PM-pole rotor can be obtained by integrating the differential torque within the coil volume. Using the principle of superposition, the torque for full set of coils can be finally obtained, which is linearly proportional to the current inputs. This linearity facilitates the real-time control of the spherical actuator.

L. Yan et al., *Design, Modeling and Experiments of 3-DOF Electromagnetic Spherical Actuators*, Mechanisms and Machine Science 4,
DOI 10.1007/978-94-007-1646-9_7,

Inverse electromagnetic solution of the torque model, i.e., solving the required current inputs for desired torque output, has been discussed. It is verified that there is no singularity in the torque model within the workspace of the spherical actuator. Because the torque model is a multiple input (coil currents) multiple output (3D torque) system, there are infinite possible inverse electromagnetic solutions. A minimum right-inverse solution has been proposed to obtain the current inputs for the actuator based on minimization of power consumption.

The tunable parameters of the PM pole and coil in the torque model provide a tool for prototype design of the PM spherical actuator aiming at maximizing torque output. According to the proposed torque model, the effect of poles parameters on the torque output can be described. Thus, appropriate values for different parameters can be chosen to achieve maximum torque output. Based on the theoretical analysis, a research prototype of the spherical actuator has been developed. It can be used for the experimental investigation on the magnetic field distribution and torque variation of the spherical actuator.

Experimental investigation of the spherical actuator includes two major parts: magnetic field distribution of the PM-pole rotor and torque variation of the spherical actuator. An automated apparatus has been developed to measure the flux density variation of the rotor in 3D space. Because the magnetic flux density is a 3×1 vector, a three-axis Hall probe has been employed for the measurement. The acquired data of the magnetic field has been nondimensionalized and normalized as a benchmark result. It can be referred by similar rotor designs without regard to the specific dimensions of PM poles. The experimental result of magnetic flux density is visualized in a 3D fashion and compared with the analytical magnetic field model, which shows that the maximum different is about 7% and the theoretical model is feasible for torque modeling.

The second apparatus has been designed for the torque measurement of the spherical actuator. This apparatus can measure the torque output generated by the spherical actuator at any rotor orientation within the workspace. A six-axis force/torque sensor has been employed for the torque measurement. The torque measurement is conducted based on a single coil configuration and a multi-coil configuration. The first experiment is used to verify the torque model of a single coil as well as the linear relation between torque output and current input. The second experiment is used to verify the superposition principle of the torque model for multiple coils, i.e. the torque generated by multiple coils is superposition of torques generated by every individual coil. The experiment shows that the difference between analytical model and experimental result is about 12%, which indicates that the proposed torque model of the spherical actuator is feasible.

As indicated in Fig. 7.1, to realize the closed-loop high precision position control of the spherical actuator, a high performance sensing system is necessary. This sensing system can detect the rotor orientation and then feedback it to the system controller. Some orientation sensing systems have been proposed by researchers. For example, three single-axis encoders are used in the rotor orientation measurement of VRSM [1, 2]. This type of orientation measurement system requires a mechanism that consists of two arc-shaped guides and a sliding block. This bulky structure

contributes to two-thirds of the total system inertia, which complicates the control implementation. To avoid this additional inertial moment, the non-contact type sensor is preferred, i.e., there is no contact between the measurement system and the rotor. A real-time vision based absolute orientation sensor has been proposed by Garner *et al* [3, 4]. In order for the implementation of this sensor, the rotor surface is required to be grided and the resolution of the sensor depends on the density of grids. Lee *et al*. [5] have proposed a microscopic-surface-based optical sensor. The grid pattern is no longer required for the rotor surface. However, this type of sensors is very sensitive to the gap as well as the relative motion speed between the rotor surface and the sensor tip. Its availability needs to be validated further. Because the magnetic field of the PM-pole rotor has been formulated, a possible orientation measurement sensor could be the Hall effect sensor. Several Hall effect sensors can be placed at different positions relative to the rotor. Based on the magnetic field formulated, the rotor orientation could be calculated from the measured value of flux density by these Hall-effort sensors. The implementation of this sensor needs to be considered further and the performance of this orientation detection approach is necessary to be evaluated. In this study, an non-contact orientation measurement method has been proposed based on the laser detection to achieve high precision measurements. Experiments are conducted to validate the performance of the proposed orientation measurement methods.

This research has established a fundamental basis for the study of 3-DOF PM spherical actuators. The major contributions of this investigation are summarized in aspects as follows.

• A design concept of the spherical actuator using multiple PM poles and multiple layers of stator air-core coils has been proposed. One advantage of this configuration is that different numbers and patterns of stator and rotor poles are allowed to be incorporated to improve the working range as well as the motion resolution of the spherical actuator. This configuration also offers a linear relation between torque output and current inputs. The linearity can facilitate the real-time motion control of the PM spherical actuator.

• Formulation of the magnetic field of PM-pole rotor is a prerequisite of actuator torque modeling. The challenge of formulating the magnetic field of the spherical actuator is that the magnetic flux density varies at every point of the 3D space surrounding the PM-pole rotor. By using the Laplace's equation of the magnetic scalar potential, the flux density of the PM-pole rotor has been formulated. The parameters of PM poles in the model can be adjusted to observe the magnetic field variation.

• The torque output of single-axis actuators has a constant direction, which makes the torque formulation much easier. However, for 3-DOF spherical motion actuators, the torque output is an orientation dependant 3D vector. Based on Lorentz force law as well as the magnetic field expression, the torque model of the spherical actuator has been formulated analytically, which could facilitate the real-time position and velocity control of the spherical actuator. Another feature of this analytical

torque model is that the two major force/torque generating elements, PM poles and coils, are parameterized. This provides an opportunity to study the effect of each parameter on the torque output of the spherical actuator. As a result, the dimensions of PM pole and coil can be determined to achieve maximum torque output.

• Experimental measurement of magnetic field can be used to verify the theoretical model as well as observe the magnetic flux density distribution. In this research, an automated apparatus has been developed to measure the magnetic flux density distribution of the PM-pole rotor in 3D space completely. A three-axis Hall probe is employed to measure the three components of flux density of the PM-pole rotor. This probe can be mounted on the apparatus and pinpoint to any point surrounding the rotor then acquire the data of flux density at that point. The acquired data has been processed with nondimensionalization and normalization so that it could be used to compare with analytical magnetic field model as well as referred by designs with other rotor configuration.

• The torque output of spherical actuators is orientation dependant. The orientation measurement is significant for closed-loop motion control of spherical actuators. Various orientation measurement methods have been proposed by other researchers. Non-contact type measurement methods are preferred as there is no friction and additional inertial moment on the rotor, which may help to improve the system dynamics. An non-contact orientation measurement method based laser detection is proposed in this study. Its performance is not affected by the environmental field and could achieve high precision measurements. Experiments are conducted to validate the operating principle of the proposed orientation measurement methods.

7.2 Recommendation for Future Research

To continue this research effort, the following aspects are recommended.

• Development and implementation of a servo control algorithm

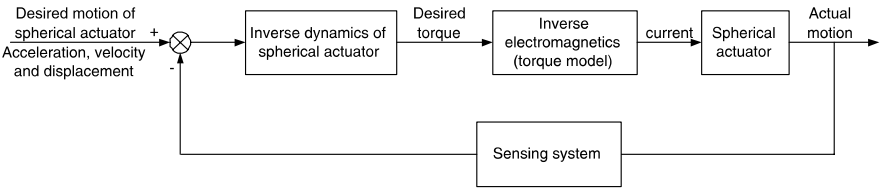

Fig. 7.1: Block diagram of motion control of the spherical actuator

Development of the control system is critically important for practical uses of the spherical actuators. The schematic block diagram of motion control of the spherical actuator is illustrated in Fig. 7.1. The angular acceleration, angular velocity and angular displacement of the spherical actuator are provided as the desired actuator motion. Based on the inverse dynamics of the spherical actuator, the desired torque can be computed. Inverse electromagnetic solution is carried out to compute the required current inputs corresponding to the desired torque output. Finally, these current inputs are applied to the coils in the spherical actuator so that the actuator can follow the desired motion. Presently, a twelve-channel current controller as shown in Fig. 7.2 has been developed for energizing stator coils. This current controller can manage twelve-channel current inputs at the same time. By using one or two pieces of this current controllers, the current inputs to the coils on the PM spherical actuator can be varied. In the future, a control algorithm will be developed and implemented on the system by using the current controller to achieve real-time feedback control of the actuator. The rotor dynamics and external payload will be considered for the motion control of spherical actuator.

- **Using laminated soft-iron as the stator material**

Currently, large size is chosen for the aluminum stator to avoid the eddy current on the stator generated by the PM poles and to facilitate the experimental measurement of flux density. In order to reduce the actuator size, nonmetal materials such as Delrin could be used to replace the aluminum for commercialized products as eddy current would not be created for nonmetal materials. However, these materials normally cannot withstand the high temperature produced by the coils. In this situation, laminated soft iron may be a good option as it can bear the high temperature resulted from the electrical power consumption. Furthermore, the eddy current generated by the PM poles is ignorable. More importantly, due to the high permeability of the soft iron, the loss of magnetic energy could be reduced and torque produced by the spherical actuator could be improved greatly.

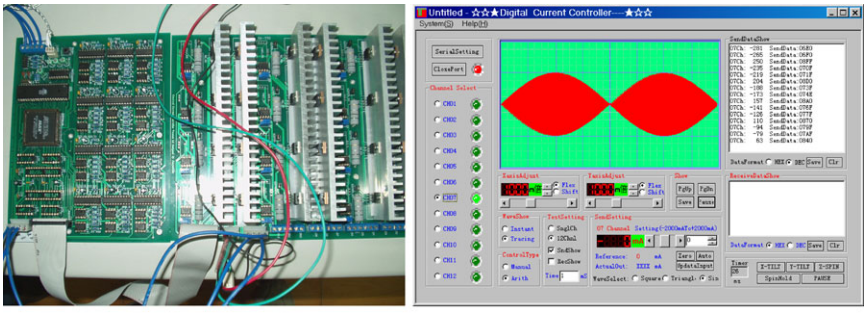

(a) Electric circuit (b) Interface

Fig. 7.2: Twelve-channel current controller

References

1. Lee K M, Sosseh R A et al (2002) Effects of Fixture Dynamics on Back-stepping Control of a VR Spherical Motor. Proceedings of the 2nd IFAC Conference on Mechatronic Systems, Berkeley, California, USA, 9–11 December 2002.
2. Sosseh R A (2001) Finite Element Torque Modeling and Backstepping Control of a Spherical Motor. Thesis of Georgia Institute of Technology, GA, USA, December 2001.
3. Garner H D (2001) Development of a Real-time Vision Based Absolute Orientation Sensor. Thesis of Georgia Institute of Technology, GA, USA, May 2001.
4. Garner H, Lee K M et al (2000) Development of a vision based orientation sensor. Proceedings of the Dynamic Systems and Control Division, IMECE 2000, Orlando, FL, USA, vol. 1:173–180, 5–10 November 2000.
5. Lee K M, Zhou D et al (2004) A real-time optical sensor for simultanous measurment of 3-DOF motions, IEEE/ASME Transactions on Mechatronics, vol. 9, no. 3:499–506, September 2004.

Index

L. Yan et al., *Design, Modeling and Experiments of 3-DOF Electromagnetic Spherical Actuators*, Mechanisms and Machine Science 4,
DOI 10.1007/978-94-007-1646-9, © Springer Science+Business Media B.V. 2011